NASA SP-109

Development of a Small Animal Payload and Integration with a Sounding Rocket

Edited by Larry J. Early
Wallops Station
Wallops Island, Virginia

Scientific and Technical Information Division 1966
NATIONAL AERONAUTICS AND SPACE ADMINISTRATION
Washington, D.C.

Foreword

A small-animal payload has been designed, developed, integrated with a modified Arcas launch vehicle, and qualified by both ground and flight testing in Phase I of the Bio-Space Technology Training Program. The vehicle is to be used in assisting biological experimenters in their evaluation of the engineering and operational aspects of space-flight research. The results of Phase I of this program are presented in this report. Included are the design criteria of the various payload systems and a description of the resulting launch configuration. The theoretical trajectory, aerodynamic analysis, environmental determination, qualification testing, and biological bench testing are discussed. Finally, the flight testing of the complete Bio-Space configuration is summarized.

The editor wishes to thank the following for their assistance in preparing this report: David F. Detwiler, Luther W. Gurkin, Ira D. Jacobson, G. W. Martin, George E. Miles, Mendel N. Silbert, and William W. West.

Contents

Introduction

Early in 1964 Wallops Station was requested by NASA Headquarters to design and qualify an appropriate payload-vehicle system to be used as a training aid for bio-scientists. The primary purpose of this system is to assist biological experimenters in evaluating the engineering and operational aspects of space-flight research. In response to this request, Wallops Station developed a small-animal payload and integrated it with a modified Arcas vehicle. This design effort was known as Phase I of the Bio-Space Technology Training Program. The sounding-rocket/animal-payload configuration was successfully flight qualified in a test program which culminated in the launch and recovery of two such payloads, each containing a laboratory white rat, in September 1964.

The Bio-Space launch vehicle (fig. 1) is an unguided, single-stage, sounding rocket capable of exposing a small-animal payload to a flight mission profile containing typical facets of space-flight research and experimentation. A brief description of the Bio-Space nominal flight mission is as follows: (1) Launch vehicle ignition initiates the flight at $t = 0$ seconds, (2) the vehicle exits the launcher tube at $t = 0.15$ seconds, (3) the launch vehicle burns out at $t = 30$ seconds, (4) the launch vehicle coasts under free fall to apogee where payload separation occurs at $t = 108$ seconds, (5) the parachute is opened at $t = 114$ seconds, and (6) the payload and attached parachute impact in the water at $t = 21.5$ minutes.

The purpose of this report is to document Phase I of the Bio-Space Technology Training Program which includes the design, development, integration, and ground and flight verification testing of the small-animal payload.

General Configuration

The Bio-Space configuration has an 18.53-caliber cylindrical body fitted with a tangent ogive nose of 4.0 fineness ratio and an 0.83-caliber boattail. Cruciform fins, with a 2.34° semi-wedge angle (measured in stream direction), 30° leading-edge sweep, unswept trailing edge, a taper ratio of 0.654, and an exposed aspect ratio of 1.545, are incorporated in this sounding rocket.

The complete launch configuration shown in figure 1 has an overall fineness ratio of 23.36. Total lift-off weight is 81.6 pounds, with 15.88 pounds of the total weight located above the rocket's thrust face.

The major diameter of the payload, adapter section, and Arcas vehicle is 4.5 inches. The Bio-Space payload has a fineness ratio of 8.73, weighs 13.28 pounds (including 200-gram white rat), and contains an internal volume of 430 cubic inches. The payload assembly primarily consists of a fiberglass nose cone, telemetry instrumentation with associated supporting structure, and a life-support capsule. The payload is attached to the recovery/adapter section with a friction-fit sleeve joint, and the recovery/adapter assembly is attached to the forward retaining ring of the motor case with a threaded joint. The recovery/adapter assembly consists of a cylindrical container housing a 3.7-foot-diameter radar reflective parachute, deployment system, payload attachment hardware, and an expulsive piston. Sectional views of the Bio-Space payload and recovery/adapter assembly are presented in figure 2, along with an identification and description of the components.

The Arcas vehicle is powered by a high-performance rocket motor using an end burning charge of plastisol-type solid propellant. The rocket-motor case consists of a one-piece steel outer casing with an insulating liner. Four aluminum fins are bonded to the case to provide aerodynamic stability.

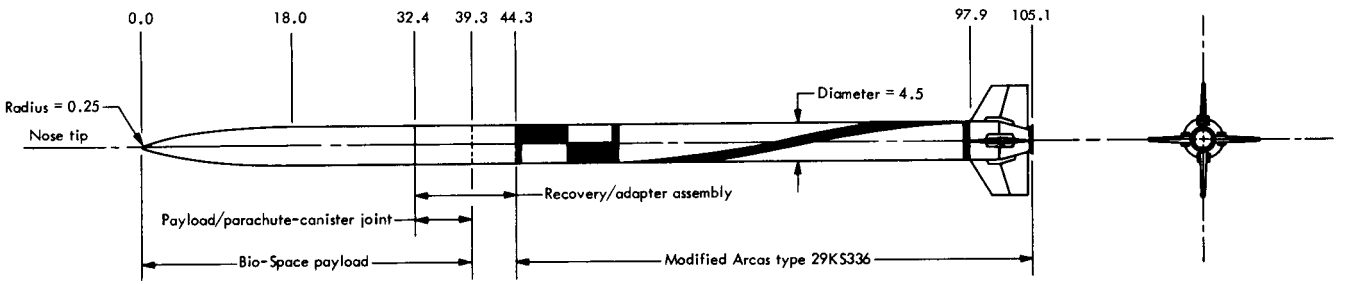

General configuration

Aerodynamic configuration data

Nose:	Fineness ratio 4.00 - tangent ogive
Body:	Fineness ratio 18.53 - cylinder
Boattail:	Fineness ratio 0.83 - $\theta_b = 15.5^\circ$
Fins:	$S_{f,e}$ = 23.38 in^2/panel
	$A_e = b_e^2/S_{f,e}$ = 1.545
	$\lambda_e = c_t/c_{r,e}$ = 0.654
	$c_{r,e}$ = 6.65 inches
	c_t = 4.35 inches
	b_e = 8.5 inches
	Λ_{le} = 30°
	$t_{r,e}$ = 0.310 inches
	$(t_{r,e}/c_{r,e})$ = 0.048
	θ_{te} = 4.86°

Nominal fin cant:

12'/panel (p = 4 cps max)
59'/panel (p = 20 cps max)

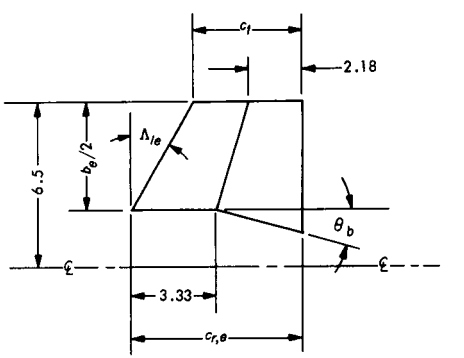

Fin detail

FIGURE 1. — *General configuration and aerodynamic data. All linear dimensions are in inches.*

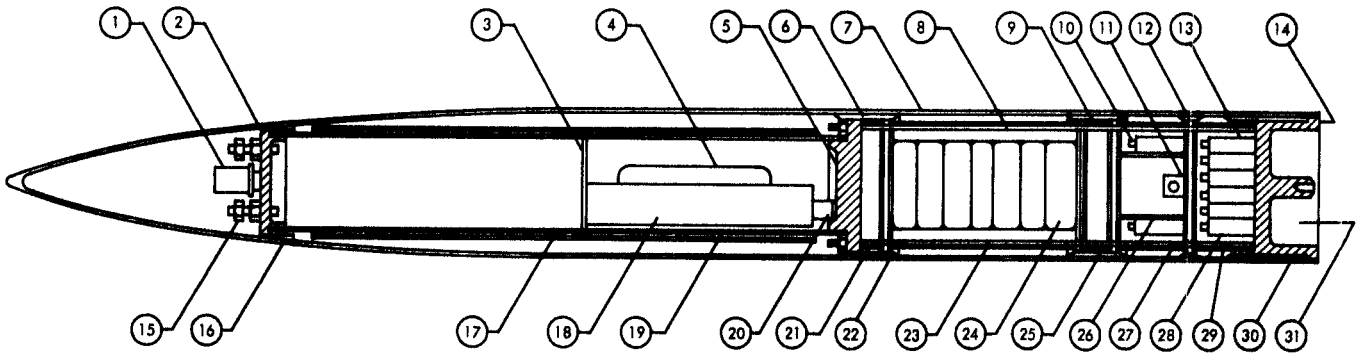

No.	Description
1	Oxygen pressure transducer
2	Life-support top plug
3	Forward couch ring
4	Lithium hydroxide shield
5	Life-support end plug
6	Bumper ring
7	Nose cone
8	Steel rod
9	Terminal case
10	Power supply batteries
11	Accelerometer
12	Bumper ring
13	Power supply batteries
14	Aft end seal
15	Capsule purging valves
16	Bumper ring
17	Antenna

No.	Description
18	Animal couch
19	Life-support capsule
20	Animal couch bracket
21	Terminal case
22	Bumper ring
23	Telemetry case
24	Telemetry components
25	Bumper ring
26	Battery box insert
27	Battery case
28	Rigid plastic foam
29	Battery case
30	End seat
31	Fluorescein dye
32	Parachute container
33	Parachute
34	Joint that mates to Arcas rocket

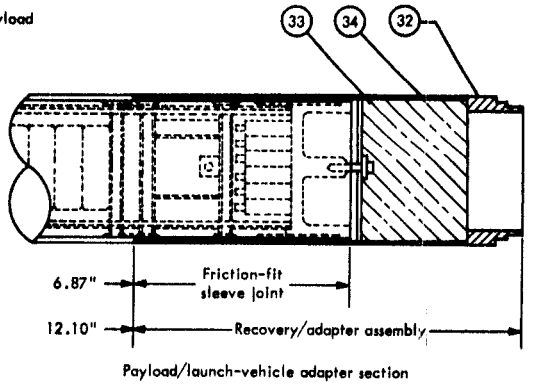

FIGURE 2. — *Bio-Space payload and recovery/adapter assembly.*

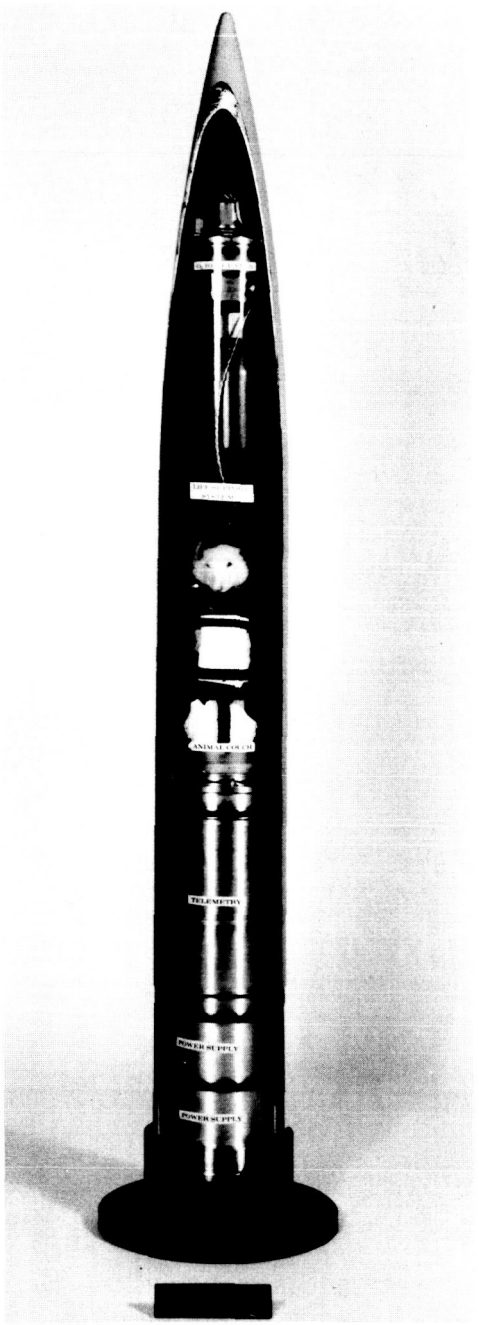

FIGURE 3. — *Payload cutaway view.*

BIO-SPACE PAYLOAD

The nose shape selected is a tangent ogive with a fineness ratio of 4.0, a 16-caliber tangent ogive radius, and a nose tip blunted with a 0.25-inch radius. The fiber-glass nose cone consists of the aforementioned nose shape and a cylindrical section that together provide a total length of 39.3 inches, a major diameter of 4.5 inches, and a volume of 430 cubic inches. External access to the nose cone is provided only at the base to minimize potential flotation and life-support sealing problems. The payload includes a tandem arrangement of a life-support system, telemetry system and power supplies, and recovery aid as shown in the sectional view of figure 2 and the cutaway view of figure 3.

The life-support system consists of a sealed cylindrical chamber with a volume of 110 cubic inches (neglecting the rat displacement).

The specimen, strapped in a specially designed contour couch, is placed into the sealed chamber which contains a 24-psia pure oxygen atmosphere with anhydrous lithium hydroxide as a carbon dioxide and water-vapor absorbent. The animal can survive over 8 hours in the life-support system at the design environment without pronounced ill effects.

An FM - FM telemetry system

and associated power supply are included to monitor the various parameters during the flight. Four continuous channels are provided: two channels are allocated to the biological functions, ECG and skin temperature; and the remaining two channels are used to measure payload longitudinal accelerations and life-support-system pressure. In addition, roll rate data are obtained from a time history of the payload received signal strength.

LAUNCH VEHICLE

The launch vehicle for the Bio-Space payload is a slightly modified version of the Arcas motor. The Arcas 29KS336 rocket motor is loaded with a stable, high-impulse solid propellant. The end-burning geometry of the propellant grain provides maximum propellant loading density and efficient conversion of propulsion energy to vehicle velocity.

The rocket-motor performance (for sea-level conditions at 70° F) used in the trajectory analysis is as follows:

Average thrust (total), lb	313
Chamber pressure, psi	1020
Web burning time, sec	28
Total burning time, sec	30
Web impulse, lb-sec	9100
Total impulse, lb-sec	9400

The nominal thrust time curve is shown in figure 4. Motor weight before firing is 66 pounds, and after firing it is 24 pounds.

The standard Arcas motor is described in detail in reference 1.

The following changes were specified and incorporated for the Bio-Space Arcas vehicles:

(1) Separation-device modification — The pyrotechnic-type explosion system was replaced with a conventional "high-low" impulse system utilizing a progressive burning ballistic charge.

(2) Grain-retention modification—A structural over-wrap grain retention system was used in lieu of the "coolie cap" method.

(3) Payload-attachment modification — The payload attachment stud thread was reversed from a right-hand to a left-hand screw thread attachment.

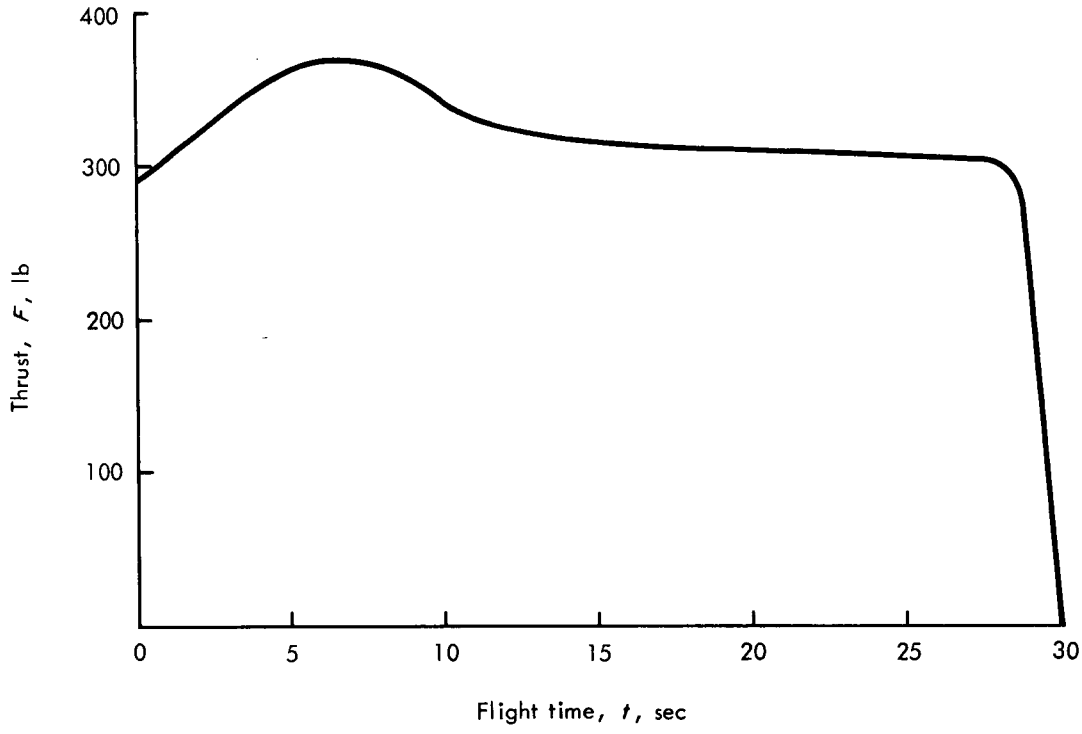

FIGURE 4. — *Arcas sea-level thrust (sea-level pressure at 70° F).*

(4) Fin cant modification—Each fin panel was canted to a nominal setting of 59′ of arc with a tolerance of ± 5′ of arc. Theoretically, this fin cant will provide 20 cps at motor burnout.

(5) Separation time modification—The separation device was changed to provide a time delay of 73 to 88 seconds after burnout of Arcas motor.

Modifications (1), (2), and (3) were proposed by the manufacturer and are now incorporated on the standard Arcas launch vehicle.

CHAPTER 2

Trajectory and Performance

TRAJECTORY COMPUTER PROGRAM

Theoretical trajectory calculations were performed using a two-dimensional particle analysis on a circular, non-rotating earth. Thrust and weight were input as functions of time, with aerodynamic drag data as functions of Mach number. Effective thrust was computed by correcting time-dependent sea-level thrust for ambient pressure. Atmospheric parameters were defined by the 1962 U.S. Standard Atmosphere with seven-step exponential fit to density and linear variation of sonic velocity.

NOMINAL TRAJECTORY

The nominal trajectory for the Bio-Space launch configuration was computed using a net payload weight of 15.88 pounds and a launch quadrant elevation angle of 80°.

The nominal flight sequence is as follows:

Event	*Flight time, sec*
Ignition	0.0
Lift-off	0.1
End of web burning	28.0
Burnout	30.0
Payload separation	108.0
Parachute opening	114.0

An initial velocity of 150 ft/sec at a flight time of 0.1 second was included due to the velocity augmentation from the standard EX 120 closed-breech launcher. (A gas generator was not used.)

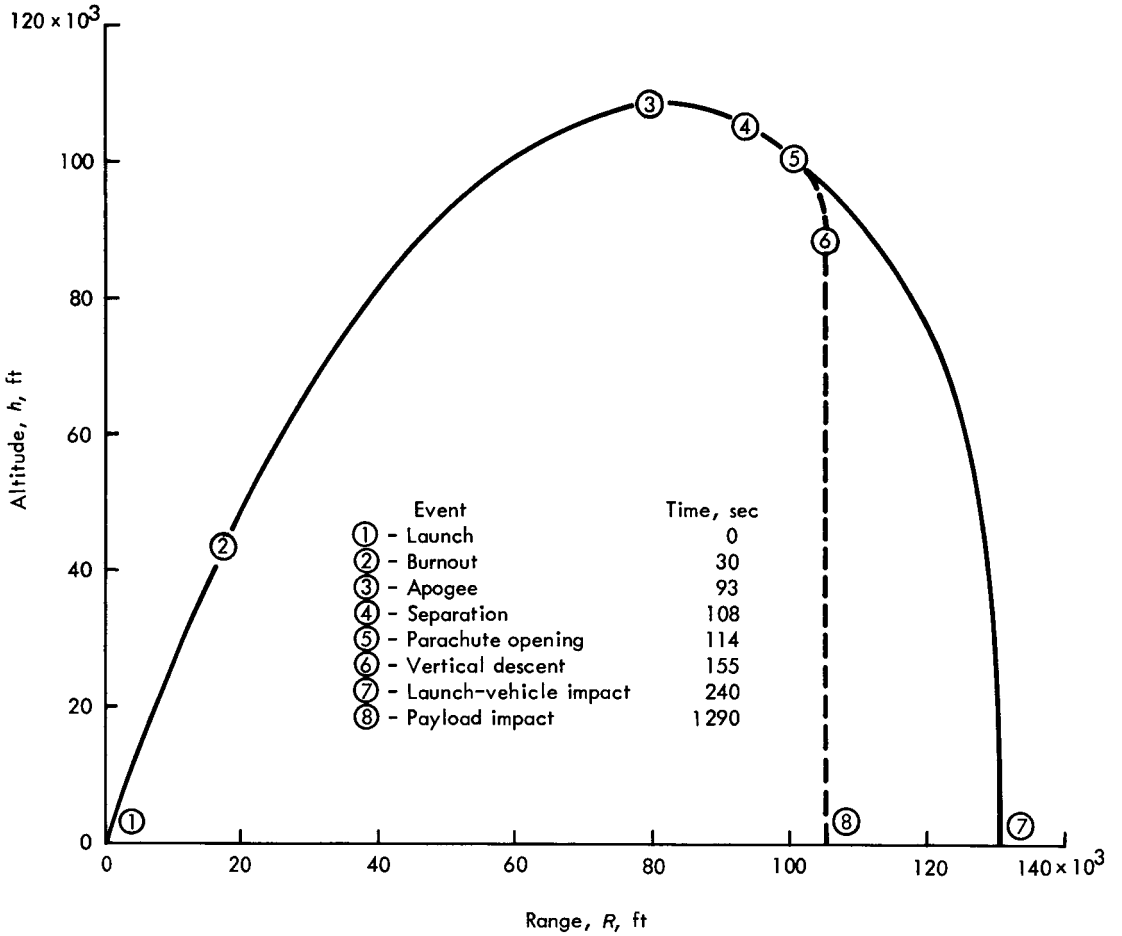

FIGURE 5. — *Nominal trajectory profile (no-wind conditions; launch quadrant elevation angle = 80°).*

The thrust and weight time histories are shown in figures 4 and 35. These values were used directly as input data into the trajectory program.

The drag characteristics of the launch configuration for all phases of the trajectory were taken from figures 13 and 14 and entered into the trajectory program at the applicable times.

The flight parameters of the nominal trajectory are presented in figures 5 and 6. The trajectory profile and the nominal flight sequence are shown in

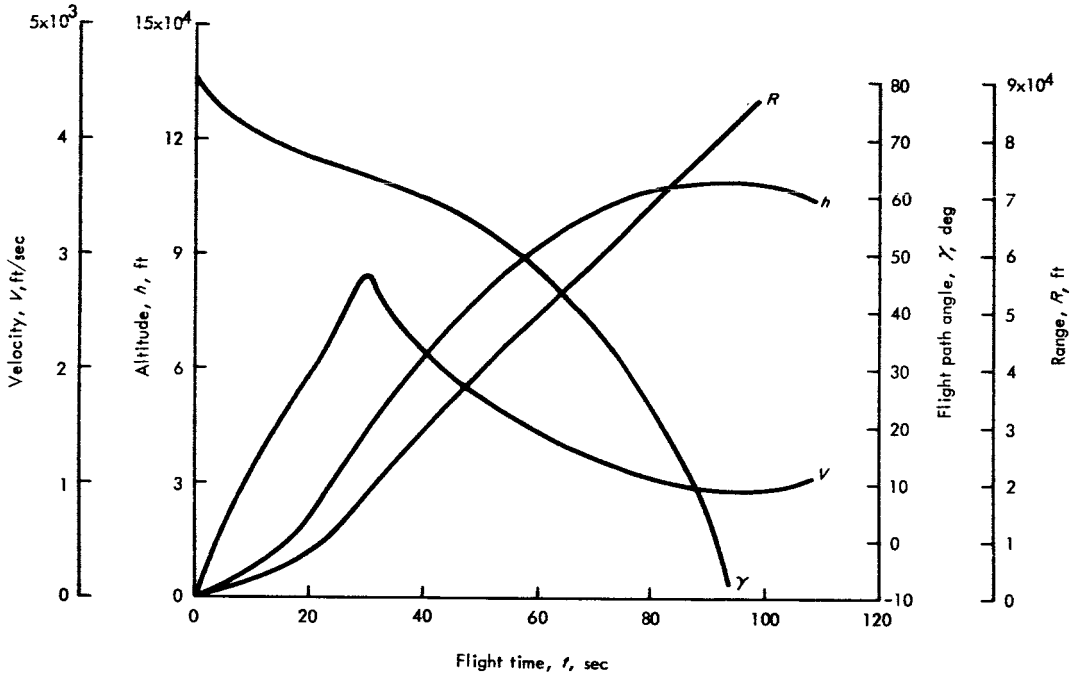

FIGURE 6. — *Nominal trajectory parameters.*

figure 5. Figure 6 shows the range, altitude, velocity, and flight-path elevation angle, axial acceleration, dynamic pressure, and Mach number as function of time. The axial acceleration discussed above is presented relative to the vehicle.

LAUNCH CONFIGURATION PERFORMANCE

Incremental ideal velocity was computed in the standard manner:

$$\Delta V_{\text{ideal}} = (I_{sp})_{\text{avg}} g \ln \mu$$

where $(I_{sp})_{\text{avg}}$ is the average specific impulse and μ is the ratio of initial weight to burnout weight.

Drag and gravity losses were obtained from the trajectory calculations during the thrusting period of flight and expressed in impulse form. The impulse available for acceleration is shown in figure 7. This figure is used to

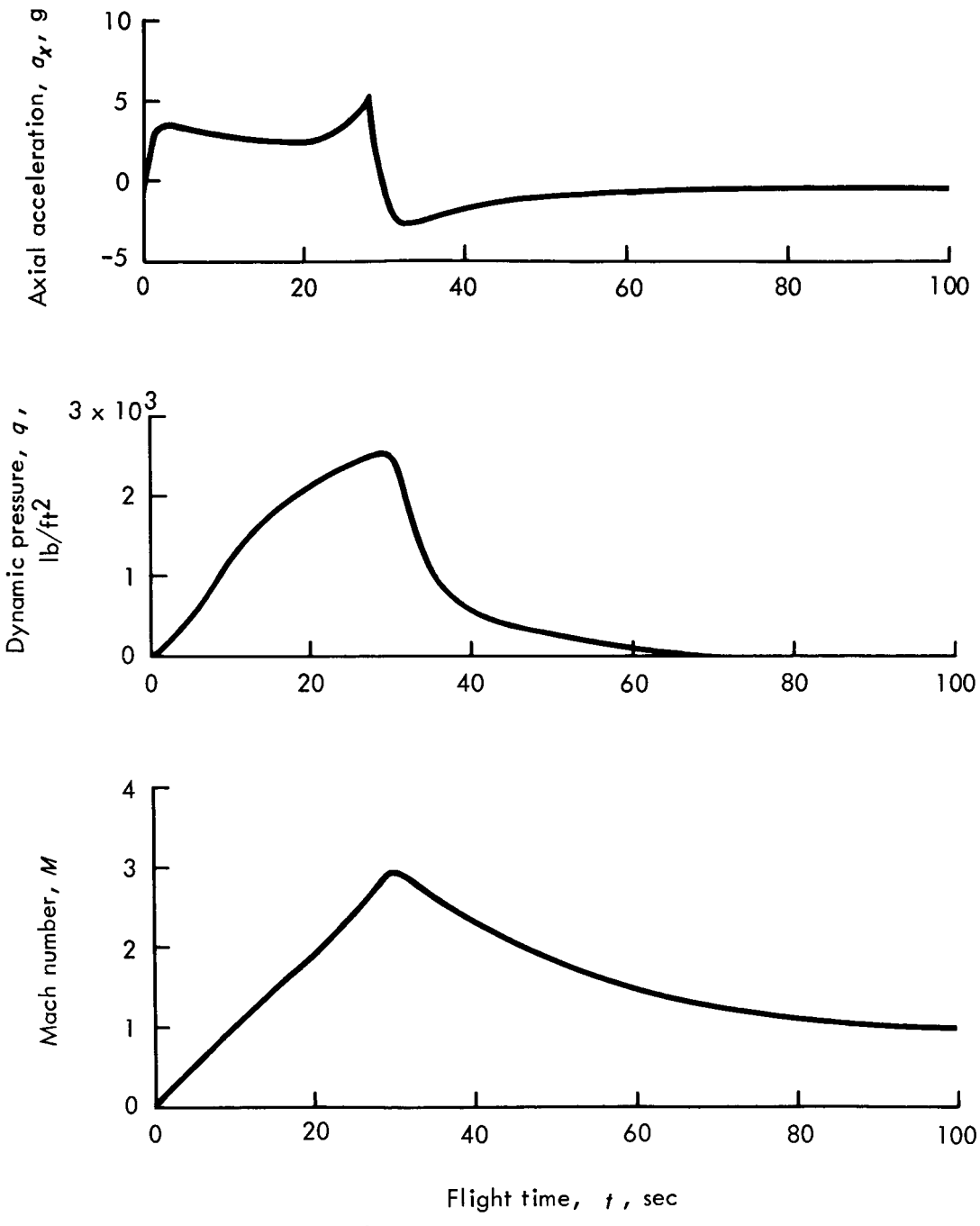

FIGURE 6. — *Concluded.*

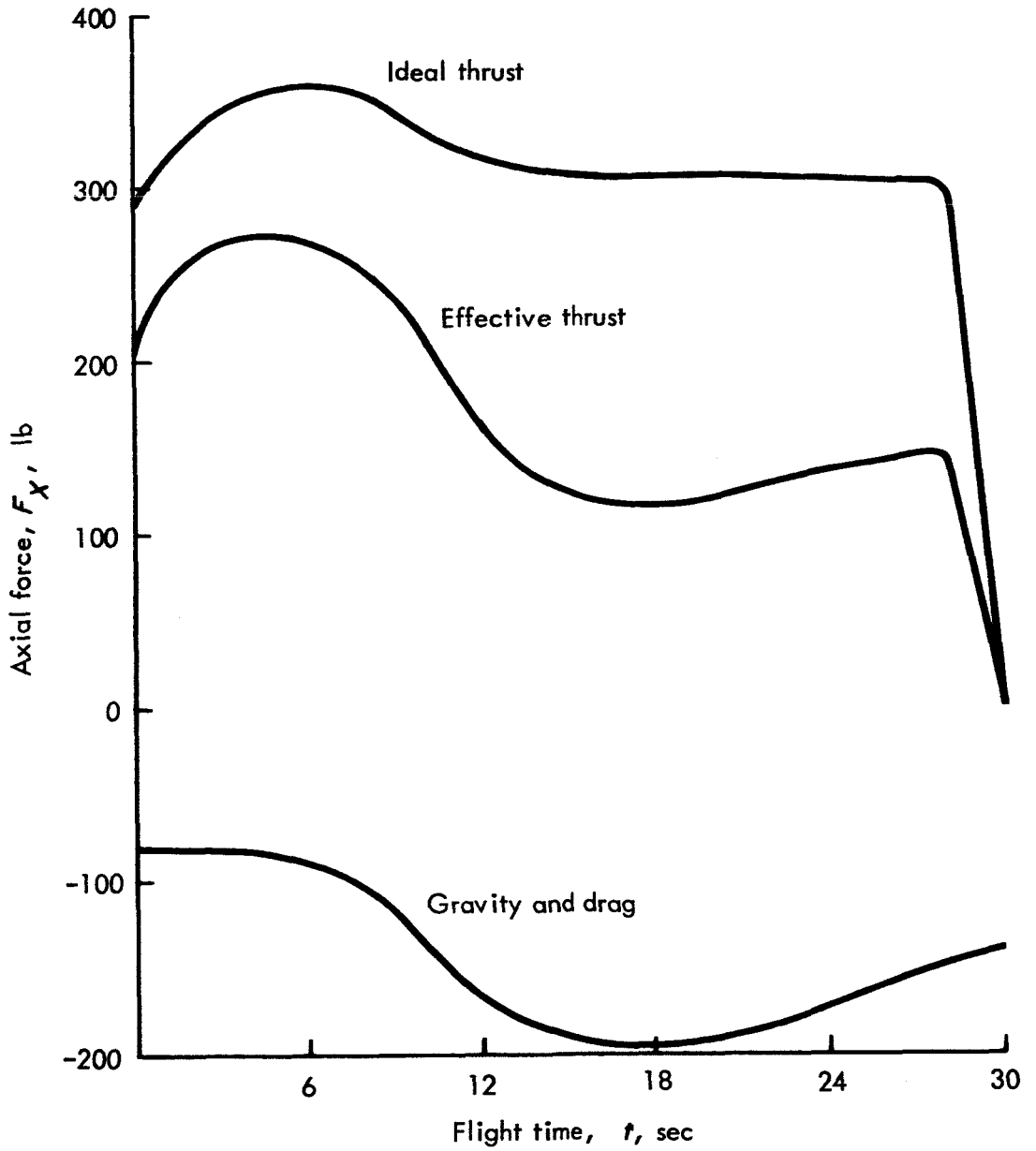

FIGURE 7. — *Axial-force components (total impulse = 9400 lb-sec; drag and gravity = 4415 lb-sec; net impulse = 4985 lb-sec; ideal velocity = 5250 ft/sec; velocity loss = 2389 ft/sec; actual velocity = 2861 ft/sec).*

determine the overall efficiency of the vehicle system. The drag loss and gravity loss are approximately 29 and 18 percent, respectively, of the ideal impulse, resulting in a net effective impulse of 53 percent of the ideal value.

These quantitative results appear to indicate a poor design regarding the efficiency of the system, but it is emphasized that rockets in the small thrust category such as the Bio-Space vehicle have inherently large impulse losses. Ideal and net impulse and the resulting ideal and actual velocity are given in figure 7.

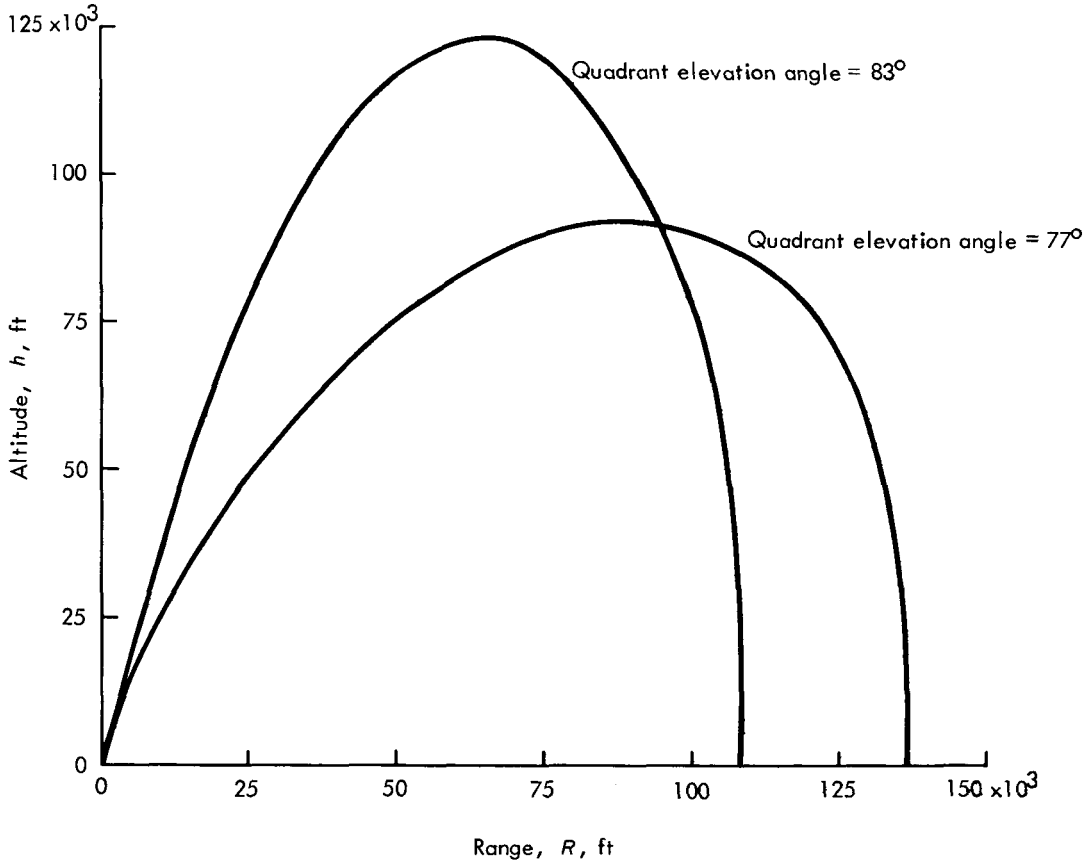

FIGURE 8. — *Launch angle variation for Bio-Space payload.*

TRAJECTORY VARIATIONS

Trajectory variation from a predicted nominal can be attributed to a combination of various factors including misalinement of the vehicle's fins and thrust axis, errors in wind compensation, error in launcher orientation and tip-off, variation in total effective impulse, and uncertainties in aerodynamic drag estimations. The end-burning Arcas with its characteristically low initial acceleration history is very susceptible to low-altitude wind effects. This inherent design-performance characteristic necessarily places emphasis on errors in wind compensation, resulting in nominal trajectory errors.

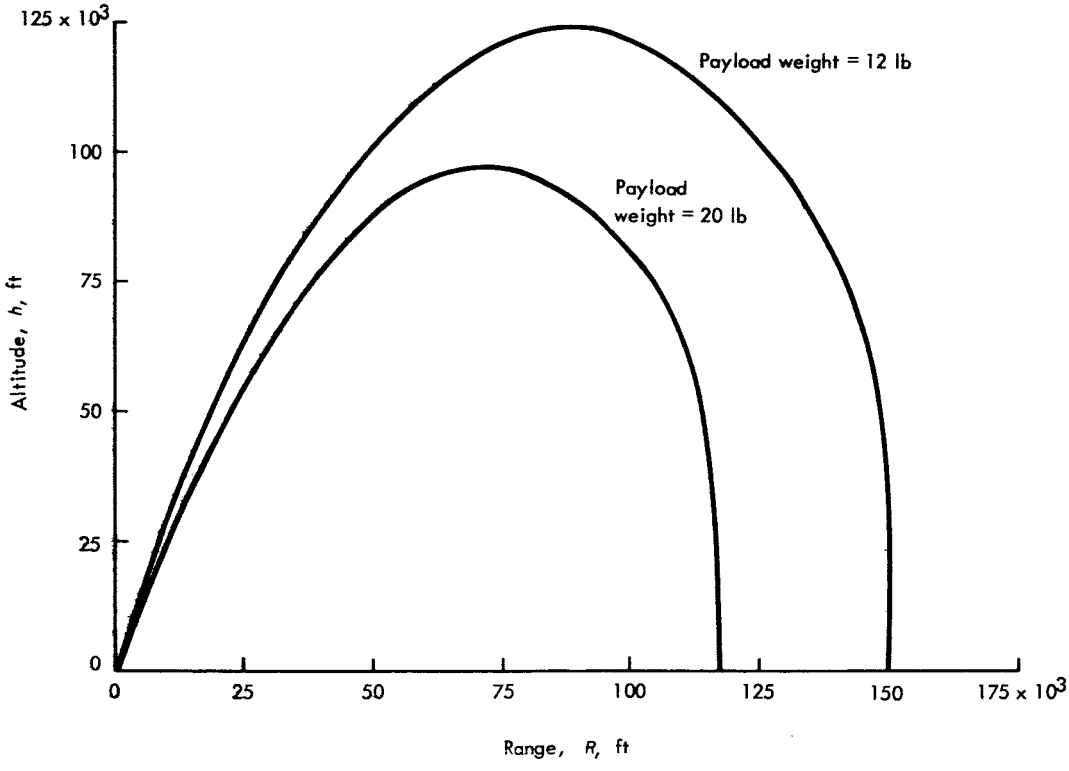

FIGURE 9. — *Payload weight effects (launch quadrant elevation angle = 80°).*

Since the Bio-Space program objectives did not dictate stringent trajectory criteria, the approach employed was to select a variation from nominal for the effective quadrant elevation angle that could be expected based on emperical data and experience. The payload and recovery system were then designed for an expected worst case in trajectory variation. Standard Arcas wind-weighting procedures and sensitivities were used for the Bio-Space configuration. Trajectory variations from the nominal are shown in figure 8.

Figure 9 is presented for potential use of the Bio-Space configuration with other experiments having net payload weights from 12 to 20 pounds.

RECOVERY SYSTEM PERFORMANCE

Theoretical parachute trajectory calculations were performed using a three-dimensional analysis on a flat earth. The computer program employed a two-step exponential atmosphere with 36 200 feet as the dividing altitude and included wind as a function of altitude. The time required for the falling recovery package to reach any given percentage of the horizontal wind velocity was determined. The assumption of constant horizontal and vertical ballistic factors was required. Horizontal displacements in the x and y directions were calculated and summed with respect to altitude.

The profile of the nominal, no-wind, recovery-package trajectory is shown in figure 5. Rate of descent and altitude as functions of descent time are shown in figure 10. The initial descent time of figure 10 is taken at event (6) of figure 5. The total descent time from parachute opening to water impact is 19 minutes, with a resulting payload terminal velocity at water impact of 38 ft/sec.

The nominal descent case does not consider wind effects, and the descent trajectory will degenerate into a pure vertical fall. However, since the relatively slowly falling recovery package is sensitive to winds, the translation in the horizontal plane of the descending payload and parachute was examined. Statistical wind data during the summer months obtained by the U.S. Weather Bureau were employed. The winds were considered up to an altitude of 90 000 feet, at which point it was assumed that the wind effects on the recovery-package descent trajectory would commence. A 95-percent

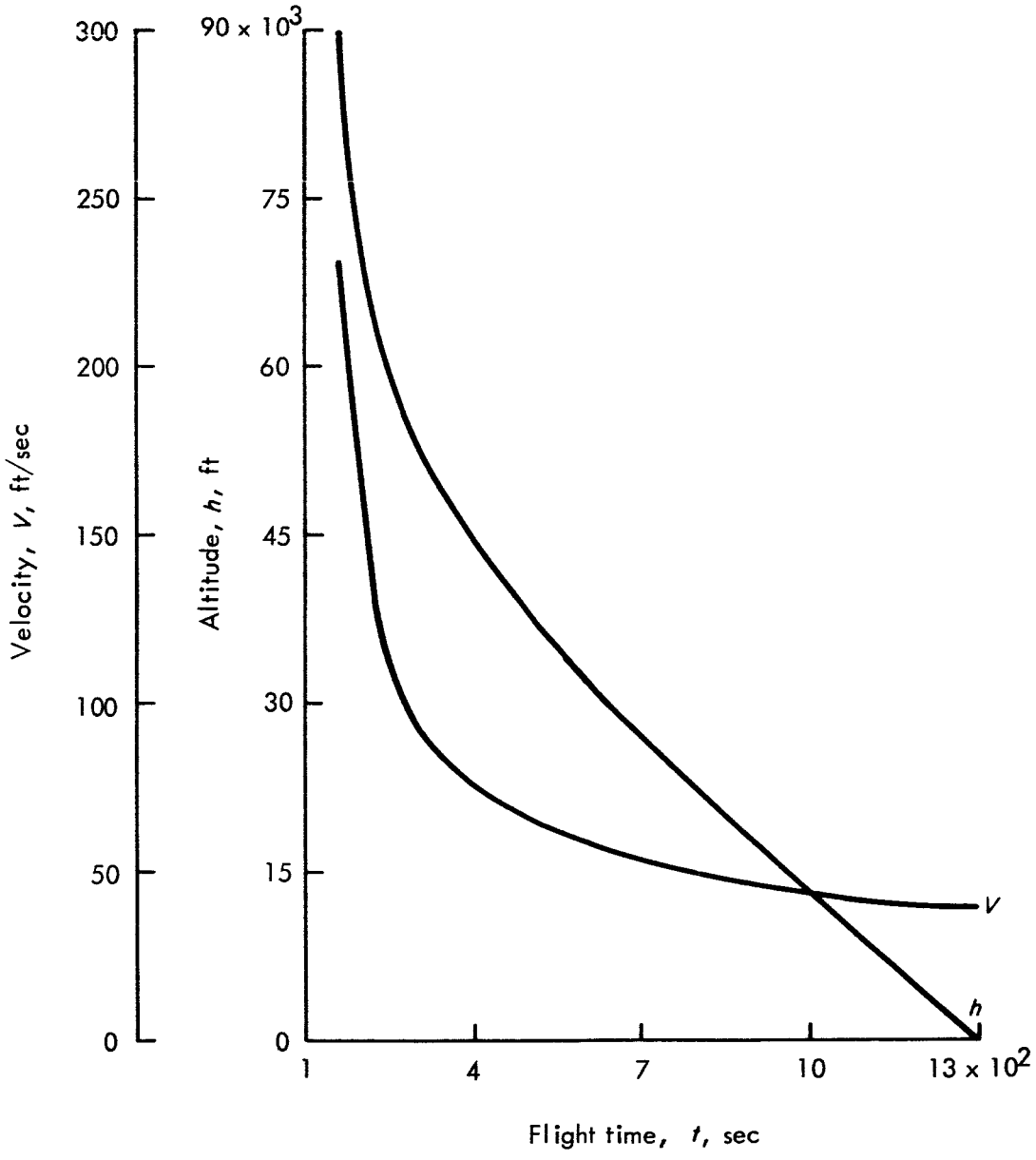

FIGURE 10. — *Recovery package descent (initial conditions taken at $t = 155$ sec; $h = 90\,000$ ft).*

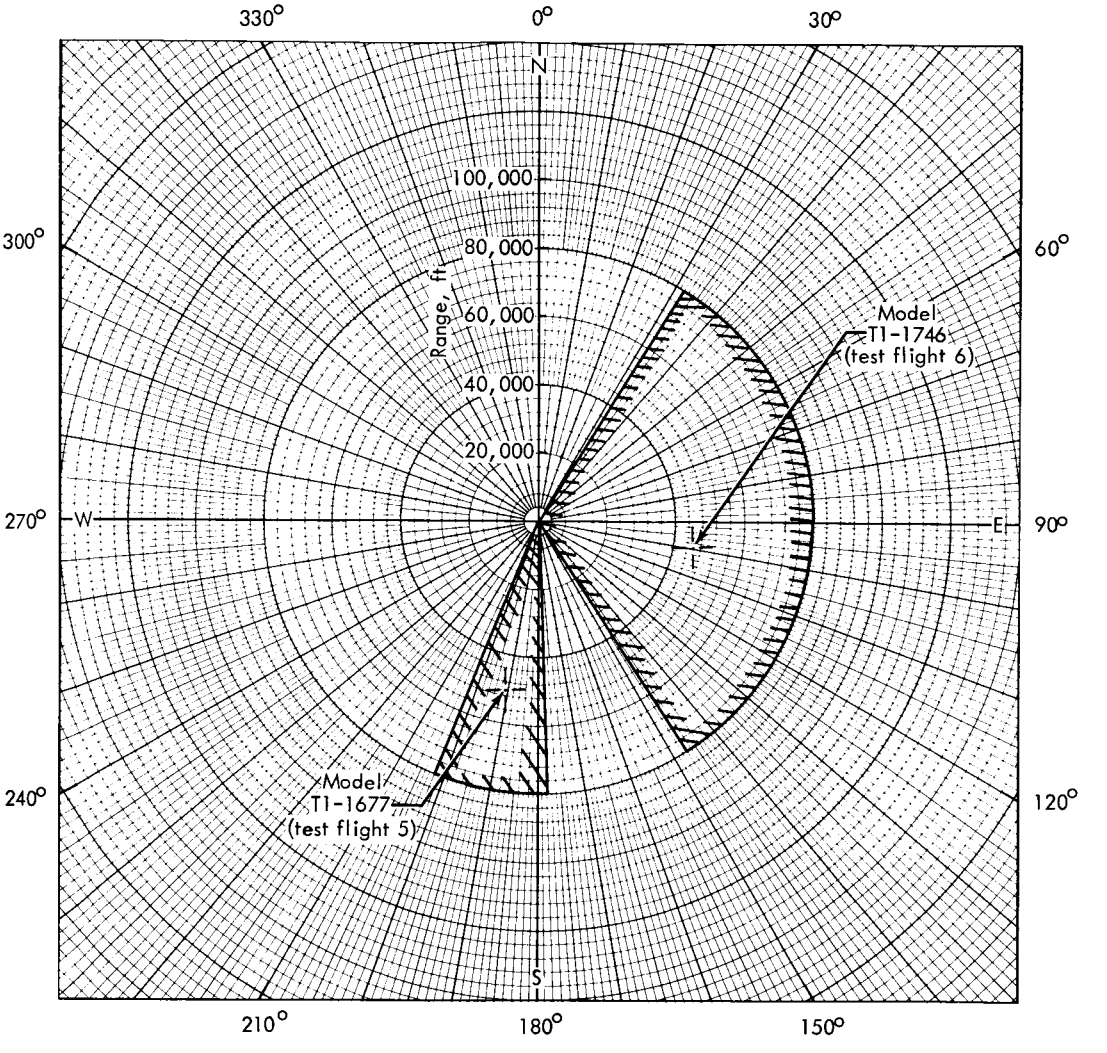

FIGURE 11. — *Parachute dispersion area; origin taken at 90 000 ft; probability: wind velocity = 3σ and wind direction = 95 percent.*

probability was used for wind-direction occurrence at various altitudes, whereas 3σ wind velocities obtained from reference 2 were used for the velocity-altitude profile. The resulting recovery-package dispersion area is shown in figure 11.

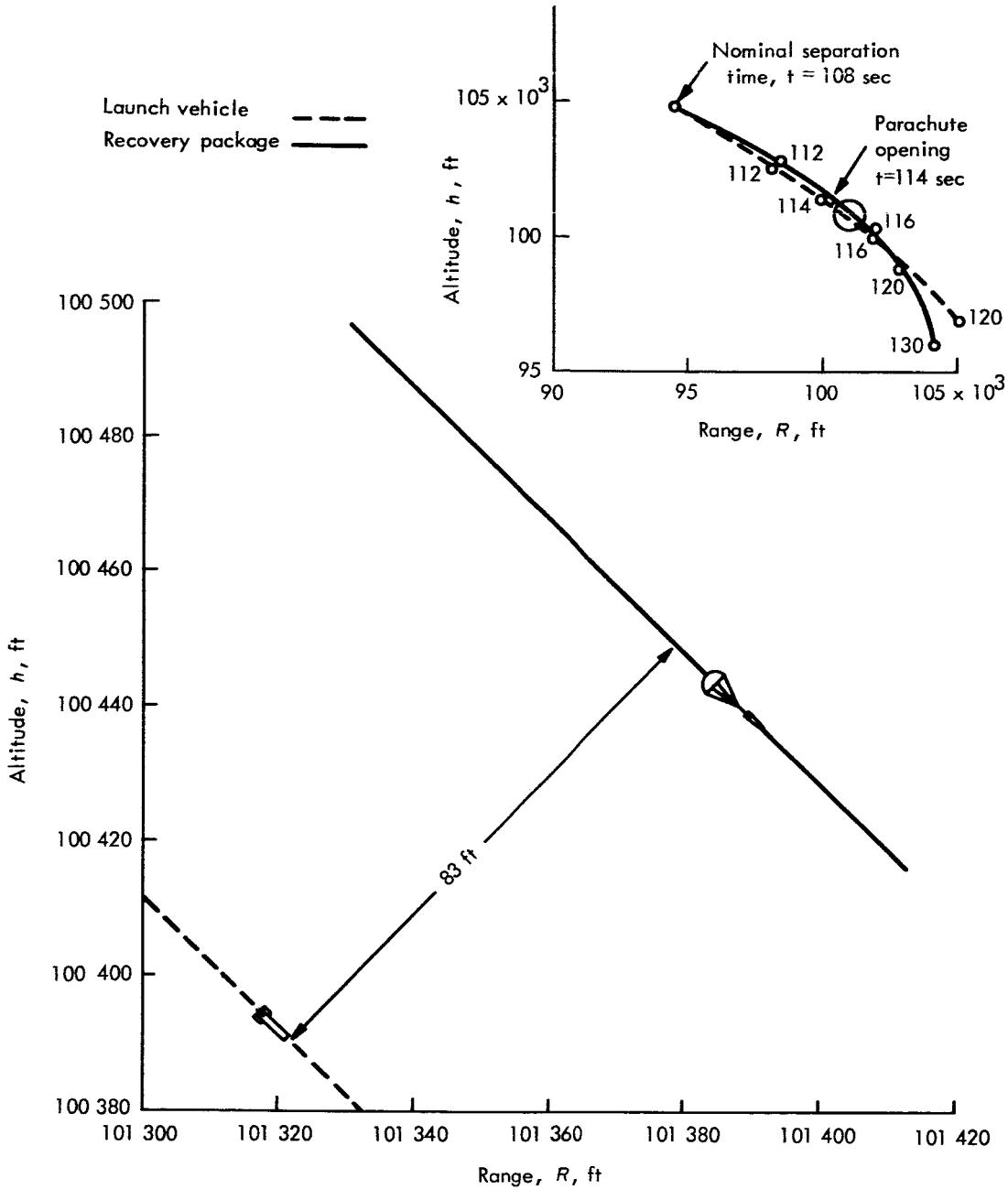

FIGURE 12. — *Nominal miss distance between launch vehicle and recovery package (miss distance obtained with stable launch vehicle lift and drag and 6-second parachute opening delay).*

LAUNCH-VEHICLE/RECOVERY-PACKAGE INTERFERENCE

Because the faster falling expended launch vehicle will eventually overtake the recovery package, there is danger that the motorcase may become fouled with the parachute or even make contact with the nose cone. The trajectories of the expended launch vehicle and the recovery package were examined after separation to determine the miss distance at the instant that the launch vehicle overtook the recovery package. Results of this analysis are shown in figure 12. The analysis does not consider the possibility of vehicle pitch orientation in the trajectory plane other than that along the flight path at separation. It is felt that, because of the high translational velocity of the vehicle along its flight path as compared with the induced velocity of separation, even a substantial launch-vehicle angle of attack would result in only a negligible change of the nominal recovery-package trajectory.

CHAPTER 3

Vehicle Aerodynamic Analysis

This section presents the aerodynamic characteristics of the Arcas Bio-Space vehicle configuration. The vehicle components are considered separately as follows: nose/body, fins, and boattail.

As seen in figure 1, the nose/body is composed of a tangent ogive with a fineness ratio of 4.0 and a cylinder with a fineness ratio of 18.53. The fin geometry is also presented in figure 1. The fins employ a diamond airfoil section with a root thickness-to-chord ratio of 0.048 and surface area of 23.38 square inches per panel. The boattail has a fineness ratio of 0.83 and a half-apex angle of 15.5°.

In the following sections, a progressive aerodynamic analysis is made: first of the various components, and then of the composite vehicle. The basic parameters are determined first, and then they are utilized in the investigation of the static and dynamic flight characteristics of the vehicle.

BASIC AERODYNAMIC PARAMETERS

Axial Force

The axial force acting on the vehicle in flight is composed of the following: skin friction drag, nose wave drag, fin wave drag, boattail wave drag, and base pressure drag.

The skin friction drag of the body and fins was obtained from reference 3. Subsonic data were based on a turbulent boundary-layer condition. The friction drag is presented in figure 13 as a component of the total drag.

The nose-wave drag was obtained from reference 3 which is based on slender-body theory. This drag is composed of the forebody drag and the interference drag of the forebody and center section of the afterbody (cylinder). The fin wave drag was obtained from references 3 and 4 and is based

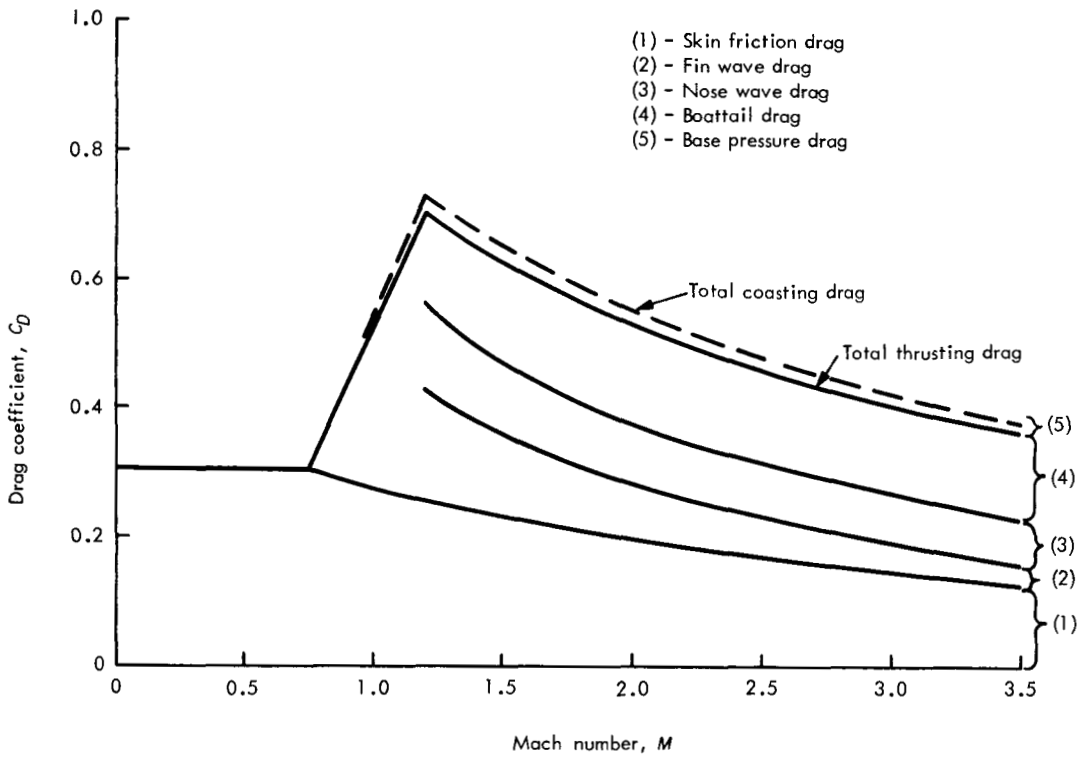

FIGURE 13. — *Component drag coefficients (based on $S_R = 0.11$ ft²).*

on linear theory. The theory applies to sharp-nosed airfoil sections and utilizes the "Mach-cone" concept. The wave-drag contributions are also shown in figure 13.

The drag of a vehicle might be reduced by the use of a boattail. With a boattail afterbody the base area is reduced, and thus a decrease in base drag is realized. However, the decrease in base drag may be nullified by the boattail wave drag. The boattail wave drag was obtained from reference 5 which utilizes experimental data. This drag contribution is shown in figure 13.

At Mach numbers greater than 1, the base of the vehicle experiences a negative pressure, relative to free-stream conditions, resulting in an increase in total vehicle drag. For the non-thrusting condition, the area involved is the total vehicle-base area. However, during the thrusting period, the area in-

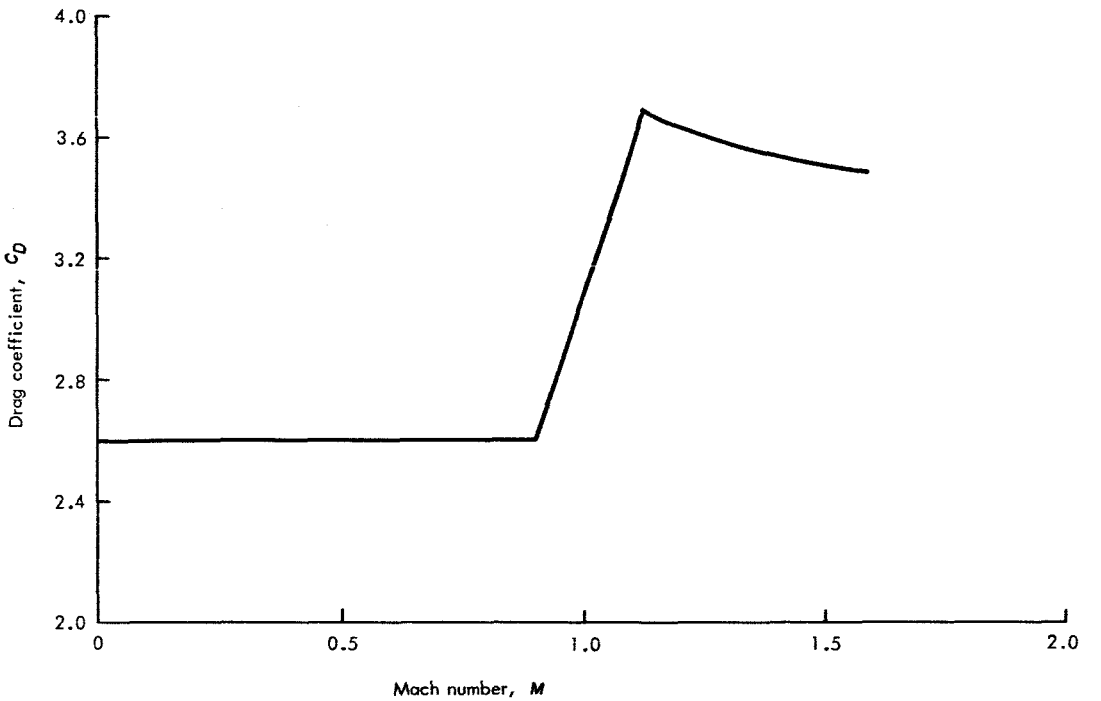

FIGURE 14. — *Drag of expended launch vehicle* ($S_R = 0.11$ *ft*^{2}).

cluded in the vehicle nozzle is not considered. Because the Arcas motor case is sharply boattailed resulting in a small base area with the exception of the nozzle region, the base drag is neglected during thrusting. The base drag during the coasting period obtained from the empirical data from reference 3 is shown added to the total thrusting drag in figure 13.

The drag of the expended launch vehicle was theoretically estimated by using the data discussed previously for the coasting configuration without the ogival nose drag and by adding the drag exhibited by a blunt, recessed front end. These data were later corrected to conform to observed data regarding flights of developmental vehicles and are presented in figure 14.

The components considered to be contributing to the aerodynamic drag of the recovery system are as follows:

(1) Nose cone and reefed parachute
  (a) Nose cone skin friction drag
  (b) Reefed parachute drag
  (c) Nose wave drag

(2) Nose cone and open parachute
  (a) Nose-cone skin friction drag
  (b) Open parachute drag

The drag for the above cases was estimated from the data of reference 6. The open parachute drag was corrected by using observed test data from developmental tests. It was observed that the ballistic factor for the recovery package in vertical, free-fall flight was

$$\frac{W}{C_D S} = 1.4$$

The drag coefficients for the recovery system are shown in figure 15. These data were utilized in investigating miss distances of the separating bodies (payload/parachute and expended launch/vehicle) for potential collision.

Normal Force

The normal force characteristics of the vehicle were obtained from experimental data if available and theoretical data where applicable.

The lift-curve slope for the nose/body was obtained from second-order shock-expansion methods (refs. 3, 7, and 8) and modified according to empirical data on similar body shapes (refs. 9 and 10). The normal-force derivatives for the nose/body at zero angle of attack is presented in figure 16. It is noted that the experimental data indicated higher lift characteristics, especially during the high subsonic and transonic regions.

The fin three-dimensional subsonic lift-curve slope is predicted by modified lifting-line theory (ref. 3). This method provides lift-curve slopes that are accurate for low aspect-ratio fins as applied to the subject configuration.

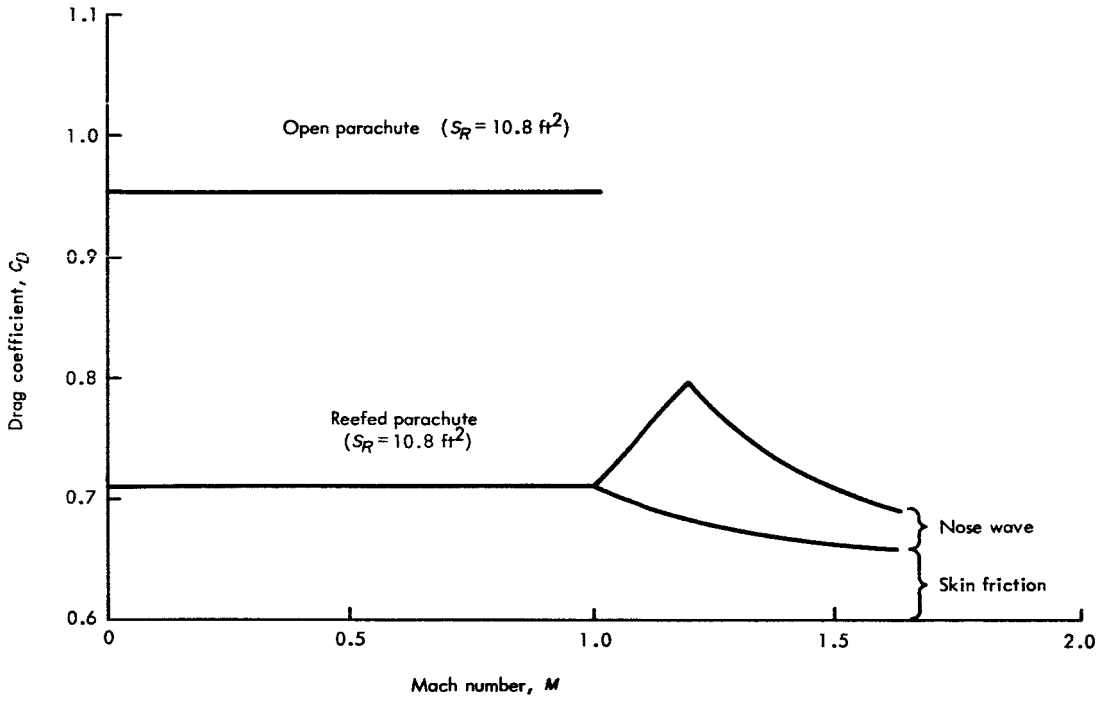

FIGURE 15. — *Recovery system drag.*

The transonic characteristics of fins are difficult to predict; therefore, transonic fin lift data used were determined from experimental data from wind tunnel tests (ref. 3). Because of the low aspect ratio and the small fin-thickness ratio, the transonic fin lift-curve slope has a relatively smooth transition in this region. The fin lift characteristics are shown graphically in figure 16. These values are given for two panels in one plane with fin-body interference factors included.

A fin-body interference factor $(K_f)_b + (K_b)_f$ of 1.3 was assumed constant for all Mach numbers in determining the lift characteristics of the fin-body combination. It can be seen from figure 1 that the fins are in the presence of a cylinder-boattail body configuration. Prediction of fin-body interference was difficult because data were not available for the boattail body effects on the fin lift characteristics, or for the fin effects on the boattail. The method for determining the fin-body interference (refs. 3 and 11) is

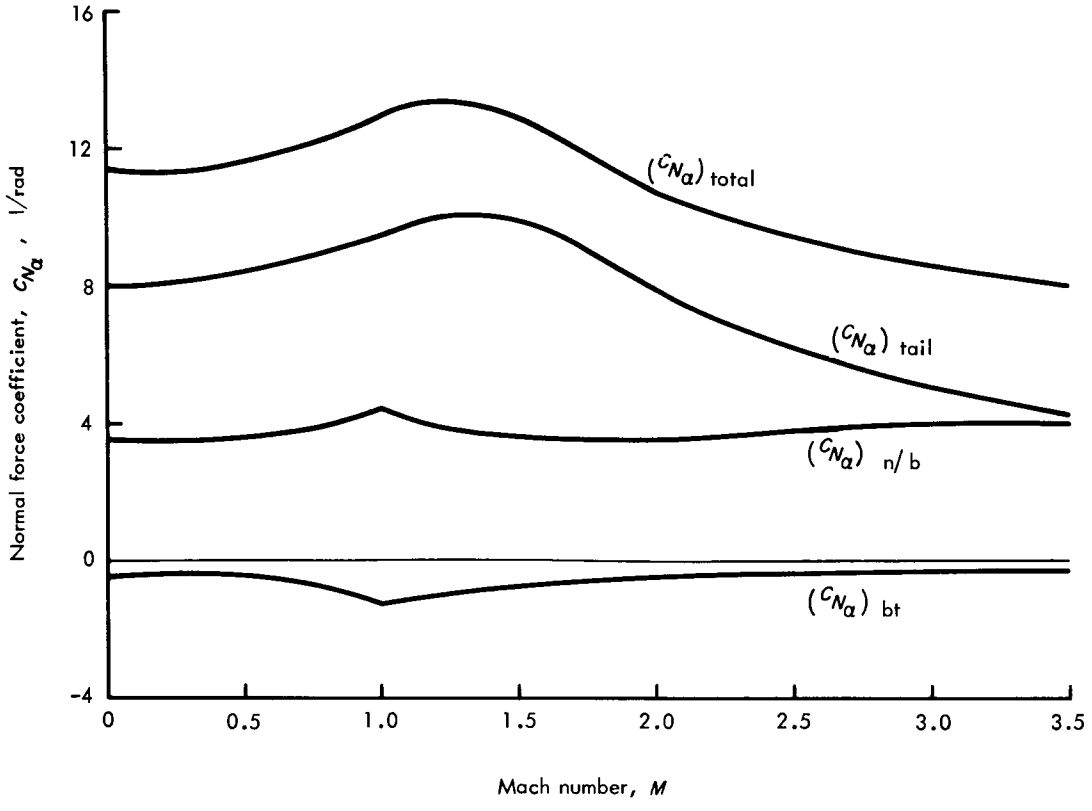

FIGURE 16. — *Normal force coefficients (based on $S_R = 0.11$ ft^2 and $d = 0.375$ ft).*

limited to fins in the presence of a cylindrical body only. Also, there is some question as to the validity of the interference factor in the transonic flight regime as predicted by slender-body theory. Other approximate methods (ref. 12) indicate conflicting results with respect to slender-body theory. In the light of the variation of interference factors in the subsonic and transonic regions and the unknown interference effects between the fin and boattail, it appears conservative to estimate the interference factor somewhat lower numerically than that predicted by theory. A more accurate determination of the fin body interference would require wind-tunnel tests.

The boattail lift-curve slope is shown in figure 16 as a function of Mach number. The supersonic values were obtained directly from experimental

data (refs. 5, 13, and 14). The subsonic boattail lift characteristics were found from the assumption of cone-frustrum reversibility (ref. 3), and transonic region values were estimated by observing the nature of the low supersonic data. These data indicate a much larger negative lift influence than that predicted by slender-body theory with the assumption of reversibility.

The data as discussed above for the nose/body, tail, and boattail, all plotted in figure 16, may be compiled to represent the normal force characteristics of the total vehicle.

$$(F_N)_{total} = (F_N)_{nose/body} + (F_N)_{tail} + (F_N)_{boattail} \tag{1}$$

but

$$F_N = \frac{C_{N_\alpha}\, \alpha\, \rho V^2}{2} S_R$$

thus:

$$(C_{N_\alpha} S_R)_{total} = (C_{N_\alpha} S_R)_{n/b} + (C_{N_\alpha} S_R)_{tail} + (C_{N_\alpha} S_R)_{bt} \tag{2}$$

The component data shown in figure 16 are entirely based on $S_R = \pi d^2/4$, where d is the cross-section diameter of the cylindrical body section. Therefore, the total vehicle normal-force curve slope may be directly added as follows:

$$(C_{N_\alpha})_{total} = (C_{N_\alpha})_{n/b} + (C_{N_\alpha})_{tail} + (C_{N_\alpha})_{bt} \tag{3}$$

The total vehicle lift coefficient based on S_R is also included in figure 16.

Center of Pressure

The subsonic center of pressure acting on the ogive-cylinder combination is found by considering potential flow over the forward part of the body with the addition of viscous cross flow over the after part (ref. 3). Slender-body theory states that this method is applicable in the transonic region also; however, experimental data (ref. 9) indicate center-of-pressure locations somewhat farther aft on the body than those found theoretically. The supersonic center of pressure may be found theoretically from the second-order shock-

expansion method (refs. 3, 7, and 8) which agrees well with experimental data at the higher Mach numbers.

The data used to determine the nose/body center of pressure as presented in figure 17 were derived from these theoretical methods, modified in the Mach number range of 0.5 to 2.0 to conform to observed experimental data for similar nose/body shapes.

The fin aerodynamic center was determined by using an empirical method by which a large number of experimental data points from many sources are used in constructing curves between theoretically determined limits (ref. 3). The fin center of pressure is plotted as a function of Mach number in figure 17. In considering interference effects between the fins and the body, it is assumed that the center of pressure for the basic fin alone is valid for the fin in the presence of the body.

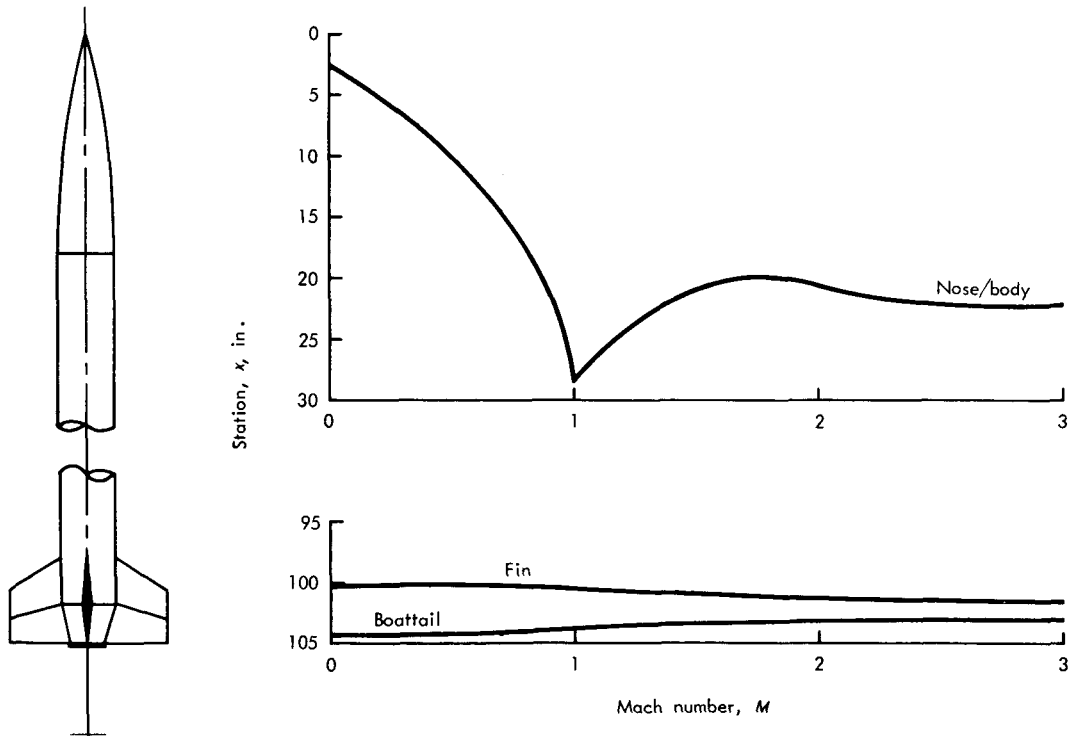

FIGURE 17. — *Center-of-pressure locations.*

The supersonic boattail center of pressure location was interpreted from experimental distributed lift data (ref. 5). Due to the lack of experimental data for the subsonic and transonic flight regimes, the center of pressure location was estimated using the assumption of subsonic reversibility and data trends at low supersonic Mach numbers. The resulting data are shown in figure 17.

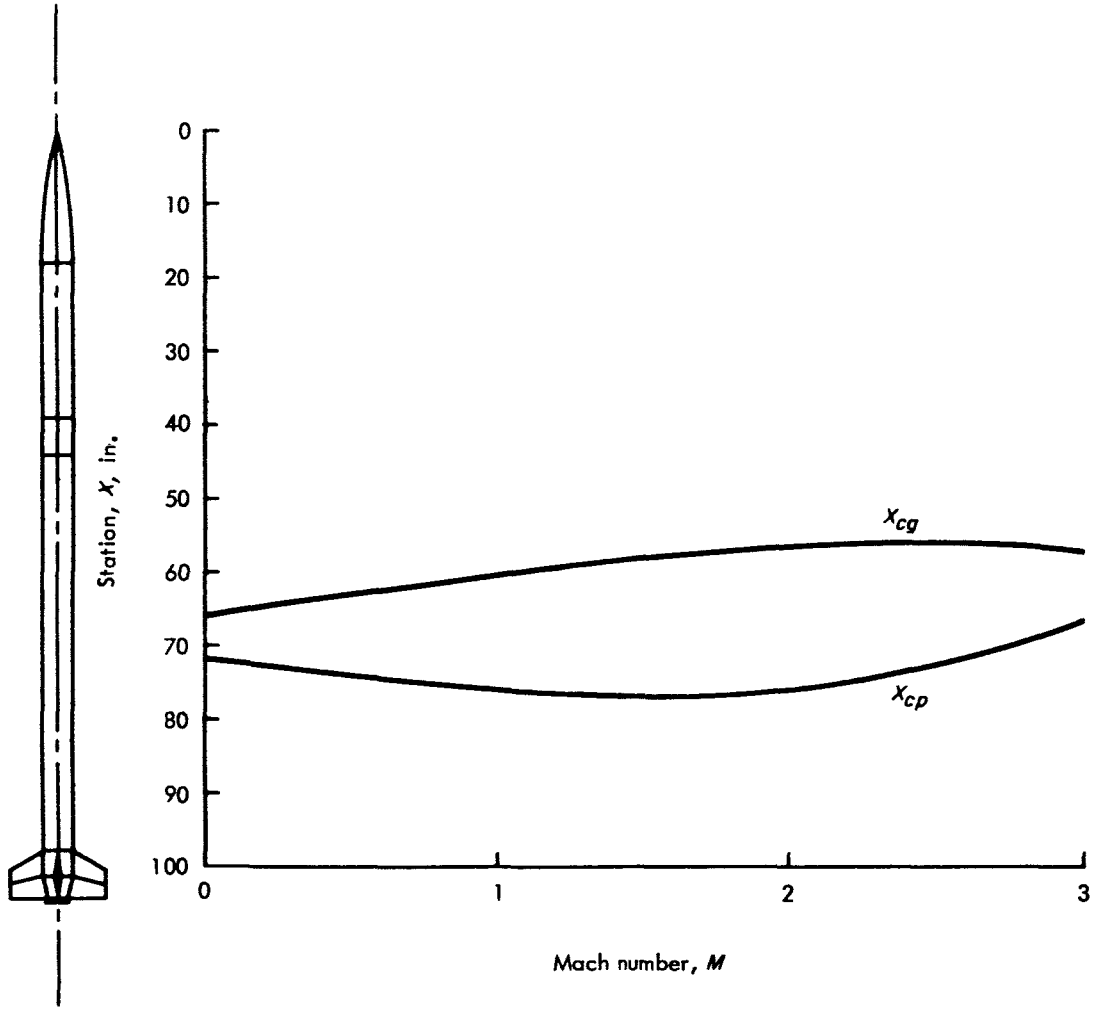

FIGURE 18. — *Center of gravity and center of pressure locations.*

The composite vehicle center of pressure location, relative to any reference position, may be determined from the component data by summing moments about the chosen reference position as follows:

$$(F_N)_{total}\,(x_{cp})_{total} = \sum_n F_{N_n}\,(x_{cp})_n \tag{4}$$

or

$$(C_{N_\alpha})_{total}\,(x_{cp})_{total} = \sum_n (C_{N_\alpha})_n\,(x_{cp})_n \tag{5}$$

Thus,

$$(x_{cp})_{total} = \frac{\sum_n (C_{N_\alpha})_n (x_{cp})_n}{(C_{N_\alpha})_{total}} \tag{6}$$

The subscript n denotes the various vehicle components whose normal force and center of pressure locations have already been determined.

The total vehicle center of pressure location is presented in figure 18, plotted as vehicle station location against Mach number. It is noted that the

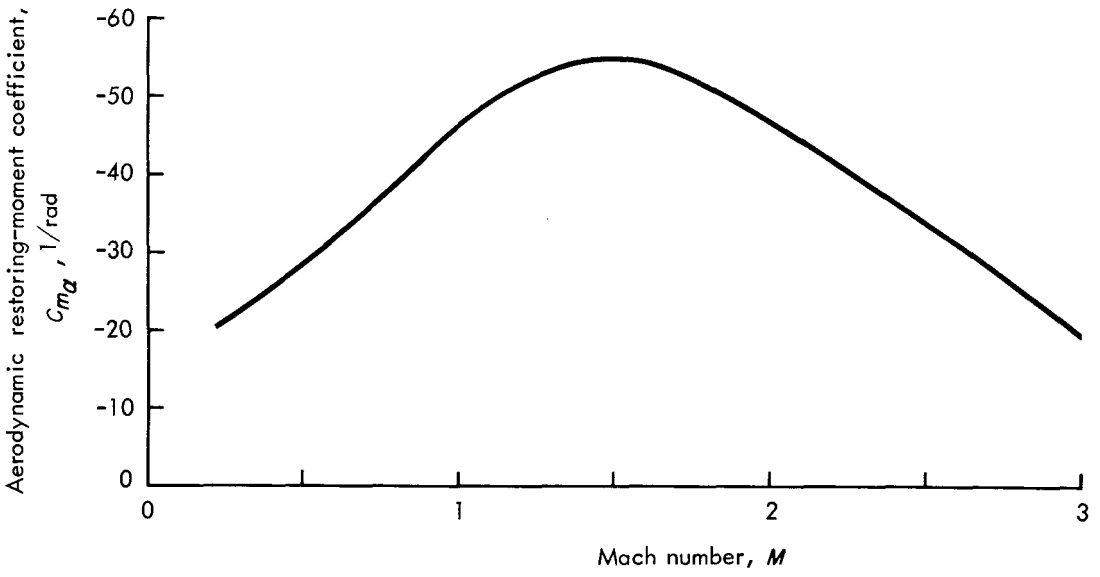

FIGURE 19. — *Restoring moment coefficient (based on $S_R = 0.11$ ft² and $d = 0.375$ ft).*

total vehicle center-of-pressure locations, as well as those of the various vehicle components, are presented relative to the vehicle nose tip (station 0.0).

Aerodynamic Restoring and Damping Moments in Pitch

In order to determine the static and dynamic stability exhibited by the vehicle, which will be discussed later, the aerodynamic pitching moments, both restoring and damping, were determined.

The aerodynamic restoring moment, which exists only if the vehicle experiences an incidence angle, is simply the resulting normal force due to this incidence multiplied by its moment arm. Since a missile in flight rotates about its center of gravity, the moment arm is the distance between the total center of pressure, where the normal force acts, and the vehicle center of gravity. Thus, the restoring moment is expressed as

$$M_Y = - F_N (x_{cp} - x_{cg}) \tag{7}$$

where x_{cp} and x_{cg} are measured relative to the nose and the negative sign indicates a nose-down moment. Equation (7) may be rewritten as

$$M_{Y_\alpha} = - F_{N_\alpha} (x_{cp} - x_{cg})$$

or

$$C_{m_\alpha} = - C_{N_\alpha} \frac{(x_{cp} - x_{cg})}{d} \tag{8}$$

The value of C_{m_α} may be determined from known aerodynamic data and the vehicle center-of-gravity location. The restoring-moment coefficient slope is presented as a function of vehicle Mach number in figure 19.

The pitch damping moment coefficient, which results from induced incidence angles on vehicle components caused by pitching velocity, is given by

$$C_{m_q} = -2 \sum_n \left(C_{N_\alpha}\right)_n \left(\frac{x_{cp} - x_{cg}}{d}\right)_n^2 \tag{9}$$

where the subscript n denotes the various vehicle components affected by the pitching velocity.

However, the effectiveness of the damping moment is reduced as a result of the lag in the development of the flow field as the vehicle experiences an orientation change with respect to the relative flow. This results in a moment, known as the lag moment, which is expressed in coefficient form (ref. 15):

$$C_{m_{\dot{\alpha}}} = 2 \sum_n \left(C_{N_\alpha}\right)_n \left[\frac{(x_{cp} - x_{cg})\, X}{d}\right]_n \tag{10}$$

where X is the position of instantaneous flow reaction, which is dependent on vehicle component. The values of X used in this paper are as follows:

Component	*X*
Nose/body	Nose tip
Tail	Fin root leading edge
Boattail	Fin root leading edge

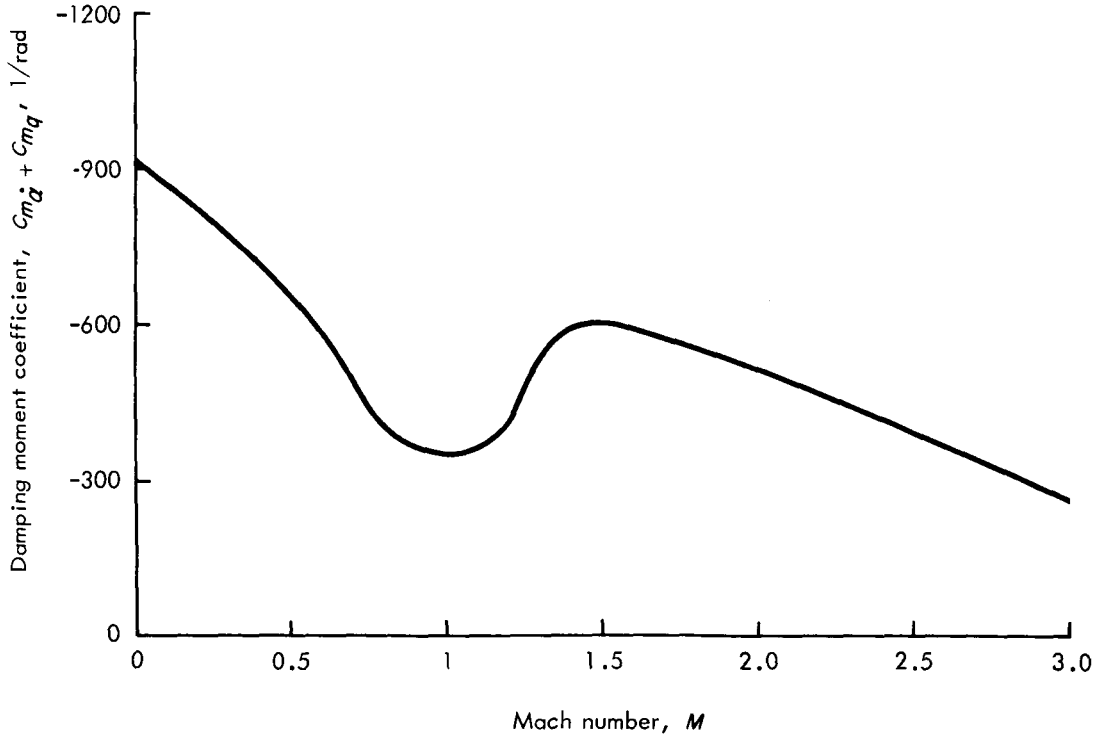

FIGURE 20. — *Damping moment coefficient (based on $S_R = 0.11$ ft² and $d = 0.375$ ft).*

Therefore, the effective damping contribution due to pitching velocity can be represented by

$$C_{m_q} + C_{m_{\dot{\alpha}}}$$

and is presented in figure 20.

Another damping contribution when the vehicle exhibits a pitching velocity is due to the Coriolis accelcration of the gas particles in motion within the motor. The method used to determine this damping contribution is obtained from reference 16, modified for use with end-burning motors. The term is presented in figure 21 as a pitching moment per unit pitching velocity $(M_{Y_q})_j$.

Roll Derivatives

The equation of motion for vehicle roll is expressed as

$$I_x\dot{p} = \sum M_X \tag{11}$$

The following moments comprise $M_{X,\,total}$:

(1) Roll driving moment, M_{X_δ}

(2) Roll damping moment, M_{X_p}

(3) Induced moment, $(M_X)_{\phi,\eta}$

Generally speaking, the driving moment is positive whereas the damping moment is negative. However, the induced moment may be positive or negative, depending on roll orientation with the incidence flow and the magnitude of this incidence. From equation (11), it is seen that the induced moment is important in determining the sign of $\dot{p}$, assuming that the driving and damping moments are nearly equal in magnitude, which is usually the case for slow-roll vehicles. However, due to the lack of data, both theoretical and experimental, the induced moment is not presented here.

The roll driving moment is determined from linear fin lift characteristics including fin/body interference factors. The roll driving moment for four fins is given as

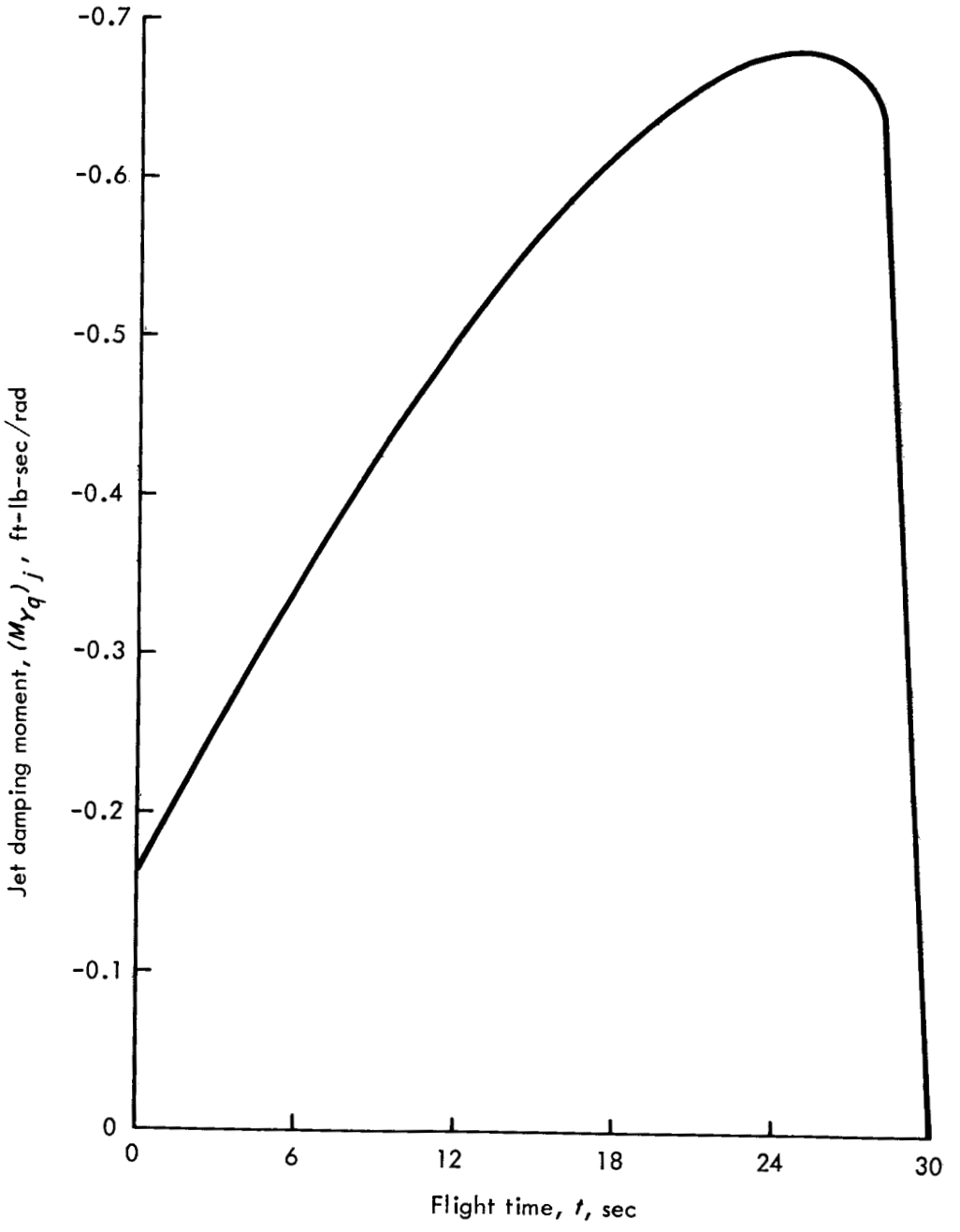

FIGURE 21. — *Jet damping moment.*

$$C_\ell = 2\left(C_{N_\alpha}\right)_{tail} \frac{\bar{y}}{d} \delta \tag{12}$$

Defining

$$C_{\ell_\delta} = \frac{\partial C_\ell}{\partial \delta}$$

equation (12) becomes

$$C_{\ell_\delta} = 2\left(C_{N_\alpha}\right)_{tail} \left(\frac{\bar{y}}{d}\right) \tag{13}$$

The value at the effective moment arm, $\bar{y}$, was assumed to be the mean aerodynamic chord, $\bar{c}$. The roll driving moment coefficient, C_{ℓ_δ}, is presented in figure 22 plotted against Mach number.

The roll damping moment, due to the existence of induced incidence angles on each element of fin surface, is determined by strip integration theory. The induced angle of attack at any point y along the span can be expressed as

$$\Delta \alpha = \frac{py}{V} \tag{14}$$

Defining

$$C_{\ell_p} = \frac{\partial C_\ell}{\partial \left(\frac{pd}{2V}\right)}$$

the roll damping moment coefficient for four fin panels may be expressed as

$$C_{\ell_p} = 4\left(C_{N_\alpha}\right)_{tail} \left(\frac{\bar{y}}{d}\right)^2 \tag{15}$$

The roll damping moment coefficient is also presented in figure 22 as a function of Mach number.

STATIC AERODYNAMIC STABILITY

The total vehicle center of pressure and the vehicle mass center are presented in figure 18. From these data, the vehicle static margin may be calculated. The static margin measured in calibers is defined as

$$\text{Static margin} = \frac{(x_{cp} - x_{cg})}{d} \tag{16}$$

The static margin is presented in figure 23 as a function of flight time.

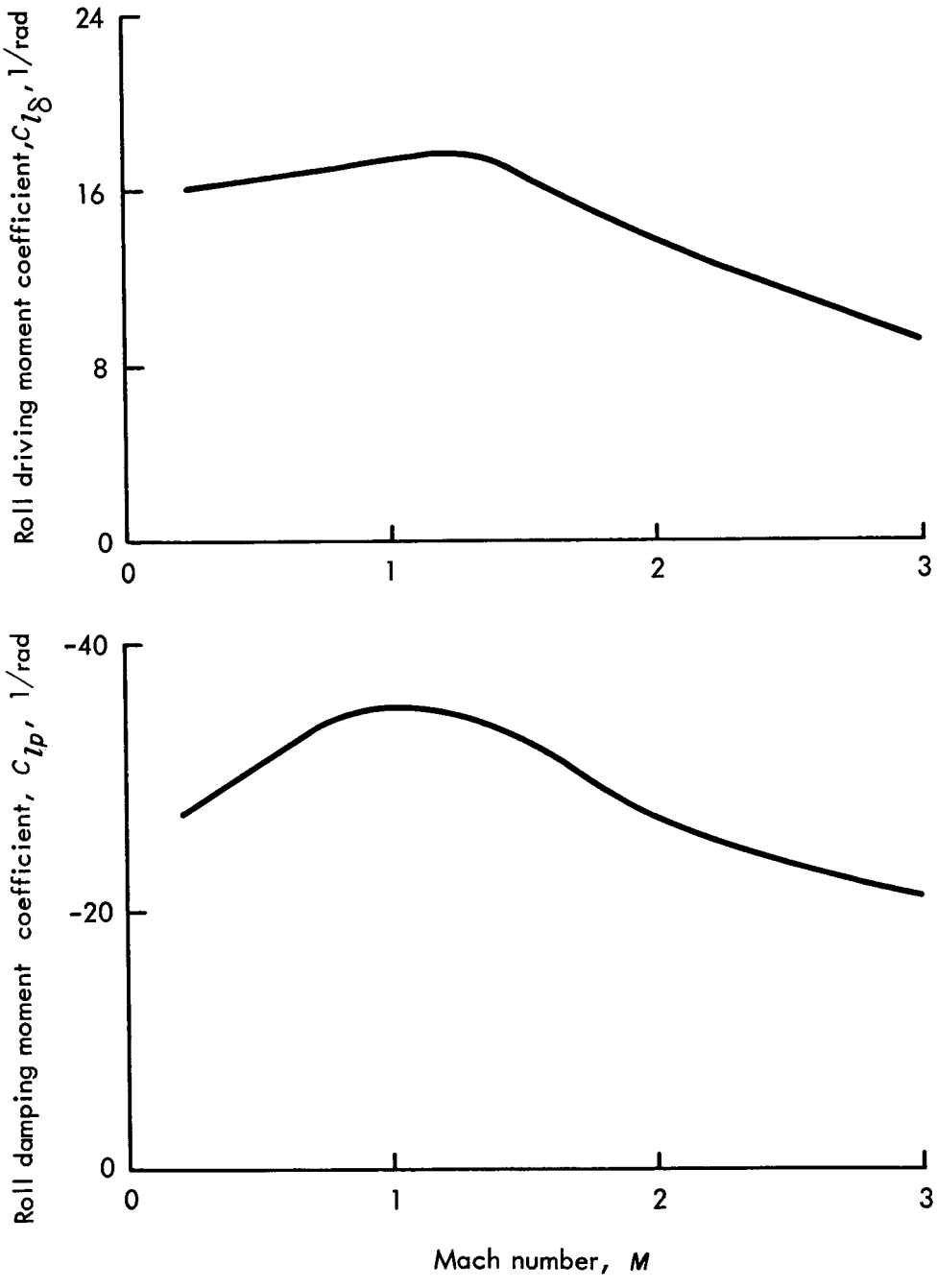

FIGURE 22. — *Roll derivatives (values are for four fins based on $S_R = 0.11$ ft² and $d = 0.375$ ft).*

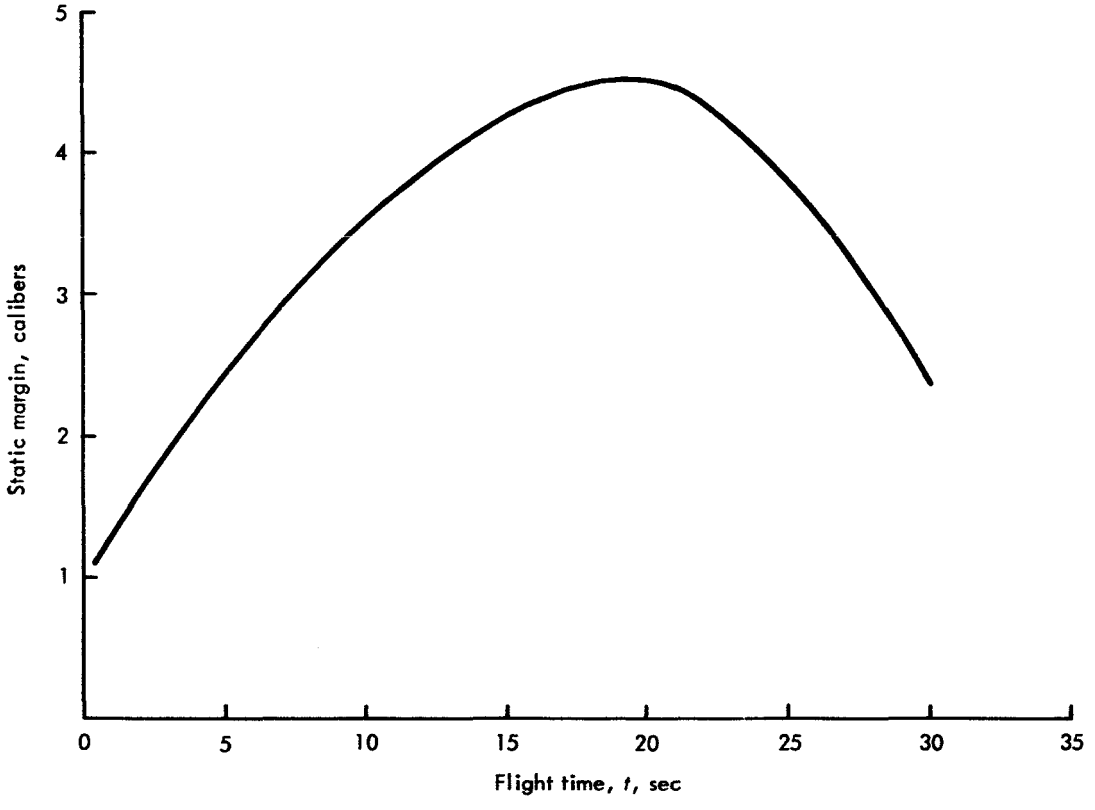

FIGURE 23. — *Static margin.*

From figure 23, it is seen that the static margin ranges in value from approximately 1.1 to 4.5 calibers, depending on the vehicle aerodynamic environment.

DYNAMIC AERODYNAMIC STABILITY

In order to insure a dynamically stable flight vehicle, the dynamic motion of the vehicle must be investigated. Since the vehicle motion, and hence the resultant incidence, is influenced by various vehicle dynamic properties, these properties should be analyzed in detail.

A representation of the vehicle motion can be obtained by projecting the total vehicle motion on the pitch plane. This will indicate vehicle incidence during flight when the pitching motion experiences maximum magnitudes.

Natural Pitch Frequency

The undamped pitch natural frequency is derived from the equations of motion describing the pitching and translational motion of the vehicle and is approximately given by

$$\omega_n = \left(\frac{M_{V_\alpha}}{I_y}\right)^{1/2} \tag{17}$$

This is the frequency at which the vehicle will oscillate due to the restoring characteristics of the aerodynamic environment, with no damping considered.

Roll Motions

A flight vehicle can easily be destroyed by a dynamic resonant phenomenon known as pitch-roll coupling. Pitch-roll coupling is a resonant instability which is encountered when any disturbance frequency is close in magnitude to the vehicle natural pitch frequency. The magnitude of the resultant instability depends on the size of the undisturbed trim and the nature of the vehicle aerodynamic properties. In effect, the vehicle undisturbed trim is magnified, with a maximum occurring when the disturbance frequency is at the natural frequency. Since all vehicles possess some type of asymmetry which produces the undisturbed trim and since the disturbance frequency is represented by the roll rate, the problem is how to avoid the potentially serious results of this coupling.

The only alternatives are to insure that the roll rate does not approach the natural frequency or, if this solution is not feasible, to insure that either the time involved is kept to a minimum to prevent an appreciable increase in the amplitude of motion or that the time of approach during flight occurs at a relatively low altitude. The resonant motions require time to build up even with no damping. Care should be taken in choosing the resonance time since the amplitude of motion is generally increased a fixed amount each revolution. Thus, for high frequencies the amplitude builds up faster.

It is shown in a subsequent section that the magnitude of the incidence is a direct function of the damping available and that the magnification of the non-rolling trim at resonance increases rapidly with altitude. The conclusion is that if a roll rate cannot be selected which keeps the vehicle out of the roll-resonance region, then a roll rate must be selected which allows the vehicle to pass through the roll-resonance region at a time determined by a trade-off between the time-limitation approach and the low-altitude approach.

Roll Rate Program

An investigation of the natural frequency characteristics of the subject configuration reveals the undesirability of a low-altitude resonance crossing. Therefore, as shown in figure 24, a maximum roll rate at burnout of 4 cps was decided upon as the first priority roll program. This rate appears desirable because the roll-rate curve crosses the pitch frequency at a time when the roll rate is rapidly accelerating while the pitch frequency is decreasing. Consequently, the crossing time involved is kept to a minimum.

As an alternative to the 4-cps maximum roll-rate program, it was decided to use a 20-cps maximum roll-rate program to avoid resonance completely. This was chosen mainly because previous flights of similar vehicles had proven successful with a maximum roll rate of 20 cps. Also, experiments had shown that the animal specimen could sustain the high roll velocities involved.

Both of these roll programs are considerably below the vehicle first structural mode; hence no structural resonance problems are foreseen.

The roll-rate values presented in figure 24 are obtained from the roll equation of motion

$$I_x \dot{p} = \sum M_X$$

or

$$I_x \dot{p} = \overset{(+)}{C_{l_\delta}}(\delta) q S d + \overset{(-)}{C_{l_p}} \left(\frac{pd}{2V} \right) q S d \tag{18}$$

The negative sign above C_{l_p} in equation (18) indicates that the roll damping

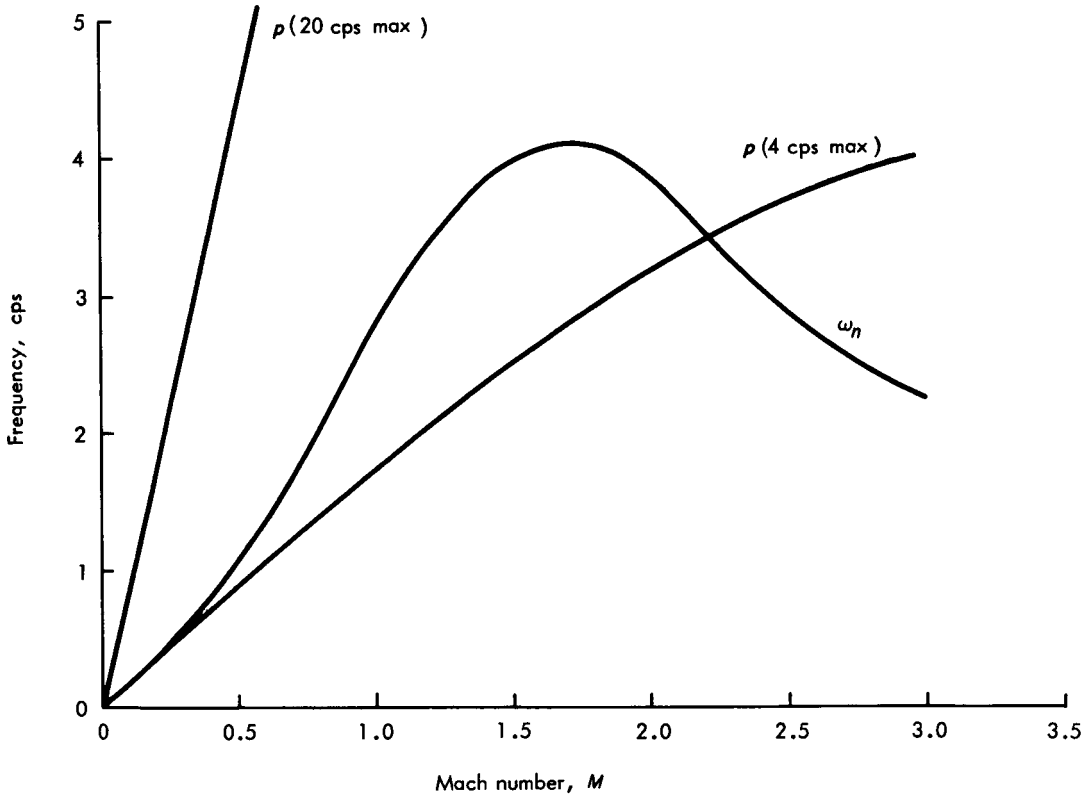

FIGURE 24. — *Natural frequency and roll rates.*

moment coefficient opposes the roll driving moment coefficient. For vehicles with small roll inertias and roll accelerations

$$I_x \dot{p} \cong 0$$

Equation (18) then becomes

$$C_{\ell_\delta}(\delta) = - C_{\ell_p}\left(\frac{pd}{2V}\right)$$

or

$$p = - \frac{C_{\ell_\delta}(\delta)}{C_{\ell_p}\left(\frac{d}{2V}\right)} \tag{19}$$

The roll rates given by equation (19) are steady-state values ($\dot{p} = 0$) for any instant during flight.

Magnification Factor

Due to dynamic cross coupling between vehicle roll rate and pitch natural frequency, as previously discussed, the non-rolling trim incidence is magnified. The amount of magnification is expressed in the form of magnification factor f_m. Simplification of the vehicle equations of motion (refs. 17 and 18) indicates that the magnification factor depends primarily upon two parameters: The first is a damping function ξ which is the ratio of the non-rolling damping of the system to critical damping; the second is the ratio of roll rate to pitch frequency p/ω_n.

The magnification factor is expressed as

$$f_m = \frac{1}{\left(1 + \frac{p}{\omega_n}\right)\sqrt{(\xi)^2 + \left(1 - \frac{p}{\omega_n}\right)^2}} \tag{20}$$

where

$$\xi = -\frac{\left\{\frac{[M_{Y_q} + M_{Y_{\dot{\alpha}}} + (M_{Y_q})_j]}{I_y} + \left(\frac{-F_{N_\alpha}}{mV}\right)\right\}}{2\omega_n} \tag{21}$$

The simplified equations indicate the maximum magnification to occur at $\frac{p}{\omega_n} = 1$, or

$$f_m = \frac{1}{2\xi}$$

or

$$f_m = \frac{\omega_n}{-\frac{[M_{Y_q} + M_{Y_{\dot{\alpha}}} + (M_{Y_q})_j]}{I_y} + \left(\frac{F_{N_\alpha}}{mV}\right)} \tag{22}$$

where

$$\omega_n = \left(\frac{-M_{Y_\alpha}}{I_y}\right)^{1/2}$$

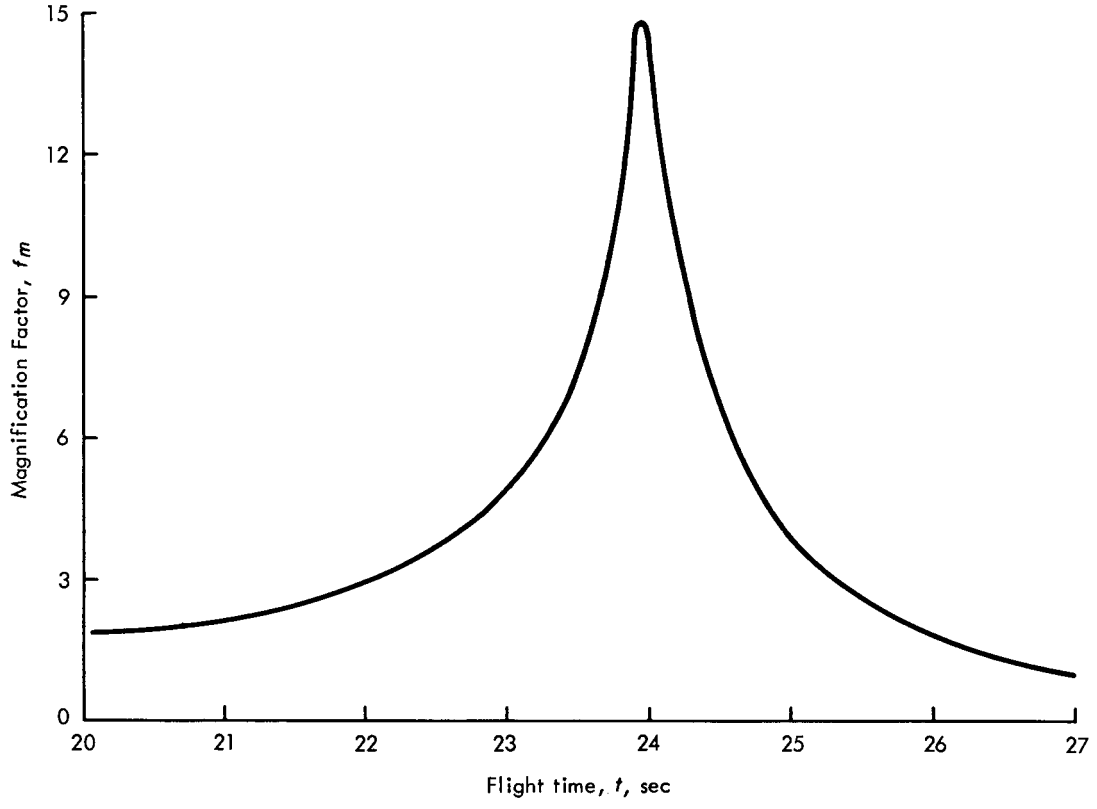

FIGURE 25. — *Magnification factor during resonance (based on maximum roll rate of 4 cps).*

The magnification factor in the region of resonance for the 4-cps maximum roll program is shown in figure 25. The 20-cps maximum roll program never approaches a resonance condition; hence no significant magnification will occur.

Non-Rolling Trim

It was stated previously that the incidence angle at any time is a result of the magnification of the non-rolling trim angle, or

$$\eta = \eta_{p=0}\,(f_m) \tag{23}$$

where

$$\eta = (\alpha^2 + \beta^2)^{1/2}$$

The non-rolling trim angle, $\eta_{p=0}$, is due purely to vehicle asymmetries. Because these asymmetries resulting from manufacture and assembly errors are difficult to predict accurately, they must be estimated. The asymmetries are assumed to be composed of aerodynamic, mass, and thrust misalinements which are noted as follows:

$(\delta_a)_f$ = fin misalinement
$(\delta_a)_n$ = nose misalinement
δ_F = thrust misalinement
D_m = mass unbalance

The non-rolling trim angle $\eta_{p=0}$ can be found by considering the above asymmetries as acting about the pitch axis only. These asymmetries, depending on how they are assumed, result in an overturning moment $M_{Y,A}$ about the pitch axis. Thus, for statically stable vehicles, the vehicle will assume a non-rolling trim angle, $\eta_{p=0}$ given by

$$M_{Y,A} = M_{Y_\alpha}(\eta_{p=0})$$

or

$$\eta_{p=0} = \frac{M_{Y,A}}{M_{Y_\alpha}} \tag{24}$$

Based on experimental measurements, with the mass unbalance contribution being neglected because of insignificant magnitude, the following asymmetries were considered to be both conservative and realistic:

$(\delta_a)_f = 0^0$ 06′ per fin
$(\delta_a)_n = 0^0$ 15′
$\delta_F = 0^0$ 15′

These estimated asymmetries could act in any plane; however, the estimation would be most conservative if the asymmetries were assumed to be all in one plane and acting in the same sense. Thus,

$$M_{Y,A} = \sum_n M_{Y,n}$$

where $\sum_n M_{Y,n}$ is the total moment about the vehicle center-of-gravity location of n component asymmetries.

The upper part of figure 26 shows the trim incidence during flight. The lower part of the same figure presents the resultant incidence angle due to magnification during flight.

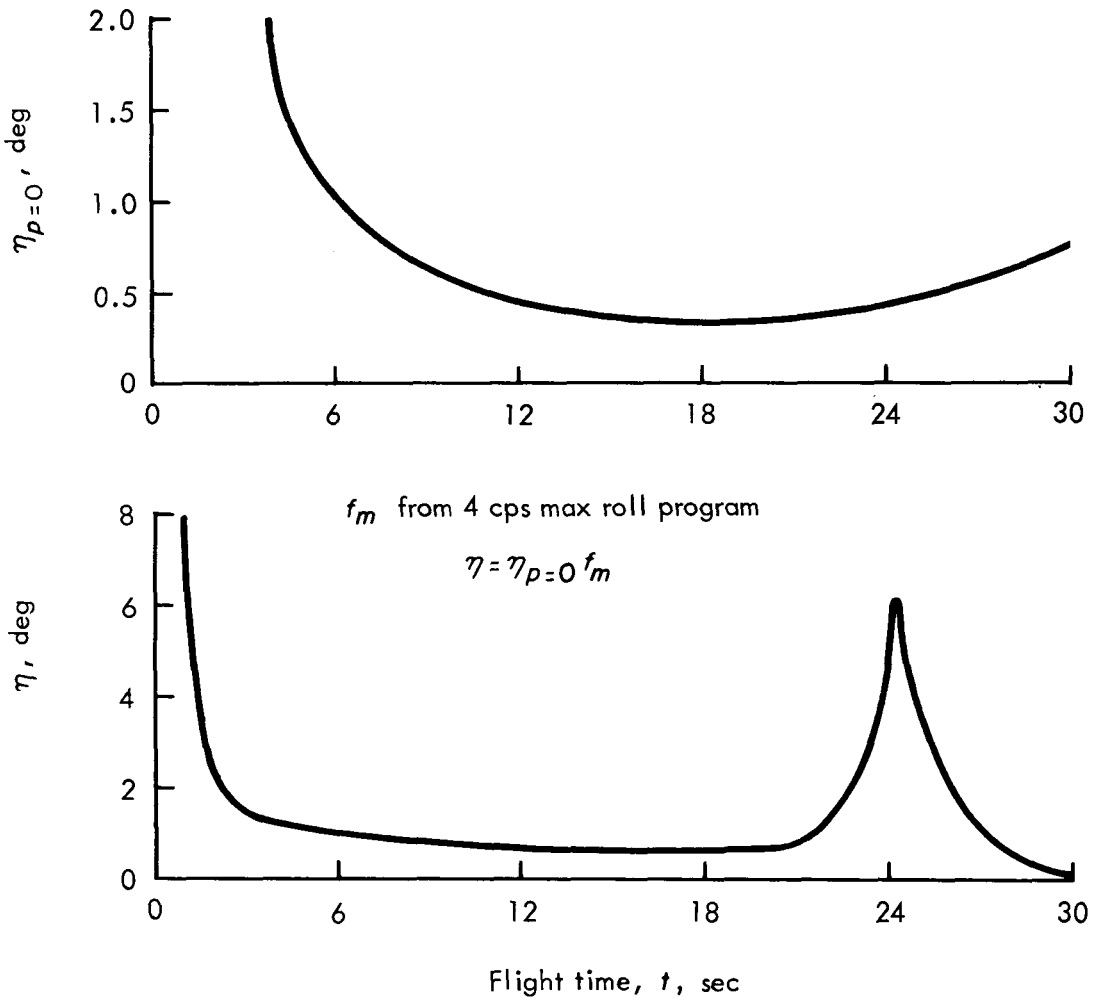

FIGURE 26. — *Nonrolling and rolling incidence.*

AERODYNAMIC LOADS

The air loads on the body and fins were determined from the lift characteristics of the various components associated with the total vehicle angle of attack. This total angle of attack is produced by wind shears and the amplified trim angle discussed previously.

Wind Angle of Attack

Using the procedure of reference 19, the wind angle of attack was determined by assuming a triangular wind shear which can reverse direction as the vehicle transverses its wave length. If the vehicle is statically stable with no angle of attack or angular rates, it obtains an angular rate equal to the shear gradient upon entering the gradient. The resulting response is sinusoidal, with the maximum amplitude occurring at ¼ wave length of vehicle motion after the initial entry. This maximum amplitude is determined by

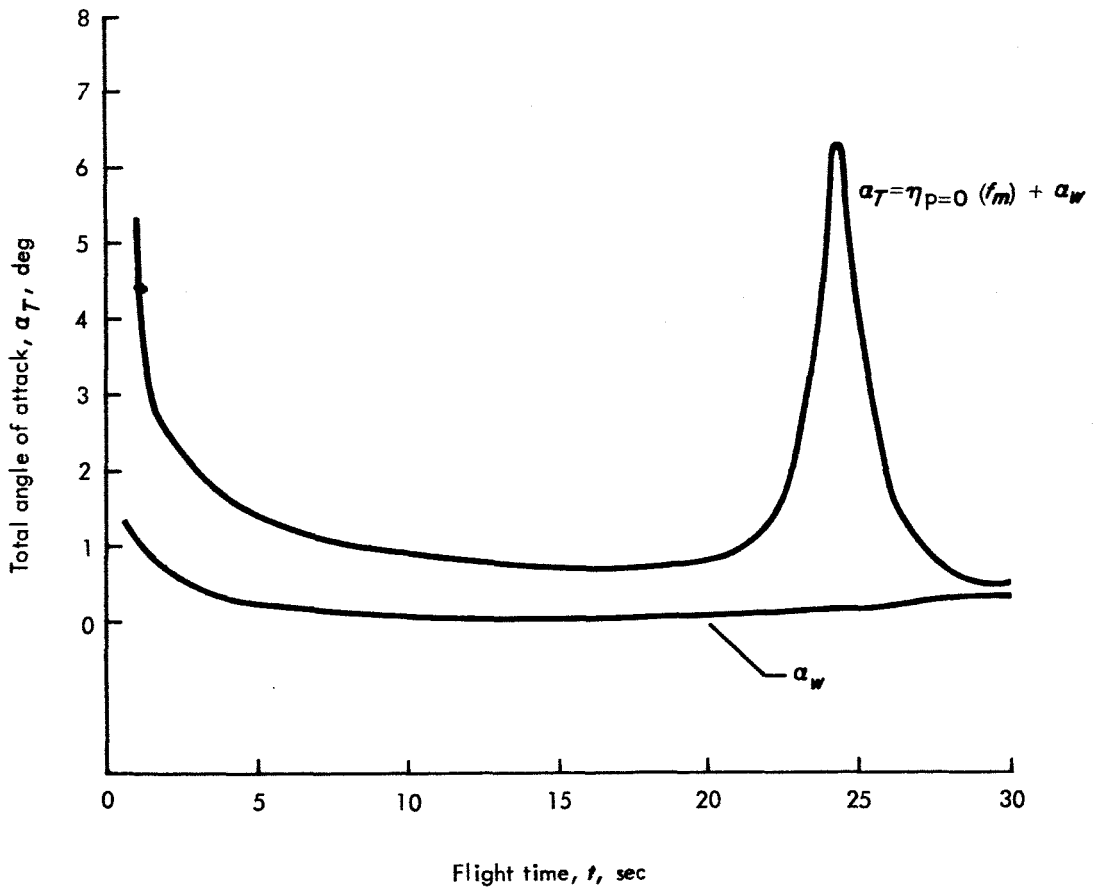

FIGURE 27. — *Total angle of attack.*

dividing the initial angular rate by the natural pitch frequency. If the gradient reverses at the most unfavorable time and persists, the wind angle of attack will overshoot by a factor of 3. Thus

$$\alpha_w = \frac{3\,(s_w)}{\omega_n} \tag{26}$$

where

$$s_w = \frac{\mathrm{d}V_w}{\mathrm{d}h}$$

Statistical wind distributions for Wallops Station during the summer months (ref. 2) indicated maximum wind shears (99.9-percent probability) on the order of

$$\frac{\mathrm{d}V_w}{\mathrm{d}h} = 0.03 \text{ per second.}$$

Total Angle of Attack

The total angle of attack is the sum of the wind angle of attack and the magnified non-rolling trim. The total angle of attack is plotted against flight time in figure 27 and is used in the following sections to determine the aerodynamic loads.

Nose/Body Air Loads

Concentrated nose/body air loading was determined by using the body lift characteristics discussed previously in conjunction with the total angle of attack. Thus

$$F_{N_{nose}} = \left(C_{N_\alpha}\right)_{body/nose} \alpha_T \left(\tfrac{1}{2}\rho V^2\right) S_R \tag{27}$$

The nose air loads are plotted against flight time in figure 28.

Fin Air Loads

The concentrated fin panel air load was determined as before by

$$F_{N_{fin}} = \tfrac{1}{2}\left(C_{N_\alpha}\right)_{fin} \alpha_T \left(\tfrac{1}{2}\rho V^2\right) S_R$$

The fin air load is plotted against flight time in figure 29.

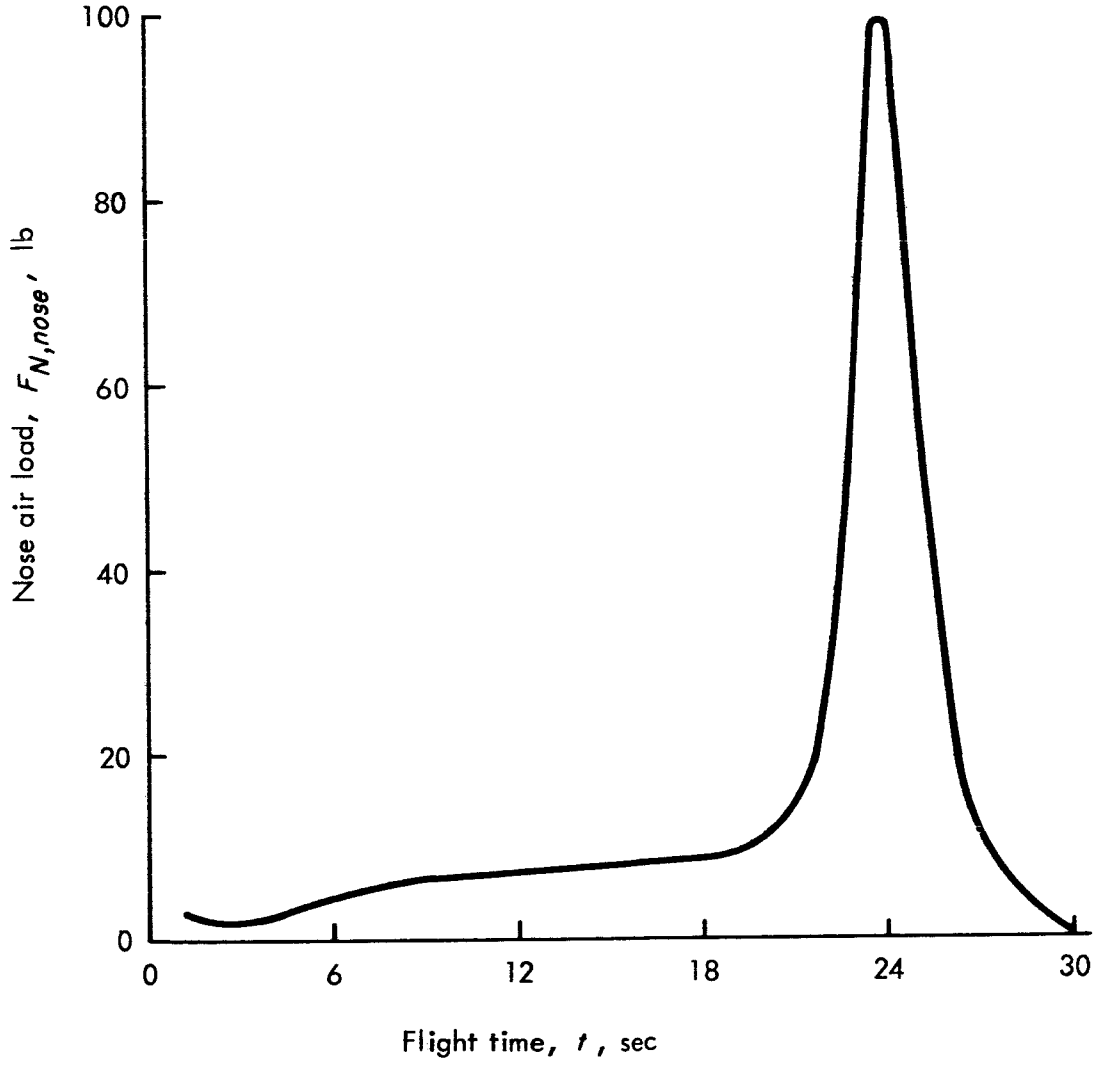

FIGURE 28. — *Nose air loads.*

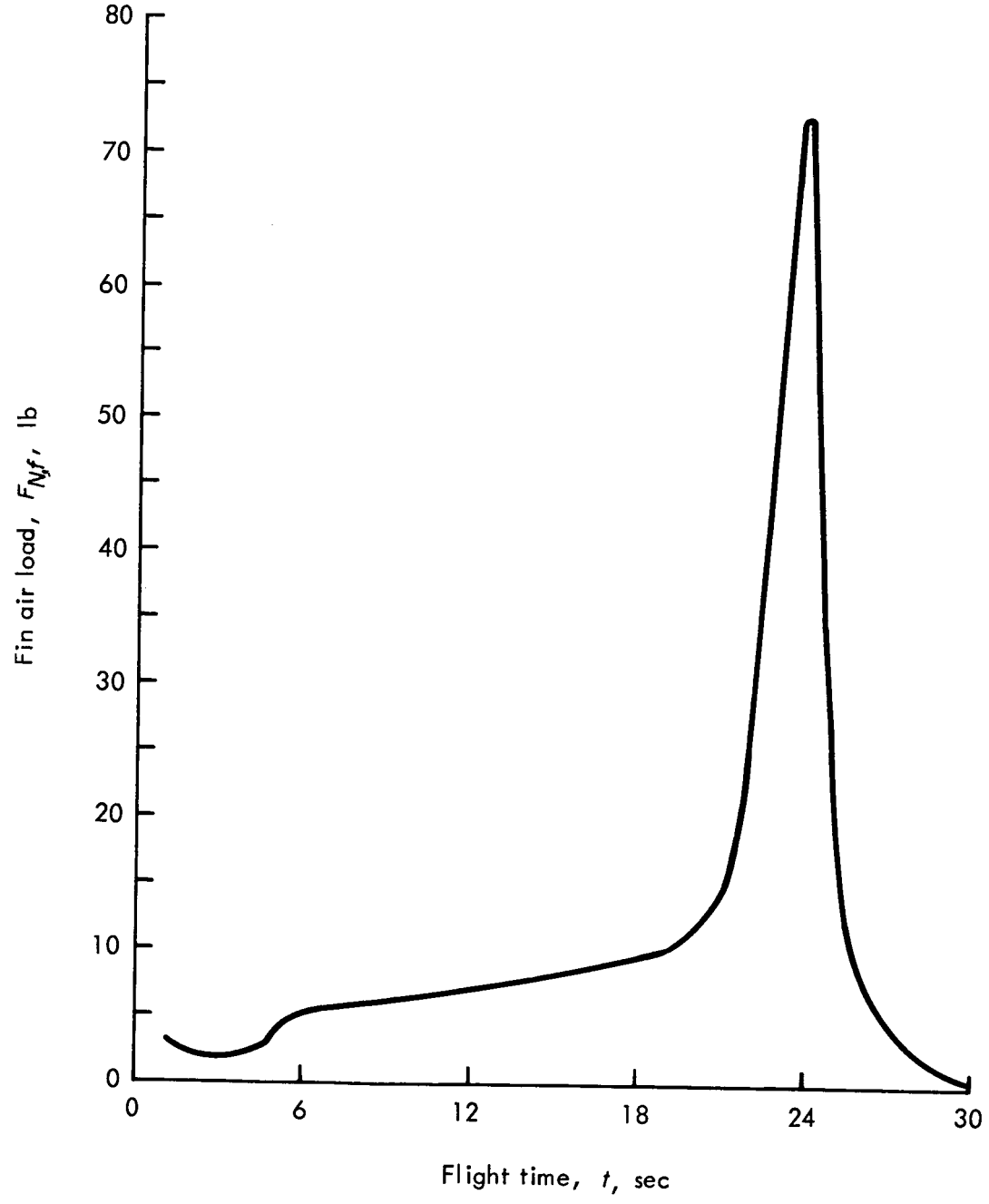

FIGURE 29. — *Fin air loads per panel.*

CHAPTER 4

Payload and Recovery Systems Design

MECHANICAL CONFIGURATION

The general mechanical requirements for the Bio-Space payload were to mate the payload and recovery/adapter assembly to the Arcas launch vehicle and to house the animal specimen with the associated supporting structure and equipment in such a manner as to provide an adequate environment for all phases of the flight trajectory and sea recovery.

The following predicted performance parameters were considered pertinent to animal tolerances and the resulting payload design criteria:

(1) Shock accelerations in the longitudinal axis at lift-off and payload separation of 50g

(2) Sustained longitudinal accelerations with a maximum of approximately 6g

(3) Angular accelerations resulting from a maximum angular velocity of 20 cps

(4) Aerodynamic heating and parachute descent cooling

(5) Vibration and noise

(6) Parachute opening shock deceleration of 50g

(7) Water impact deceleration

An additional design criterion imposed on the payload was that a favorable ratio of total external volume to total weight be maintained to insure flotation without the aid of other flotation devices.

In conformance with these design requirements, the payload assembly shown in figure 2 was designed and fabricated. The payload assembly primarily consists of a fiber-glass nose cone, telemetry instrumentation with associated supporting structure, and a life-support capsule. The life-support capsule was placed close to the payload center of gravity to minimize ac-

celeration forces due to tumbling that might be encountered during payload separation. The animal couch was placed in the life-support capsule centered on the roll axis to minimize the effects of normal and tangential accelerations due to high roll rates. External access to the nose cone is provided only at the base to minimize potential flotation and life-support capsule sealing problems.

The selection of an adequate environment for the life-support capsule was based on bench-test performance of two different designs: In one design, the atmosphere was supplied by a high-pressure oxygen storage bottle and regulator. The regulator was set to provide a chamber pressure of 5 psia. The characteristics of the regulator and bottle are as follows:

Volume of gas, cu in.	9
Supply pressure, psig	500
Outlet pressure, psia	5 ± 0.2
Flow rate, liters/hr at standard temperature and pressure	0 to 0.5
Gas	Oxygen
Acceleration limit, g	50
Ambient pressure, psia	0 to 14.7
Weight, oz	16
Size (cylindrical shape):	
Diameter, in.	2
Length, in.	8

In the other design, the animal was sealed in the life-support capsule with a suitable atmosphere for a sufficient time period (including preparation, launch, and recovery), and then the animal was removed before the atmosphere deteriorated. Both designs considered used anhydrous lithium hydroxide as a CO_2 absorbent.

Each design was fabricated and bench tested with an animal; both methods proved satisfactory. Since the project objectives did not impose special environmental requirements, the latter design was selected because of its simplicity and weight advantage.

The following description of the payload and components is given to augment the section view of the payload presented in figure 2. The payload can be generally subdivided into three groups: the nose cone with associated

load-transmission bumper rings and the aft payload attachment ring, the data transmission housing assembly, and the life-support capsule assembly.

The nose cone was fabricated from a number 181 fiber-glass cloth bonded with an Epon 828 polyester resin and machined to a uniform thickness of 0.10 inch. The load-transmission attachments, bumper rings, were fabricated from the same fiber-glass resin compound as the nose cone and machined so that the outer surfaces exactly mated with the inner surface of the nose cone, thereby assuring a uniform load transmission to the nose cone. The rings were then bonded to the inner surface of the nose cone with a high-strength plastic cement.

The aft payload attachment ring was fabricated from 6061-T6 aluminum and machined to assure the same nicety of fit as the bumper rings. The inner circumference was threaded to provide a positive attachment with a high degree of fixity for the payload within the nose cone. The ring was then bonded to the extreme aft inner circumference of the nose cone.

The data transmission housing was assembled by stacking the individual system components in the following order: aft end-seal, power supply, separator, power supply, separator, terminal section, separator, transmitter, separator, terminal section, and finally a life-support end plug. The assembled system was then firmly tied together and properly aligned by means of four steel rods extending through the assembly from the aft end seal to the life-support end plug.

The aft-end seal was machined from 6061-T6 aluminum and threaded to screw into the end seal affixed to the nose cone. In order to assure no pressure leakage, this ring was fitted with three rubber "O" rings arranged in series. The forward side of the aft-end seal contained four 1/16-inch holes to permit attachment of the steel rods. The underside of the aft-end seal was machined to accept the parachute forward closure from the recovery system, thereby integrating the payload and recovery system.

The aluminum housing cylinders were machined from 6061-T6 aluminum to an outside diameter of 4.28 inches and a thickness of 1/16 inch. The lengths of the cylinders varied from 2 inches for the power supply sections, ½ inch for the terminal sections, to 4½ inches for the transmitter section.

The batteries in both power-supply sections were positioned and secured by foaming in place. The transmitter components were secured by the steel rods.

The separators were fabricated by sandwiching a 0.10-inch cork insert between two 0.10-inch bakelite panels. They were then drilled to permit passage of the steel rods through them. These separators attenuated the anticipated high longitudinal impulse loads and also transferred the component loads to the bumper rings and nose cone shell.

The life-support end plug was machined from 6061-T6 aluminum, threaded on the forward side to receive the aft end of the life-support capsule, and flanged on the bottom to enclose the forward terminal section. The flanged portion of this end plug was drilled on the same pattern as the aft-end seal to provide passage for the steel rods. The system was then properly aligned and secured by means of self-locking nuts screwed against the flange of the life-support end plug.

The life-support capsule was fabricated by simply threading a section of 2¾-inch outside diameter by 1/16-inch-thick fiber-glass tubing at both ends. The aft end of the tubing screwed onto the aforementioned life-support end plug to which the animal couch was also attached. The life-support top plug provides the seal on the forward end of the capsule.

The animal couch was constructed of the same fiber-glass components as the nose cone. Several holes were drilled through the couch to afford as much ventilation as possible to the animal. The couch was attached to the life-support end plug by a bracket and aligned within the fiber-glass life-support enclosure with a bakelite plastic disc of the same diameter as the inside of the capsule.

The life-support top plug was machined from 6061-T6 aluminum and threaded to screw into the life support enclosure. A proper seal was insured by the use of an O-ring. The forward plug was tapped to accommodate two pressure valves, one feed and one vent, and a pressure transducer.

AERODYNAMIC HEATING AND COOLING

Aerodynamic heating effects were investigated at two points on the nose cone, one at the stagnation point and the other at a point 12 inches aft of the

nose tip. Temperature time histories for the payload were calculated by computer programs for the stagnation temperatures and internal temperature profile using modified heat-balance equations. The general method of heat calculations for the payload's internal temperature profile assumed that the body can be broken into a number of individual blocks so that a temperature history can be determined for each block over a specified interval of time using specified time increments. Inputs provided for the programs were trajectory parameters, consisting of free-stream values of velocity, Mach number, Reynolds number, temperature, density and time, payload configurational geometry, and material properties including conductivity, density, specific heat, and emissivity. A temperature-time history from launch to payload separation at apogee is presented in figure 30 for the nominal trajectory.

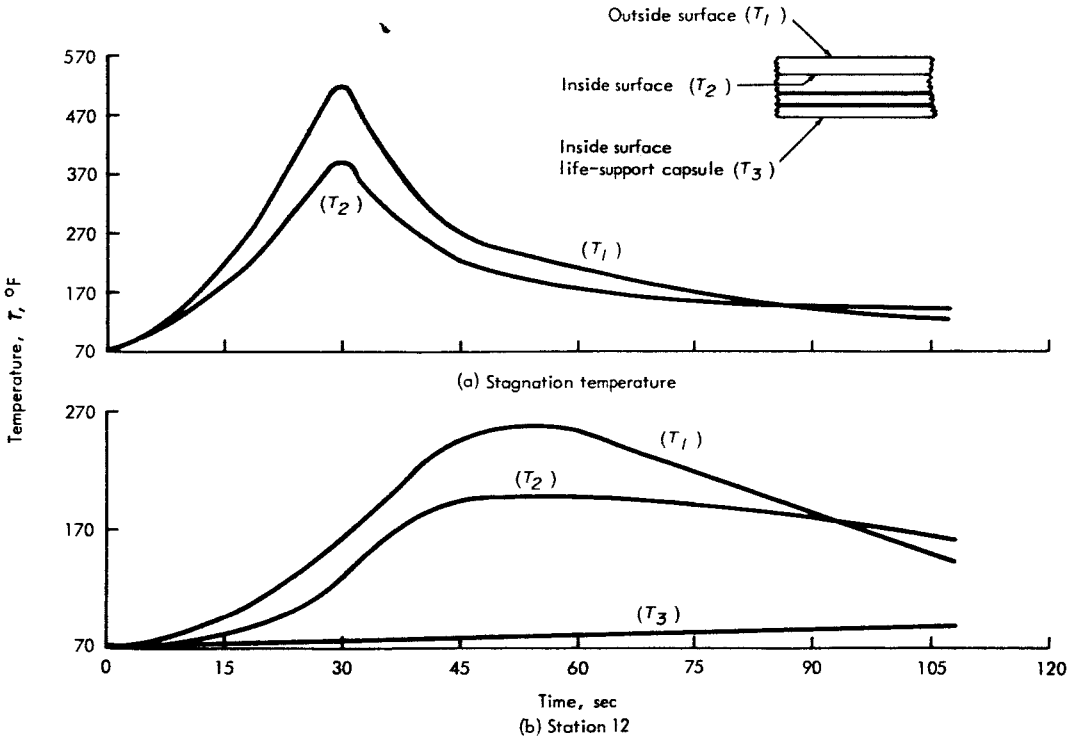

FIGURE 30. — *Heating of nose cone at stations 0 and 12.*

The cooling during parachute descent was determined using initial conditions at payload separation as initial inputs. Results are given in figure 31.

The maximum temperature variation predicted for the inside wall of the life-support capsule is shown in figure 31. The maximum temperature expected was 120° F at 2 minutes after separation, and the minimum expected was 40° F at 18 minutes after separation.

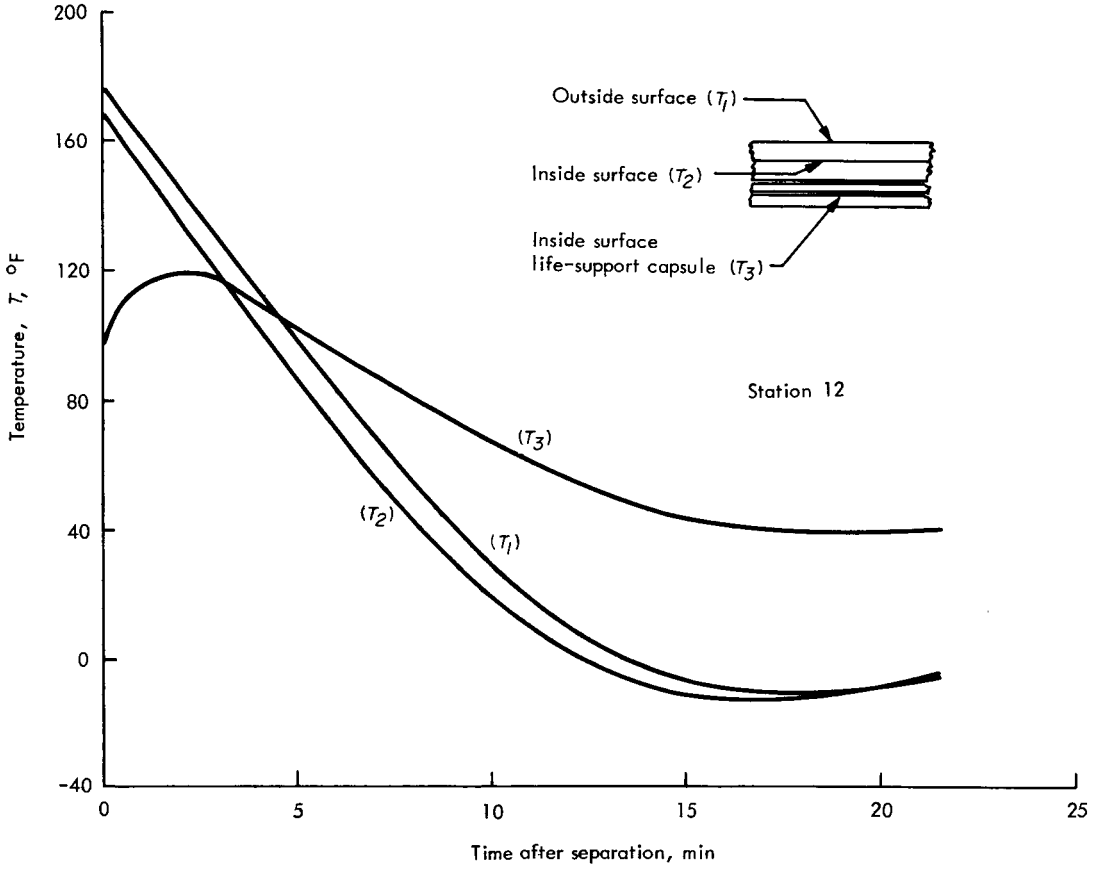

FIGURE 31. — *Cooling during parachute descent (temperature taken at station 12).*

RECOVERY SYSTEMS

Retrieval of the Bio-Space payload with its live specimen aboard was a primary mission objective. To accomplish this objective, the design criteria necessarily included high reliability in systems with small weight and volume allocations.

The recovery systems and aids used in the Bio-Space configuration are parachute and deployment system, flotation, and location aids.

Parachute and Deployment System

The primary parachute design considerations were:

(1) Parachute geometry, descent rate, and resulting total descent time selected to accommodate the following:

(a) Animal's tolerance to cooling influence of upper atmosphere

(b) Terminal velocity at water impact and resulting impact loads

(c) Dispersion of payload due to wind drift

(2) Adequate stability to minimize oscillatory motions during descent and resulting angle of attack at water entry.

(3) Structural integrity to withstand dynamic pressures at deployment and resulting deceleration loads.

(4) Canopy fabricated from a material with air permeability characteristics suitable for high altitude deployment (approximately 115 000 feet) and metalized to facilitate radar tracking as a prime location aid.

To meet the requirements and considerations, a parachute was designed with the following characteristics:

Type	Hemispherical
Material	Metalized silk
Weight (including payload attachment), lb	1.1
Flying diameter, ft	3.7
Drag area (C_DS), ft^2	10.3
Packing volume, in.^{3}	68

The deployment system primarily consists of a static line, break line, canopy crown bridle, deployment bag, reefer line, and reefer-line cutters. Because of the ballistic-factor characteristics of the payload and expended launch vehicle, a nominal 6-second delay was incorporated into the parachute deployment sequence to prevent a potential collision. The time delay is provided by two subminiature reefer-line cutters attached to the deployment bag. The following is the deployment sequence of events:

Nominal time from lift-off, sec	*Event description*
108	Payload separates from expended launch vehicle with a $\Delta V \approx 50$ ft/sec and a peak acceleration of approximately 40g.
108.3	Static line becomes taut and pulls actuation pins in both reefer-line cutters simultaneously.
108.3 +	Static line again becomes taut and severs break line connected to the parachute canopy's crown bridle. Payload and launch vehicle are now physically disconnected, and reefed uninflated canopy serves as a stabilizing influence on the aerodynamically unstable payload.
114.3	Parachute is inflated by actuation of either of the two reefer-line cutters.

For the nominal trajectory case with parachute deployment at 114.3 seconds after lift-off, a dynamic pressure of 15 lb/ft^2 is predicted, and a shock opening load of 232 pounds is expected.

Performance for the parachute attached to the payload is discussed in the section entitled "Recovery System Performance" and shown in figures 5, 10, and 11. The descending parachute and payload are shown in figure 32.

Flotation

Flotation is provided by a favorable ratio of total external volume to total payload weight. Internal volume seal is afforded by O-rings positioned in series at the aft end of the payload. The distributed mass of the payload and external nose-cone configuration geometry permits a slight nose tip-up buoyant attitude. This flotation attitude exposes the dye marker located in the aft end to sea water and also provides sufficient nose-cone planform area above water level for an effective search target.

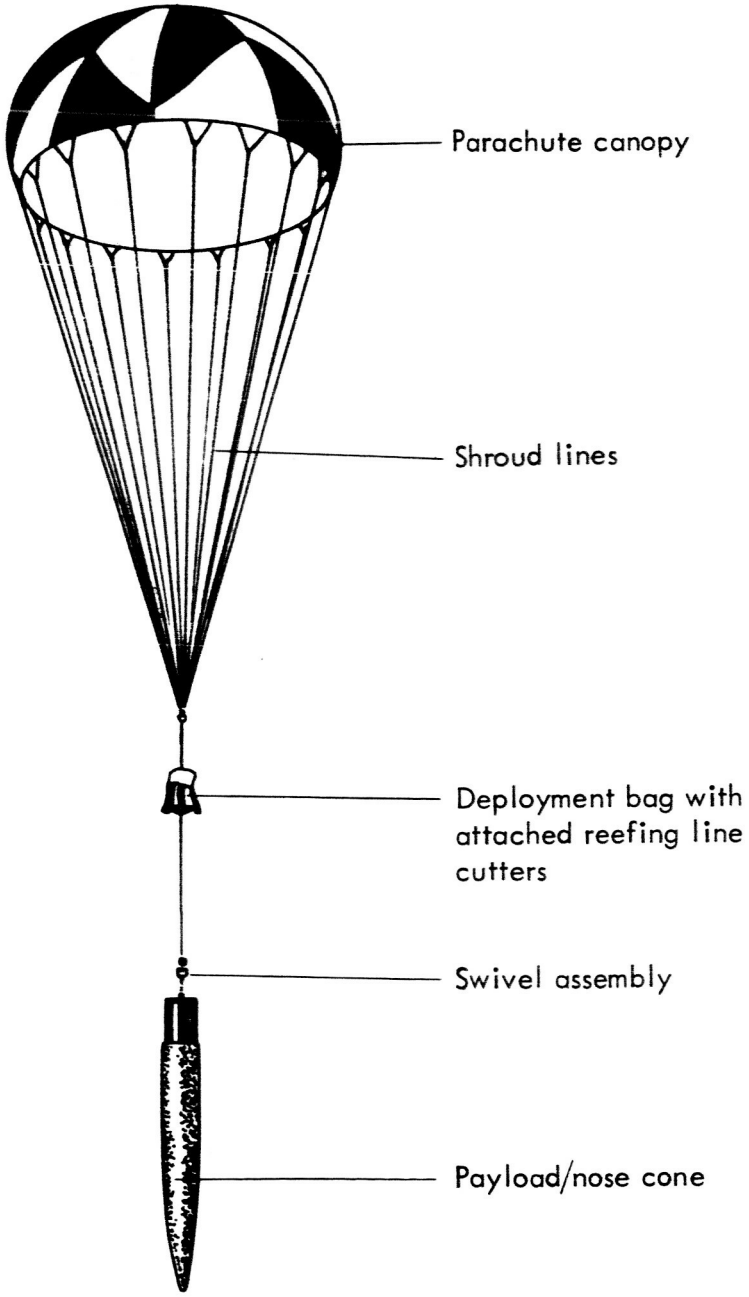

FIGURE 32. — *Bio-space recovery package.*

Location Aids

Passive location aids are employed and consist of a radar reflective parachute, dye marker, and conspicuously painted (fluorescent orange) nose cone. Tracking radars locate the impact point of the payload and vector the recovery vehicles to the location. The dye marker and painted nose cone become effective aids once the vectored search craft are in the payload's vicinity and are executing visual surveillance. The fluorescein dye marker is effective for approximately 4 hours after impact.

TELEMETRY SYSTEM

Selection of the components for the telemetry system must necessarily reflect the requirements for measuring the frequency response and accuracy of the data. Consideration was given to the use of a time-sharing technique since this approach is extremely attractive for measuring slowly varying parameters. However, since only four channels of data were being measured, two of which required continuous coverage, it was decided that one subcarrier oscillator for each data channel would better suit all requirements for the system.

The following general guidelines were used in the selection of the system:

(1) The system must consist of components conforming to IRIG telemetry standards if possible.

(2) An FM/FM system will be used.

(3) Components must meet or exceed the expected environmental and performance requirements.

(4) Subassemblies must be interchangeable on a plug-in basis.

(5) The system power drain must be minimized.

(6) The system must conform to size and configuration dictated by payload requirements.

(7) The system weight must be minimized.

(8) Components with space-flight history are desirable.

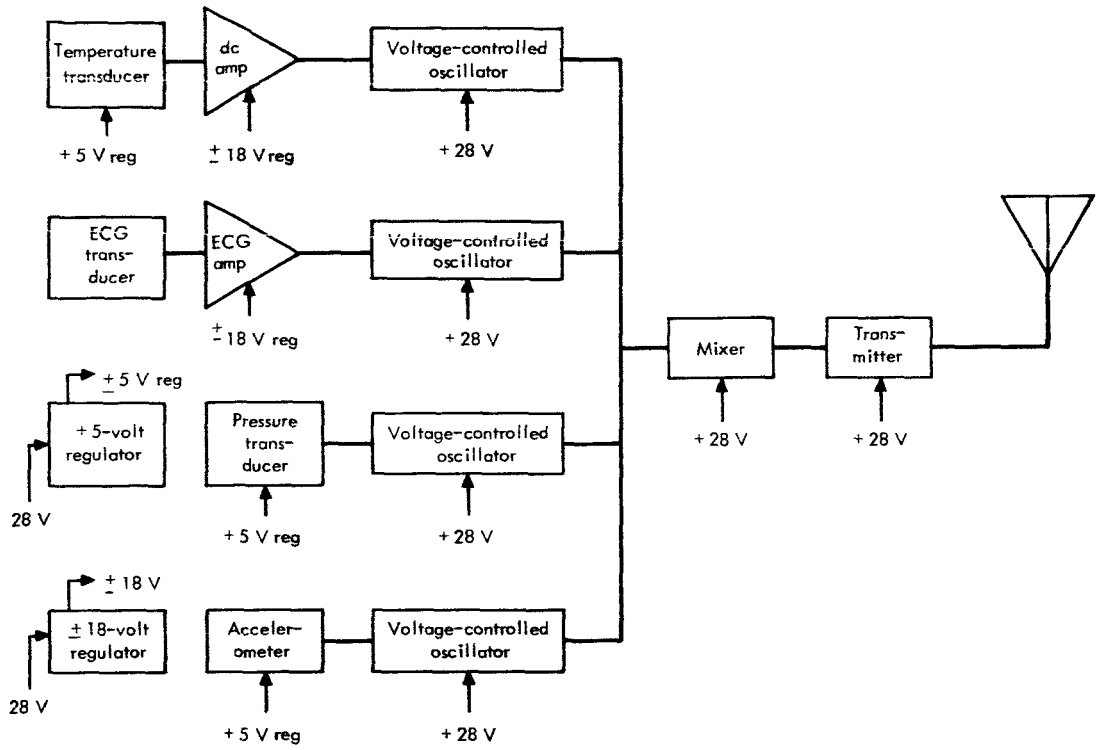

FIGURE 33. — *Telemetry system schematic.*

A schematic for the complete telemetry system is shown in figure 33.

System Components

Antenna—The antenna design was based primarily upon three considerations:

(1) Because of the nature of the launching system and the need for a sealed nose cone, the antenna should be internal to the nose cone.

(2) To provide spin rate, the antenna radiation pattern as seen by the receiving station must have nulls.

(3) The radiation pattern should be maximized consistent with the other requirements.

The antenna system consists of a double-slotted cylinder with one driven and one parasitic element. The radiation requirement is satisfied by this antenna since there are two significant nulls in the pattern as seen from the side of the payload. Polarization is perpendicular to the length of the slot.

Radiation patterns were taken by holding the receiving antenna in a fixed position and rotating the payload. This method avoided errors which may have occurred if the receiving antenna had been rotated and its characteristic changed.

Polar radiation patterns were taken with the payload in the horizontal and vertical positions only. No attempt was made to establish a spherical pattern other than by interpolation.

Transmitter—The transmitter is a phase-modulated crystal-stabilized type operating at a frequency of 240.2 megacycles. The power output when provided with an optimum load is 250 milliwatts.

+5-volt dc Regulator—A +5-volt voltage regulator was used to supply the voltage necessary for expectation of the Wheatstone bridge circuit and the potentiometer circuits of the transducers.

± 18-volt dc Regulator—A ± 18-volt dc supply was used to provide voltage for operation of the transducer amplifiers.

Power Source—The power necessary for the instrumentation was supplied by nineteen 1.5-volt cells connected in series to provide a nominal 28-volt source. The capacity of the silver zinc cells is 1 ampere-hour at 1.5 volts.

For all prelaunch testing, power was supplied by an external supply.

Voltage Controlled Oscillators—Four voltage-sensing subcarrier oscillators were used in each payload. IRIG channels 13, 5, 6, and 7 were used for ECG, skin temperature, pressure, and longitudinal acceleration, respectively.

Electrocardiogram Amplifier—The primary features of the ECG amplifier are small size, light weight, low noise, high stability, and high common-mode rejection. The amplifier was designed especially for use in physiological instrumentation systems. The ECG amplifier has the following characteristics:

Maximum gain	8000
Minimum gain	220
Maximum undistorted subject, V (peak-to-peak)	6
Wide-band noise (0.15 cps to 30 kcps), μV rms	< 2
Narrow-band noise (0.15 cps to 100 cps), μV rms	< 1
Low frequency, cps	0.15
High frequency, kcps	35
Command mode rejection, dB	> 90

A low-level amplifier was used to condition the signal output of the Wheatstone bridge used for the temperature measurement to a level suitable for application to the VCO. This amplifier produces a 0- to 5-volt signal output with a ± 10-millivolt input.

The primary features of the amplifier are low noise, high gain, and high common-mode rejection.

Transducers

Transducers are used in the measurement of temperature, ECG, acceleration, and pressure. A wiring diagram for the transducers is given in figure 34.

Temperature Measurement—In the temperature measuring systems the thermistors were used in a Wheatstone bridge circuit to provide maximum sensitivity (percent output change versus temperature) and linearity. Since the resistance of the thermistors was high compared with lead resistance, no correction for lead length was necessary.

It was necessary to limit the voltage applied to the thermistor so that the small current flow would not produce enough heat in the thermistor to cause incorrect readings as a result of self-heating. The voltage was limited by careful selection of bridge circuit resistances and by using a voltage dividing network at the input terminals of the bridge. Resistances were chosen so that the bridge could be adjusted for zero output at the center of the temperature range, and plus or minus 10 millivolts at the high and low temperature points, respectively.

An amplifier was used at the output terminals of the bridge to condition the signal before insertion into the voltage controlled oscillator.

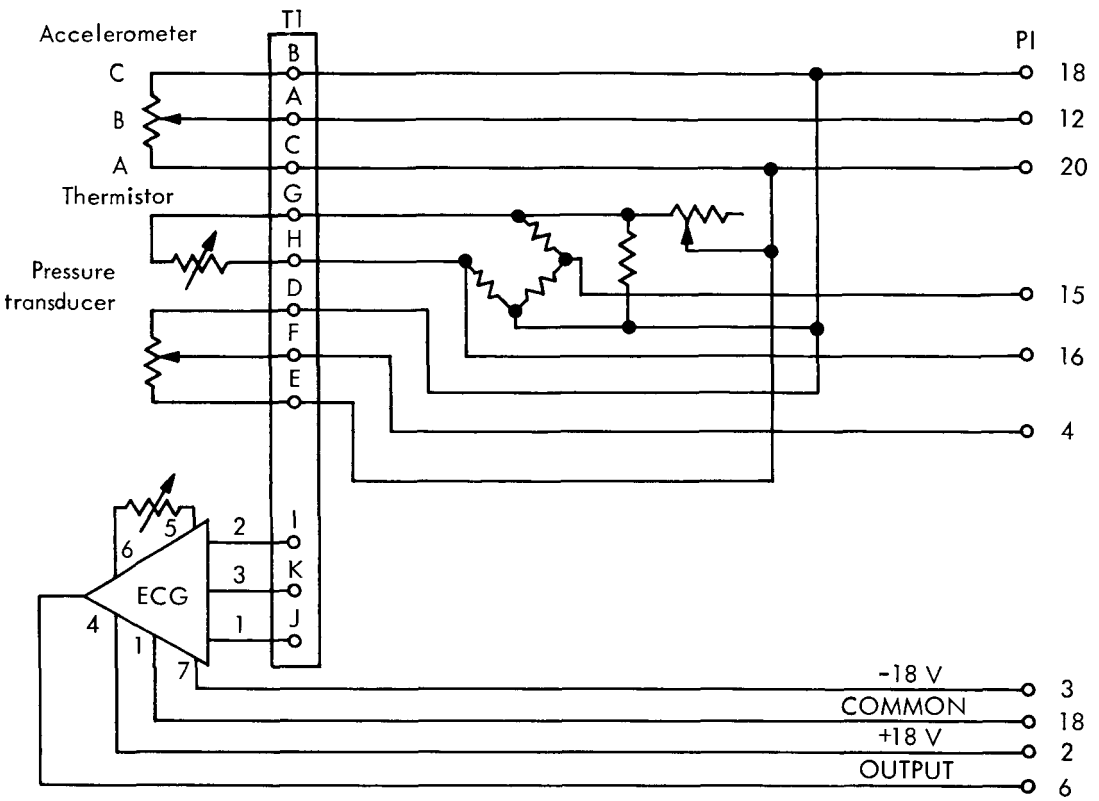

FIGURE 34. — *Transducer wiring diagram.*

Small glass bead thermistors mounted on an anodized aluminum disk were used. The dissipation constant and time constants are 0.7 mW/°C and 2 seconds, respectively. The thermistor bead diameter is approximately 0.043 inch.

Electrocardiogram—ECG was taken using several types of surface and implanted electrodes. It was determined that ECG could be optimized from the standpoint of minimum noise and minimum base line shift by using small circular disks implanted under the skin.

The ECG signal was conditioned by a small variable gain amplifier before insertion into the voltage controlled oscillator.

Accelerometer—The accelerometer used provides a voltage-ratio output

that varies in direct proportion to the g-values of acceleration in two linear directions. The output is obtained by using a spring supported mass to actuate the noble metal brush of a precision wire-wound potentiometer. The accelerometer is fluid damped.

The specifications are as follows:

Range, g	± 50
Natural frequency, cps	100 (± 15%)
Temperature environment, °C.	— 18 to + 71
Vibration	Mil–E–5272C, para. 4.7.1
Maximum weight, oz	2.25
Potentiometer resistance, ohms	5000
Size:	
Height, in.	0.81
Width, in.	0.83
Length, in.	1.48

Pressure Transducer—The pressure transducer used is an accurate, hermetically sealed, potentiometric-output, capsule-type instrument. The precision-wound potentiometer is made of a noble metal.

The specifications are as follows:

Pressure range, psia	0 to 25
Potentiometer resistance range, ohms	5000
Resolution, percent	0.4
Size:	
Diameter, in.	1
Height, in.	1
Maximum weight, oz	3
Linearity, percent	1.0
Repeatability, percent	0.40
Hysteresis, percent	0.80
Friction, percent	0.80
Temperature error (−65° F to + 200° F), percent	1.0

WATER IMPACT

The deceleration of the Bio-Space payload at water impact was investigated using the basic theory for impact loading developed by T. vonKarman. The velocity as a function of time for the virtual mass impact theory is given by:

$$V_t = \frac{WV_0}{W + m_v g}$$

where

W	payload weight
V_0	payload/parachute terminal velocity at initial water impact
m_v	virtual mass
g	acceleration of gravity

The virtual mass for the Bio-Space tangent ogive nose cone was assumed to be (ref. 20):

$$m_v = (0.64)\ (2/3)\ \rho r^3$$

where

r	radius of instantaneous cross section
ρ	density of water

A velocity time history and resulting deceleration for the Bio-Space payload was computed using as initial conditions a terminal velocity of 38 ft/sec and a total weight for the payload and parachutes at water entry of 14.4 pounds. The maximum deceleration computed was 1.4g which occurred after the nose tip of the tangent ogive nose cone had penetrated the water for approximately 12 inches. Experimental data from helicopter drop tests agreed well with the analytical predictions.

PHYSICAL PROPERTIES

A flight time history for the complete Bio-Space launch configuration including weight, center of gravity, pitch moment of inertia, and roll moment

of inertia are presented in figure 35. A tabulation of physical properties for the components, payload, recovery/adapter combination, and Arcas launch vehicle is also shown in figure 35.

All physical properties presented in this section are measured values from actual flight hardware items. A bifilar torsion pendulum was used to measure pitch and roll moments of inertia.

Component	W, lb	x_{cg}, in.	I_y, slug-ft^2	I_x, slug-ft^2
Payload	13.28	27.50	0.270	0.0082
Adapter assembly	2.60	41.52	.097	.0014
Launch vehicle loaded	66.00	74.30	4.374	.0433
Launch vehicle empty	24.00	76.40	2.508	.0260

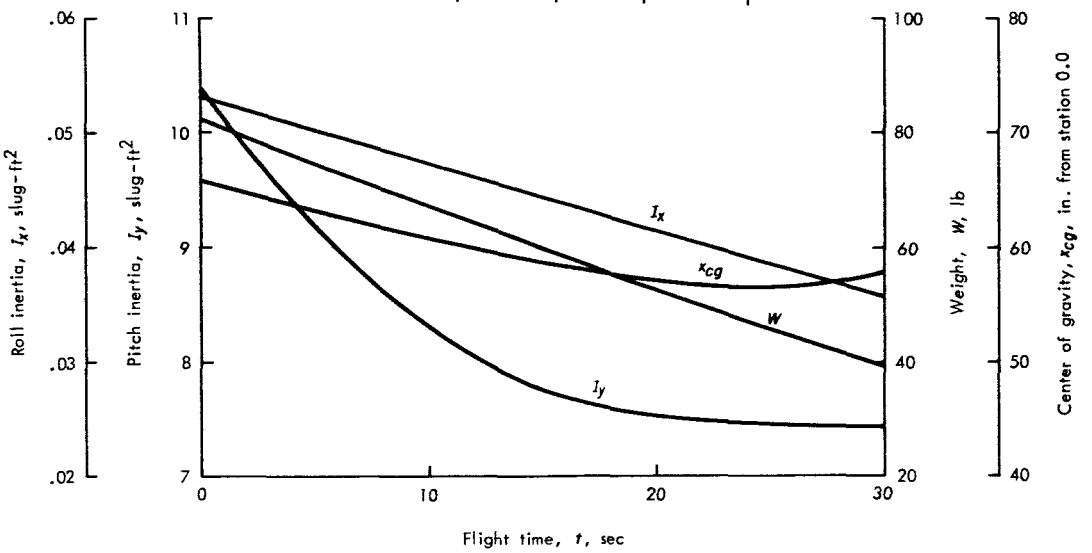

FIGURE 35. — *Physical properties.*

STRUCTURAL FREQUENCY

The three points in the rocket's flight trajectory selected for a fundamental transverse structural frequency computation were lift-off, time of maximum aerodynamic natural frequency at 19.2 seconds, and rocket burnout.

The Rayleigh method was used for the structural frequency computation. This method uses the static deflection curve as the mode shape of vibration and the frequency is determined when the maximum kinetic and potential energies of the assigned mode shape are equated. For an assumed static deflection curve for the Bio-Space configuration, the fundamental transverse structural frequency is given by

$$\omega_s^2 = \frac{\pi^4 g \int_0^{\ell} EI \sin^2 \frac{\pi x}{\ell} \, dx}{\ell^4 \int_0^{\ell} W_x \left(\frac{1}{2} - \sin \frac{\pi x}{\ell} \right)^2 dx}$$

where

E	modulus of elasticity, lb/in.^{2}
I	transverse moment of intertia, in.^{4}
ℓ	vehicle length, inches
W_x	weight distribution, lb/in.
g	acceleration of gravity, in./sec^2
ω_s	structural frequency, cps

As shown in the above equation the vehicle length, weight distribution, and flexural rigidity (EL) are the parameters employed in the structural frequency determination. Due to the difficulty encountered in attempting to express the weight and EI distributions as explicit functions of length, a numerical integration is performed over the total vehicle length with the weight and EI approximated by step distributions. The weight and flexural-rigidity distribution for the Bio-Space launch configuration are given in figure 36. The weight distribution shown is for the loaded launch-vehicle configuration, and the EI distribution presented is assumed constant for the complete flight profile.

Fundamental structural frequency as a function of rocket burning time is shown in figure 37. It was concluded from the results of this rigid body

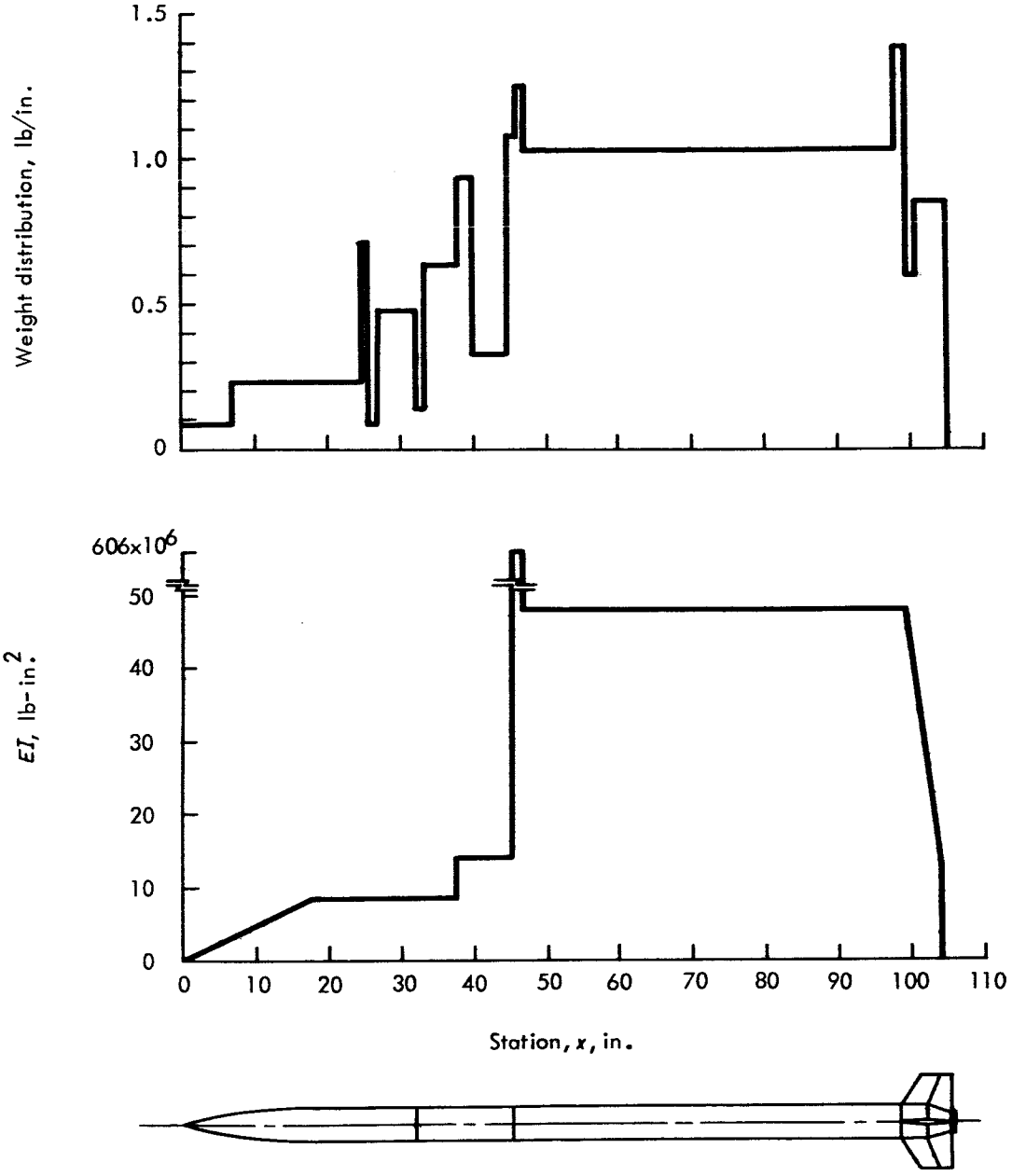

FIGURE 36. — *Structural properties.*

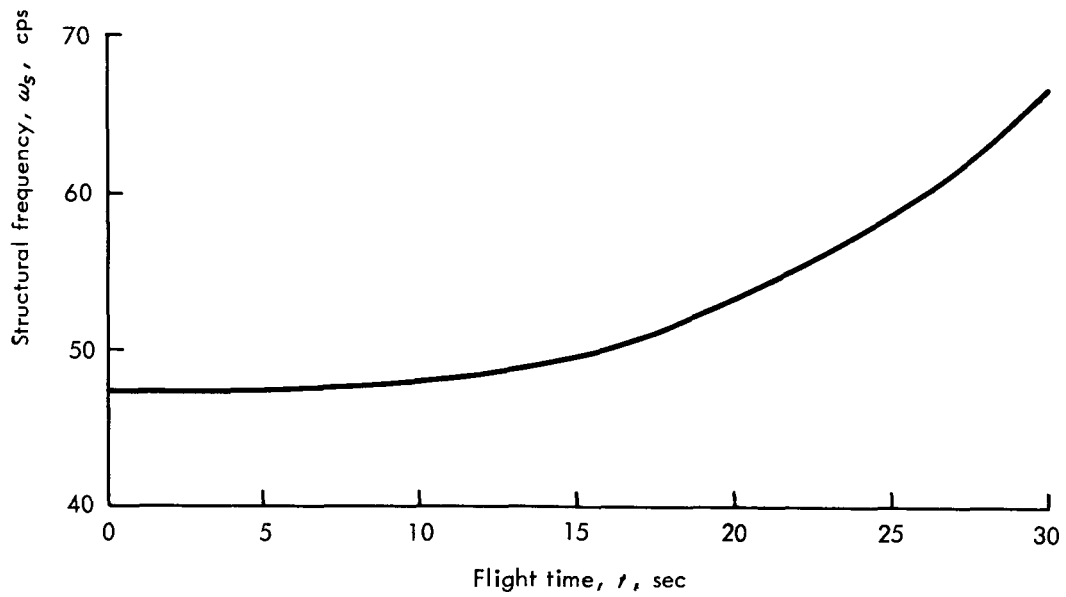

FIGURE 37. — *Fundamental structural frequency.*

analysis that the roll rates experienced by the subject vehicle were adequately removed from the frequency ranges that would produce significant resonant responses with the fundamental transverse body bending mode.

STRUCTURAL INTEGRITY

Structural loading on the Bio-Space launch configuration was investigated at the point in the trajectory where the product of the dynamic pressure and the vehicle's angle of attack was maximized. The flight time for maximum structural loading was at pitch-roll resonance ($t = 24$ sec) with a magnified angle of attack of 6.28° and a dynamic pressure of 2400 lb/ft^2.

Considerations of transverse loadings and probable vehicle structure indicate that payload and fin environment are the questionable items to be investigated on the Bio-Space configuration.

The principal transverse force on the nose cone is the aerodynamic lift force which is considered to be concentrated at the center of pressure of the

body/nose and boattail configuration. (See fig. 28.) However, the transverse load factor for this principal aerodynamic force is only slightly higher than the inertia load factor induced by rotation and translation. Attention was focused on the structural integrity of the friction-fit sleeve joint that mates the payload and the recovery/adapter assembly. Using the above mentioned applicable load factors acting on the nose cone, a resulting bending moment of approximately 2500 in-lb and a shear force of 80 pounds were calculated acting about the aft end of the payload (body station 39.3). The allowable tensile and shearing stresses for the fiber-glass nose cone are sufficiently high to preclude an initial failure in the engagement portion of the nose-cone shell. The initial structural failure mode for the joint was determined experimentally and was found to be a local buckling failure in the recovery/adapter assembly's aluminum cylinder at body station 43 with an applied moment of 21 000 in-lb.

Steady-state calculations indicate that transverse inertia loadings on the fins are high in that both translational and rotational effects are in the same sense but the resulting force due to the accelerated mass of the light-weight fin panels is small compared with the aerodynamic loads at resonance shown in figure 29. These results were then compared with the proof tests performed on the fins by the manufacturer. The manufacturer submits each attached fin to a static load of 300 pounds applied at the predicted center-of-pressure location.

It was concluded from the previous discussion and results that the Bio-Space launch configuration would have adequate structural strength to withstand the predicted flight environment.

CHAPTER 5

Biological Bench Tests

The design of the complete Bio-Space configuration was necessarily dictated by the animal's tolerances to the previously described mission profile. Although a literature search provided general characteristics and some environmental tolerances for the laboratory white rat, it was deemed necessary to perform bench tests with the specimen to determine animal tolerances to various parameters and to develop effective methods of integrating the animal with the payload systems.

BENCH TEST OBJECTIVES

The objectives of the bench test are discussed in the following paragraphs.

Anesthesia

Anesthesia tests were conducted to determine the most effective types and methods of immobilizing the test animal prior to physically restraining the specimen and placing the experiment sensors on its body. Several types, dosages, and methods of administration were employed to determine the specimen's reaction time, "down" time, and tolerance levels.

Physical Restraints

Physical-restraint tests were conducted to determine the most effective method of physically restraining the specimen. The restraint techniques were evaluated with regard to apparent animal comfort, reduction of body movement, interference with experiment sensors, and assurance that the animal's body center line remained approximately coincident with the vehicle longitudinal axis.

Experiment Sensors

Since the experiment requirements dictated the inflight monitoring of the specimen's electrocardiogram and body temperature, several types of

electrodes as well as placement areas and techniques were evaluated. One type of thermistor was considered, and various placement areas were evaluated.

Life-Support Systems

The life-support systems tests were made to determine the effectiveness of the oxygen systems and the anhydrous lithium hydroxide absorption agent. The function, effectiveness, and duration of the two were evaluated.

Environmental Changes

The environmental changes tests were conducted to determine the animal's reaction, tolerance, and adaptability to the anticipated changes and extremes in pressure, oxygen content, and vehicle spin.

BENCH TEST PROCEDURES AND RESULTS

The procedures and results of the bench tests are discussed in the following paragraphs.

Anesthesia

Both general and local anesthesia were used during the test, the local anesthesia being used to eliminate any pain during electrode implantment.

Inhalation anesthesia—ether, fluothane, and halothane—were used with apparently equal success. The anesthetized period was sufficiently long to permit encouchment but not long enough to place the experiment sensors on the specimen. The inducement and recovery appeared rapid and smooth in nearly all cases.

An intravenous short-acting barbiturate was tried on several specimens. This anesthesia kept the animal immobilized long enough to perform all pre-flight operations. The inducement period was smooth and short with an apparently rapid and smooth recovery. Two serious difficulties were encountered with this type however; one being that of injection and the other in determining and administering a small enough dose to prevent toxicity.

Physical Restraints

Two restraint techniques were employed during the tests: The first was simply a cylindrical plexiglass tube, and the second was a contoured couch. A 1¼ inch-diameter plexiglass tube was used during the initial tests, but owing to its obvious lack of restraints, was soon discarded. The animal was allowed far too much latitude of movement, thereby drastically distorting the electrocardiogram records. Also, in some instances, there was sufficient movement to enable the specimen to dislodge the sensors.

An animal was later anesthetized and placed in a molding compound to establish general body contours. A fiber-glass couch was fabricated from the mold configuration. A ⅝-inch-diameter hole was drilled in the aft end through which the animal's tail was pulled and then taped along his abdomen. Coupled with taping the animal's front and rear legs, this procedure provided ample restraint.

Experiment Sensors

Well, plate, and spike electrodes were tested on several specimens to determine the best type or types. The placement was anterior-posterior and lateral-lateral. The electrodes were glued to a shaved body area and also implanted beneath the skin and sutured in place.

The plate-type electrode furnished the best general functionality, giving good readings with both types of attachment. Both the well and spike types were fairly bulky and difficult to immobilize. Due to the sensitivity of the read-out to muscle noise, the latter two types were discarded.

The lateral-lateral electrode placement provided the most uniform records, the wave forms being of sufficient amplitude to be readable. The best read-out was obtained from the implanted electrodes which apparently caused the specimen little or no discomfort and no after-effects.

Life-Support Systems

Life-support systems tests were made to determine the effectiveness of the oxygen systems and the anhydrous lithium hydroxide absorption agent.

The life-support capsule was simply a sealed fiber-glass tube approximately 18 inches in length and 2-¾ inches in diameter, with the encouched

specimen mounted in the aft end. Both environmental design concepts described in the section entitled "Mechanical Configuration" were tested with several specimens. An altimeter was connected to the life-support capsule, and the pressure change with time was determined for both the internal oxygen supply and the pressurized capsule designs. Data obtained indicated that the specimen can survive over 8 hours in the life-support capsule at the design environments without pronounced adverse effects.

Two blankets containing 10 grams each of anhydrous lithium hydroxide were used primarily for carbon dioxide absorption. The blankets were taped to a plastic shield that was attached across the open front of the fiber-glass couch.

Environmental Changes

The animal was subjected to the predicted changes in pressure and roll rate. The condition in which a complete failure of the oxygen seal occurs was also reproduced. The test apparatus for the pressure tests included the flight tube connected to a vacuum pump and the altimeter gage hook-up. The change in vehicle roll rate was reproduced on a variable-drive lathe with a tachometer.

The animal showed no apparent discomfort or ill effects during any of the pressure tests, including that which reproduced the failure of the oxygen seal. The specimens tested demonstrated a remarkable ability to adjust to severe pressure changes.

The roll-rate tests consisted of placing the animal in the life-support capsule and mounting the capsule on a lathe, one end being chucked and the other placed on a free center. The lathe was then spun over a spin time history representing the vehicle's predicted roll-rate performance from launch to parachute deployment. At the conclusion, the animal exhibited some dizziness and eye protrusion. The dizziness disappeared after approximately 5 minutes, but the eye protrusion lasted 24 to 48 hours.

CHAPTER 6

Payload Flight-Qualification Testing

The satisfactory conclusion of a number of payload tests was considered essential prior to the approval of a final payload design. The original test program called for a concentration of efforts in two areas, drop-model tests from a helicopter and payload environmental tests. During the course of payload development, it became necessary to include two additional tests, a payload static-load test and a payload-separation-system ground test. A discussion of the qualification tests and the results of each are presented.

DROP MODEL TESTS

A free-falling payload model dropped from a helicopter often provides the simplest, most economical, and most comprehensive method of obtaining both qualitative and quantitative information on payload events performed in a simulated flight environment. This type of test is particularly useful in evaluating payload recovery systems and techniques.

The Bio-Space drop model consisted of a payload mock-up, a parachute assembly, and a specially designed afterbody containing a modified Arcas gas-generator separation device. The afterbody, or fin assembly, was designed to simulate the total Arcas launch-vehicle mass and to provide a static stability of 1 caliber to the drop model prior to payload separation. To minimize the possibility of collision between the afterbody and the parachute-stabilized payload after the separation event, the afterbody alone was designed to be statically unstable, and two of the four fins were canted at 3° to induce an instantaneous change in heading and a tumbling motion after payload separation. The drop model was released at an altitude of 10 000 feet, and payload separation was delayed for 5 seconds after release. The resulting aerodynamic pressure at separation approximated the predicted pressure expected at payload separation during rocket flight.

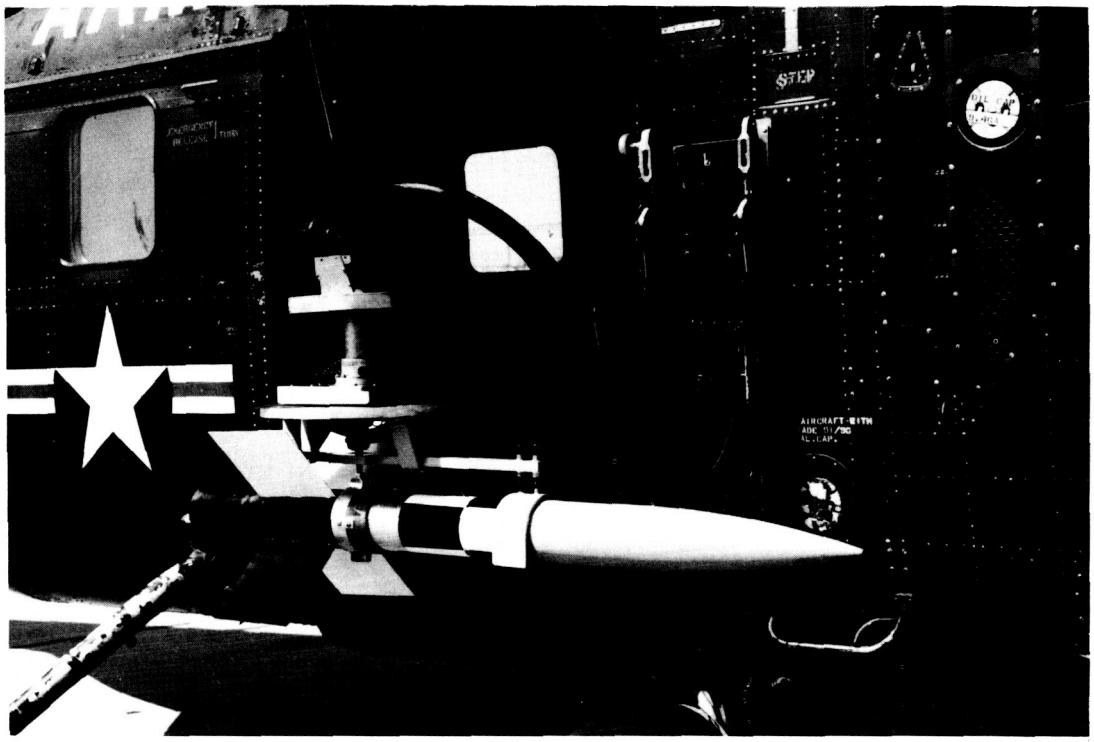

FIGURE 38. — *Drop model.*

Two separate drop-model tests were conducted. Each payload mock-up was designed to represent as closely as possible the total mass and mass distribution of the flight payload. Wherever possible, prototype payload structures were employed. Mechanical shock-indicating accelerometers were installed in both payloads along the three orthogonal axes to obtain quantitative data for the payload separation, parachute deployment, and water impact events. A telemetry transmitter, power supply, and antenna system were included in the second payload mock-up. A photograph of the drop model attached to the helicopter is shown in figure 38.

The objectives and results of the drop-model tests are presented in the following paragraphs.

Payload Structural Integrity

It was necessary to determine the capability of the prototype payload structure to withstand the shocks of payload separation, parachute deployment, and water impact. Although tracking camera coverage proved useful, evaluation of payload structural integrity was almost wholly dependent upon payload recovery. From the inspection of both successfully recovered payloads, it was concluded that the prototype payload structure would adequately withstand all predicted post-launch events.

Payload Separation System Performance

To improve upon the undesirable separation shock level and burning characteristics often obtained from the standard Arcas payload separation device, it was decided to employ a newly developed separation device utilizing a progressive-burning ballistic propellant charge. One objective of both drop-model tests was to evaluate the performance of the payload-separation system utilizing the new device. This test was particularly important because of major differences between the mass and nose cone configuration of a standard Arcas payload and that of the Bio-Space payload. A minor modification was made to each separation device so that it could be electrically actuated after helicopter release by a 5-second time delay programer installed in the drop-model afterbody. Test results were determined primarily from tracking camera coverage and inspection of the recovered payloads. It was concluded that the system utilizing the new separation device would provide sufficiently reliable separation between the Arcas launch vehicle and the Bio-Space payload consistent with all payload-component shock limitations.

Parachute Performance

Payload recovery criteria and predicted vehicle trajectory parameters necessitated a new parachute system design. Drop-model test objectives included evaluation of the parachute deployment technique, the structural integrity of the parachute, and the payload descent stability and impact dispersion as affected by the parachute.

Tracking-camera coverage and inspection of the recovered payloads indicated that the modified parachute deployment technique would work satisfactorily in flight.

It was later necessary to modify the deployment technique further to include an additional 6-second delay between payload separation and parachute deployment, when it was found during initial flight testing that the separated Arcas launch vehicle could collide with the deployed parachute. The additional 6 seconds provided time for the trajectories of the Arcas launch vehicle and the payload to diverge sufficiently before deployment of the payload parachute. A third drop test was conducted to evaluate the operation of the new technique with satisfactory results.

Tracking-camera coverage and inspection of the recovered payloads proved the capability of the parachute to structurally withstand deployment at an aerodynamic pressure approximating the predicted maximum that could be expected at parachute deployment during rocket flight.

From tracking camera coverage and radar data, it was determined that the payload descent rate and stability after parachute deployment were near the predicted values. The radar track, along with the known existing wind profile, also provided a check on the method that was used for predicting Bio-Space payload wind impacts.

Telemetry System Performance

To evaluate the adequacy of the telemetry transmitter RF signal strength and the capability of the telemetry system to withstand all post-launch shock events, the Bio-Space payload telemetry transmitter, antenna, and power supply were included in the second drop-model payload. The signal strength record obtained at the ground station and the inspection of the recovered payload provided satisfactory proof of adequate design.

Water Impact Loads

Inspection of the recovered payloads verified that the water impact event could be satisfactorily withstood.

Payload Recovery

One of the primary Bio-Space payload design criteria was the requirement for the water recovery of the payload containing a live small-animal specimen. An important objective of the drop-model tests was the evaluation of payload flotation characteristics and recovery aid effectiveness.

After impact, the drop-model payloads assumed a flotation attitude of approximately 15° from horizontal, thus exposing a relatively large nose-cone area as seen from above. Inspection of the recovered payloads verified that the nose-cone payload triple O-ring seal provided adequate protection against any leakage into the closed volume. The radar-reflective parachute, the brightly painted nose cone, and the dye marker all proved effective as recovery aids. The fluorescent orange nose-cone provided a high contrast to the background formed by the green fluorescein dye marker and was easily visible from the recovery vehicles (aircraft and surface vessels).

PAYLOAD STATIC LOAD TESTS

Vehicle break-up was evidenced on the initial two launches. Prior to the aerodynamically induced structural failure of the recovery/adapter section, the vehicle's dynamic motions were characterized by very large coning motions that exceeded predicted angles of attack and resulting flight loads. The dynamic motion signature from both flights indicated that the problem was either dynamic instability, aeroelasticity, or a combination of both. Due to the complexity of the problem and the unknowns involved, changes were made to the launch vehicle in both potential problem areas. The vehicle spin rate program was changed and the recovery/adapter joint was modified to provide greater stiffness.

Prior to the third flight test, a payload static load test was conducted to validate calculations on the structural integrity of the new separation joint under static load conditions. Static load tests at various payload stations were performed to determine payload deflections versus applied load.

PAYLOAD SEPARATION SYSTEM TEST

Because the launch-vehicle-payload separation joint had been modified extensively after the conclusion of the drop-model tests, it was necessary to requalify the separation system before the resumption of flight testing. A test model was assembled and consisted of a strapped down inert Arcas launch vehicle, the modified separation system containing a gas-generator separation device, a parachute assembly, and a mock-up Bio-Space payload. The separation device was electrically actuated from a remote site. From photographic coverage of the separation event and inspection of the separated items, it was concluded that the redesigned joint would neither degrade separation reliability nor significantly reduce the relative payload separation velocity.

PAYLOAD ENVIRONMENTAL TESTS

Using the information obtained during previous testing, a prototype small-animal payload was constructed to duplicate the intended final payload design. The prototype payload was subjected to a series of environmental tests to determine the existence of mechanical or electrical problems under conditions that could not be simulated during earlier tests. To establish a margin of integrity, the prototype was required to operate properly within test limits chosen which were more severe than those anticipated from flight.

The four flight payloads, two instrumented rounds and two small-animal rounds, were each tested to limits approximating as closely as possible expected flight conditions. Satisfactory performance of the four flight payloads during environmental tests concluded the testing program, and each payload was considered qualified for flight. Significant environmental test parameters are outlined in table I.

TABLE I
Bio-Space Payload Environmental Test Parameters

(a) Sinusoidal Vibration
[Frequency logarithmically swept at 2.0 octaves/min]

Model	Frequency range, cps	Acceleration amplitude
Prototype	20 to 40	0.08 in. D.A.
(All three axes)	40 to 2000	± 6.5 vector g
Flight	20 to 70	0.02 in. D.A.
(All three axes)	70 to 2000	± 5.0 vector g

(b) Randon Vibration
[Flight models only, all three axes]

Frequency range, cps	Test duration, sec	Acceleration density, g^2/cps	Acceleration, rms g
20 to 2000	65	0.0125	5.0

(c) Shock
[Longitudinal axis only]

Model	No. of tests	Average pulse duration per test, msec	Average shock per test, g
Prototype	2	18	62
Flight	1	15	66

(d) Altitude

Model	Maximum altitude simulated, ft	Time at maximum altitude, min
Prototype	200 000	20
Flight	150 000	10

CHAPTER 7

Flight Tests and Results

FLIGHT TESTING RÉSUMÉ

The flight test program for the development of the Bio-Space launch configuration consisted of six developmental firings. Comprehensive design verification of the small animal payload, launch vehicle, and recovery system was achieved with the test series. The extent of the flight testing for this development program was predicated primarily on the relatively inexpensive launch vehicle employed, and the sequence of the testing was influenced primarily by procurement lead time required for various payload instrumentation.

The initial two vehicles carrying inert payloads broke up near rocket burnout. Prior to the aerodynamically induced structural failure of the recovery/adapter section, the vehicle's dynamic motions were characterized by very large coning motions that exceeded predicted angles of attack and resulting flight loads. Dynamic instability, aeroelasticity, or a combination of both were indicated from the dynamic motion signature as the probable modes of failure. Changes were made to the launch configuration in both potential problem areas, and the remaining four launches exhibited adequate vehicle stability and performance. The third firing was successful in that the payload was recovered completely intact with a slightly damaged attached parachute. The fourth launch in the test series experienced a catastrophic parachute failure which initiated a deployment system modification that was incorporated and successfully tested on the last two launchings in the test program. The fifth and sixth launches of the test series, carrying the only live specimens flight tested, were successfully launched and recovered. A lift-off sequence for the fifth test firing carrying the first live specimen is shown in figure 39. The recovered specimen is shown in figure 40 with the life support capsule removed immediately following recovery of the bio-payload.

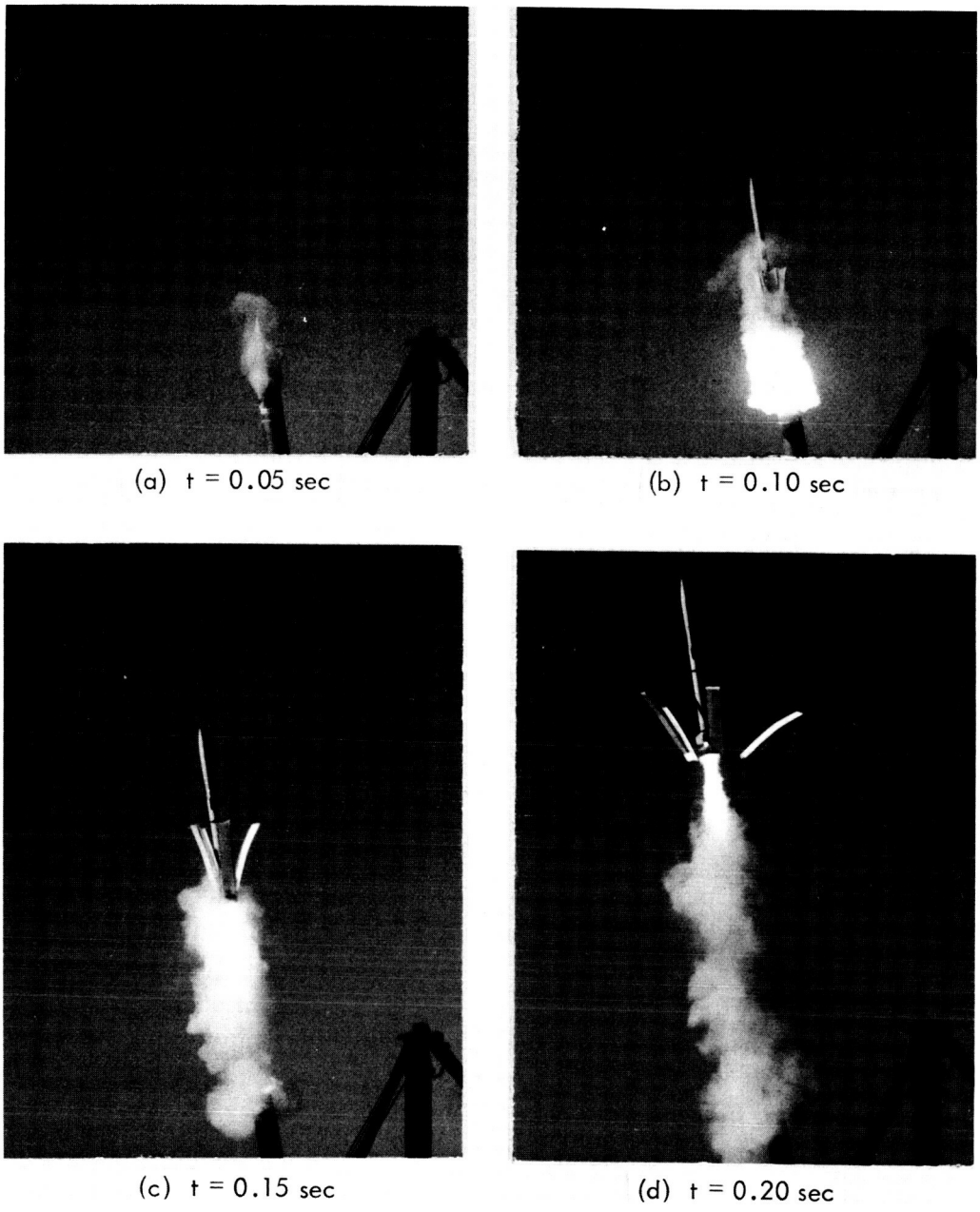

(a) t = 0.05 sec

(b) t = 0.10 sec

(c) t = 0.15 sec

(d) t = 0.20 sec

FIGURE 39. — *Lift-off sequence for test flight 5 (model T1-1677).*

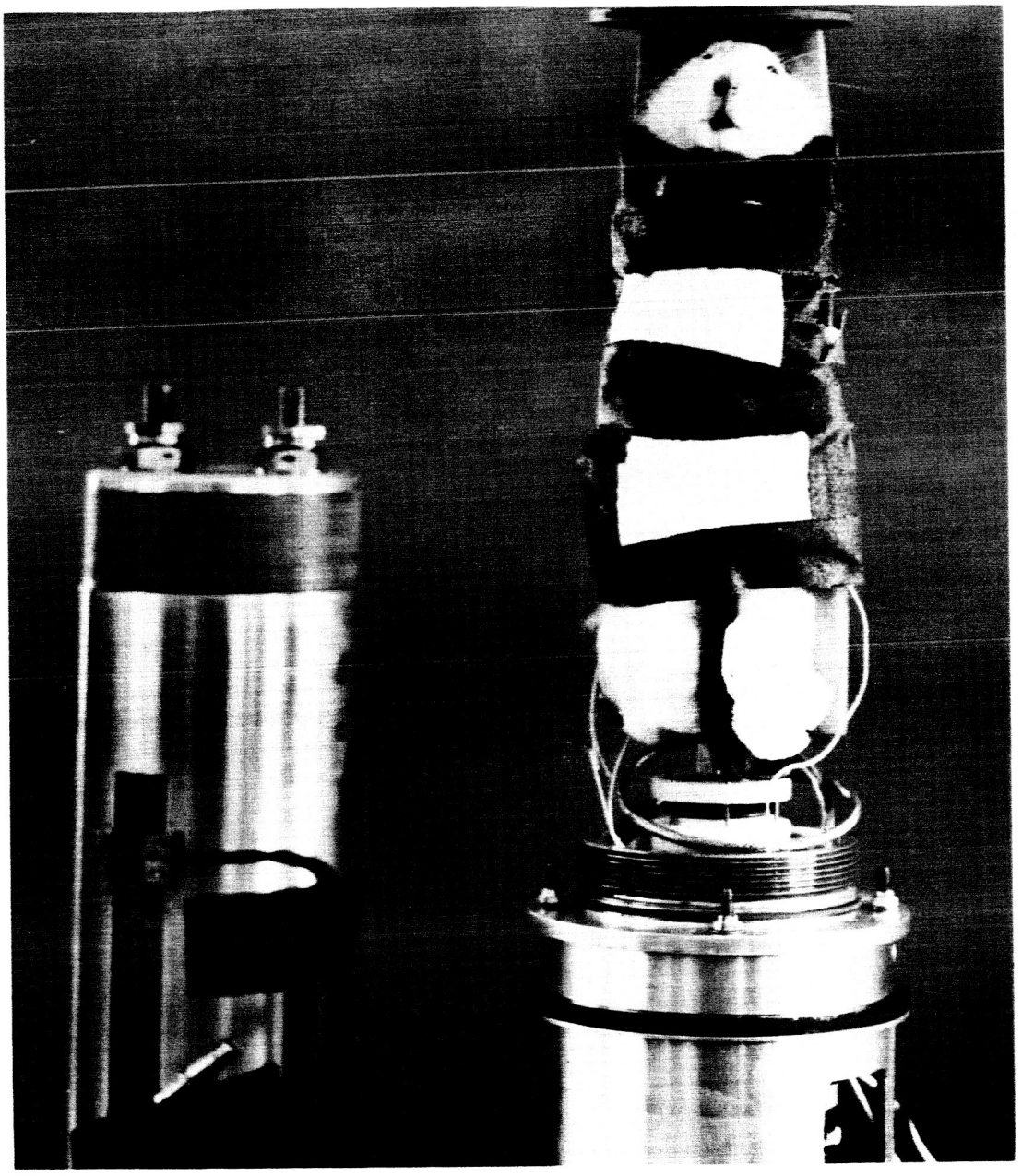

FIGURE 40. — *Recovered specimen and payload.*

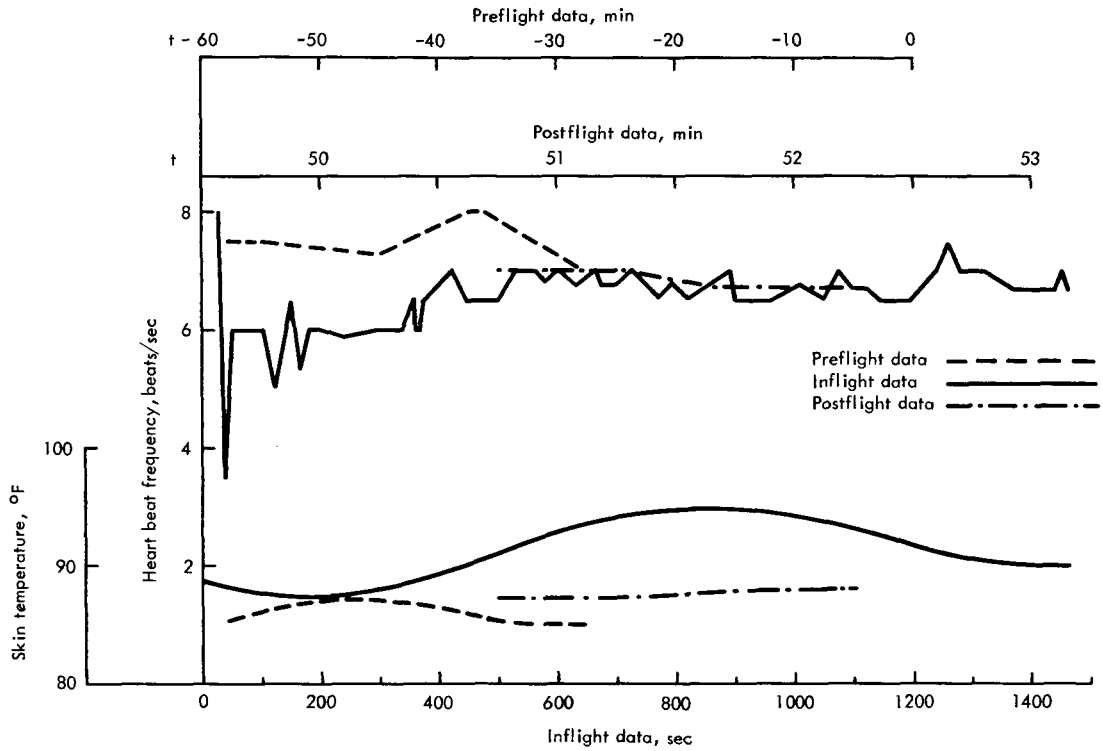

FIGURE 41. — *Biological parameters.*

TEST DATA DISCUSSION

Flight test data were primarily obtained from telemetry, radar, and tracking cameras. Telemetry data provided roll rate, longitudinal acceleration, life-support-capsule pressure, and the specimen's ECG and skin temperature. The biological parameters, ECG and skin temperature, obtained from the live specimen during the sixth flight test are shown in figure 41 including preflight and postflight data for comparative purposes. Radar data provided the trajectory parameters shown in figures 42, 43, and 44. Film data were used extensively to determine the vehicle's dynamic motions during the early portion of the trajectory. Heat-sensitive paints were applied to the

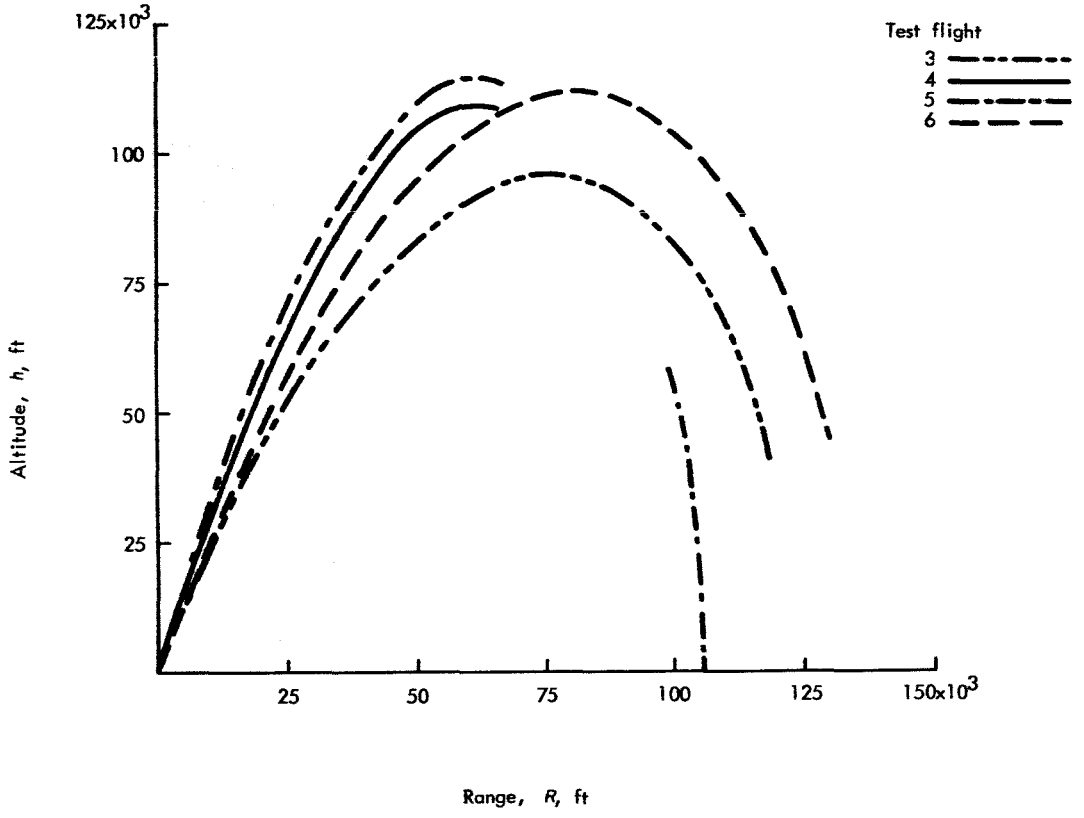

FIGURE 42. — *Flight-test trajectory profiles for launch vehicle.*

inside of the payload nose cone to determine maximum temperature encountered during flight.

Test Flights 1 and 2

Test flights 1 and 2 (models T1-1673 and T1-1674) were conducted on June 25 and July 10, 1964. Inert payloads were used in both flights, and the launch configurations were the same, with two exceptions. The roll-rate program had a maximum of 4 cps for the first test and a maximum of 8 cps for the second. Also, the adapter/recovery assembly was structurally reinforced

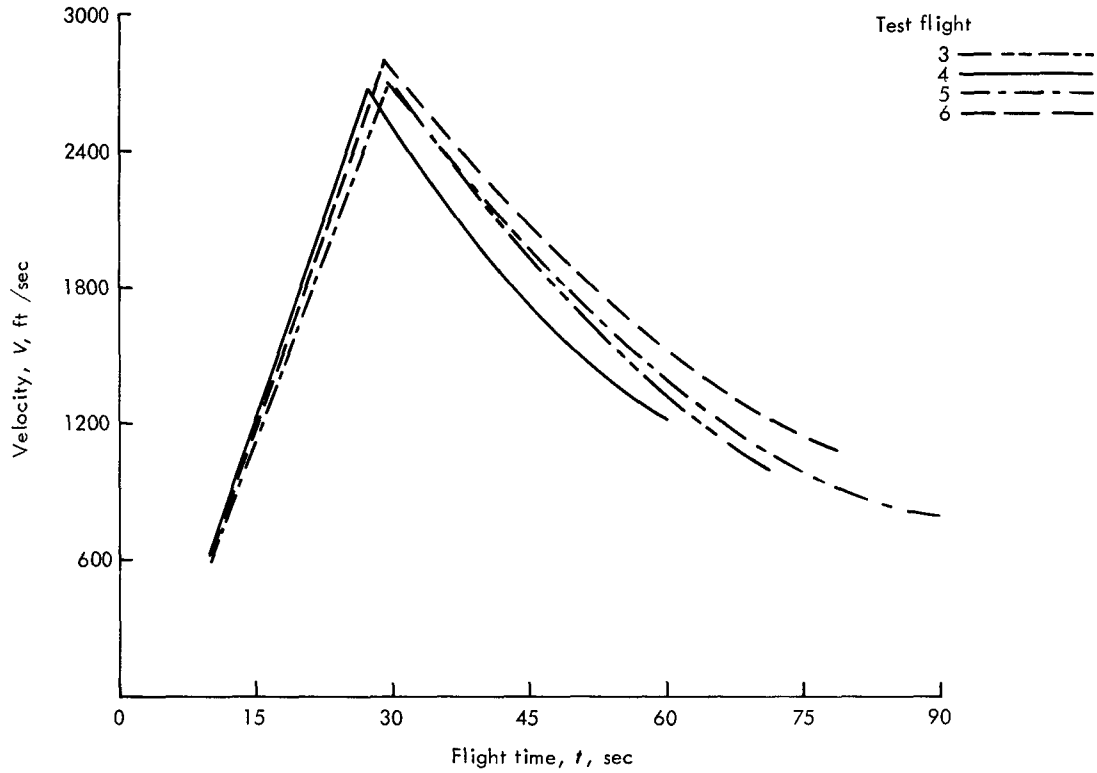

FIGURE 43. — *Flight-test velocity data.*

for the second test. Tracking cameras provided limited vehicle motion data from lift-off until approximately $t = 15$ seconds for both flights. Tracking data for the first flight revealed that the roll rate became erratic with accompanying large coning angles in the transonic region from approximately $t = 8$ seconds to $t = 10$ seconds. Immediately afterwards, an abrupt dynamic motion convergence and resulting steady flight persisted until approximately $t = 17$ seconds when the coning motions began again and increased progressively until $t = 24.5$ seconds when the vehicle broke up as a result of the large coning angles and prevailing dynamic pressure. The trajectory profile and dynamic motion signature of the second flight was essentially the same as that of the first, with the vehicle breaking up at $t = 27.9$ seconds. A quantitative failure analysis of the two flights was not possible because of lack of

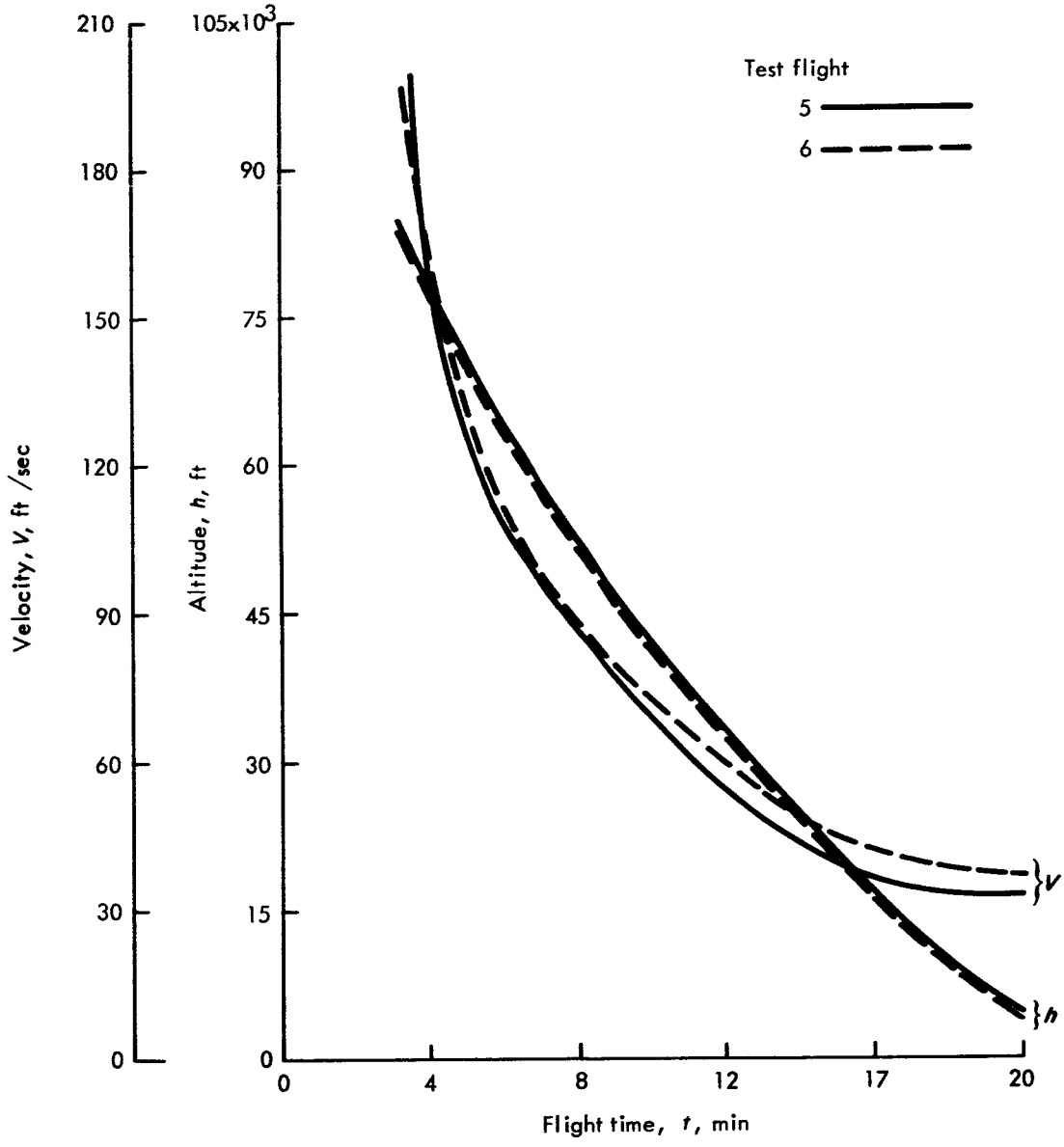

FIGURE 44 — *Recovery-system descent test data.*

data (roll rates, motion amplitudes, frequencies, and phase angles) during the portion of the flight before and during vehicle breakup. Postulated dynamic instability near breakup would include a nutational and rolling-velocity resonance and/or a Magnus instability.

It is believed that the erratic roll rates and coning motions during the transonic region are a combination of the "undamping" dynamic pitching moment and resulting induced rolling moments and resonance of the nutation frequency with the rocket's rolling velocity.

Another possible cause of the observed flight behavior is aeroelasticity. Basic physical and trajectory input data were provided to Langley Research Center to perform an aeroelastic analysis for the subject configurations. From this analysis, it was concluded that the initial design of the subject vehicles did not appear conservative in view of margin against aeroelastic divergence. Stability was also found to be highly sensitive to small changes in fin lift characteristics and joint stiffness.

It was also concluded that the observed flight behavior could have resulted from a combination of both of the previously described failure mechanisms, that is, dynamic instability and aeroelasticity.

Test Flight 3

Test flight 3 (model T1-1675) was conducted on July 23, 1964, and as a result of design changes, was successful aerodynamically. The roll rate program was changed from a maximum of 4 cps to a maximum of 20 cps for two reasons: (1) The 20-cps maximum roll rate program would not allow the vehicle to approach the resonance region during a flight time when low damping and high aerodynamic pressures were existent as the 4-cps maximum program did; and (2) since it was expected that induced roll moments were causing the erratic roll rates observed in test flights 1 and 2, the higher roll driving moments involved with the 20-cps maximum roll program would help overcome possible negative induced roll moments tending to cause the roll acceleration to become smaller than predicted, or even negative.

Also, the connecting joint between the nose cone and the recovery/adapter assembly was modified. The engagement portion between the nose cone and the recovery/adapter assembly was lengthened to provide a stronger connect-

ing joint engagement. This flight included the first test of the complete Bio-Space payload (without live specimen).

The payload included a telemetry system providing continuous roll-rate data. Temperature-sensitive paints were used to indicate maximum temperatures experienced on the inner surface of the nose cone at approximately 12 inches from the nose tip. These paints indicated a maximum temperature of approximately 250°F.

The recovery system experienced a partial failure involving parachute damage believed to have been caused from interference with the expended launch vehicle.

Test Flight 4

Test flight 4 (model T1-1676 was conducted on July 29, 1964. This model was identical in every respect to test vehicle 3. Vehicle aerodynamic performance was satisfactory; however, a catastrophic parachute failure resulted in the nose cone free-falling from 72 800 feet. The payload without attached parachute was recovered heavily damaged and partially filled with seawater.

Test Flights 5 and 6

Test flights 5 and 6 (models T1-1677 and T1-1746) were conducted on September 3 and 26, 1964, respectively. Test vehicles 5 and 6 were aerodynamically identical to test vehicles 3 and 4.

The recovery system employed a parachute reefing device designed to delay parachute opening until 6 seconds after payload separation. This delay allowed the faster falling launch vehicle to attain a larger separation distance from the recovery package after parachute opening.

Test vehicles 5 and 6 also contained live animal payloads in order to test the Bio-Space vehicle system's capability to accommodate a live specimen and return biological data to receiving stations. Both test flights 5 and 6 were completely successful in launch vehicle aerodynamic performance and recovery system operation. Also, live-specimen heart beat and skin temperature were monitored and recorded continuously during flight.

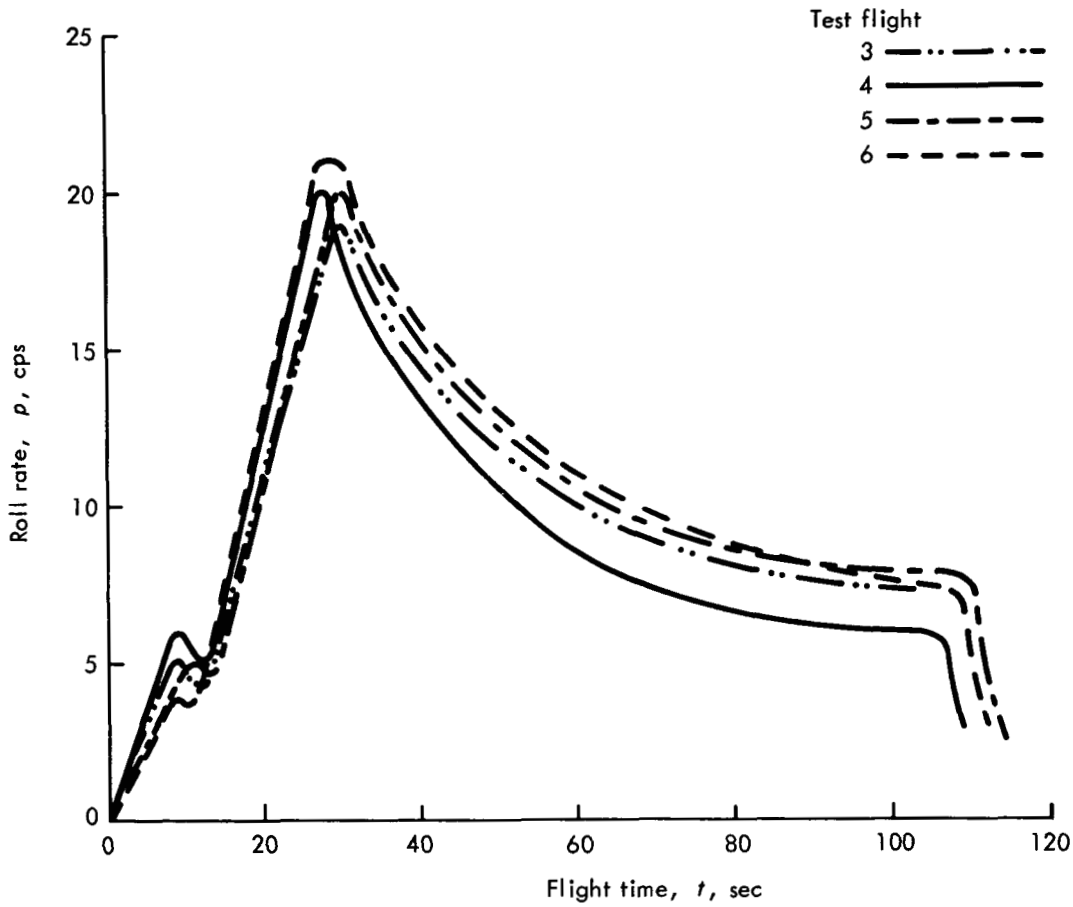

FIGURE 45. — *Flight-test roll-rate data.*

Figures 42 and 45 present the aerodynamic performance of test flights 3, 4, 5, and 6, all of which were successful in this respect. Figure 44 shows the recovery system performance of test flights 5 and 6.

Altitude-range trajectory profiles are shown in figure 42. These data are for the launch vehicle only and do not indicate recovery system performance. Figure 43 presents total vehicle velocity as a function of flight time. It can be seen that a slightly early burnout time was experienced on test flight 4.

The roll rate as measured from telemetry data is shown in figure 45. A

variation in roll rate is indicated for all flights shown in the figure as the vehicle passes through the transonic region. This phenomenon was accompanied by substantial vehicle coning motions. These variations in vehicle motions, both in pitch and roll, can be explained by the unsteady flow field about the vehicle during the transonic flight region. This unsteady flow field may cause the pitch and roll damping coefficients to become positive, or self-exciting (ref. 21). This action is further triggered at this time due to the inherent low value of the pitch damping coefficient during transonic flight (see fig. 20). Initiation of the pitching motion would induce the roll motion variations, with the overall dynamic motion converging only after adequate pitch damping is resumed. This is confirmed by the rapid degeneration of coning motion observed after the vehicle passed through the transonic region.

Appendix

SYMBOLS

A	fin aspect ratio, $\frac{b^2}{S_f}$
a_x, a_y	accelerations parallel to missile X and Y axes, ft/sec^2
b	fin span, inches
C_D	drag-force coefficient
C_ℓ	rolling-moment coefficient
C_{ℓ_p}	rate of change of rolling-moment coefficient with rolling velocity, $\frac{\partial C_\ell}{\partial\left(\frac{pd}{2V}\right)}$, per radian
C_{ℓ_δ}	rate of change of rolling-moment coefficient with fin deflection $\frac{\partial C_\ell}{\partial \delta}$, per radian
C_m	pitching-moment coefficient.
C_{m_α}	rate of change of pitching-moment coefficient with angle of attack, $\frac{\partial C_m}{\partial \alpha}$, per radian
C_{m_q}	rate of change of pitching-moment coefficient with pitching velocity, $\frac{\partial C_m}{\partial\left(\frac{qd}{2V}\right)}$, per radian
$C_{m_{\dot\alpha}}$	rate of change of pitching-moment coefficient with rate of change of angle of attack, $\frac{\partial C_m}{\partial\left(\frac{\dot\alpha d}{2V}\right)}$, per radian
C_N	normal-force coefficient
C_{N_α}	rate of change of normal-force coefficient with angle of attack, $\frac{\partial C_N}{\partial \alpha}$, per radian

c	chord length, inches
$\bar{c}$	mean aerodynamic chord, inches
D_m	mass unbalance, lb-in.^{2}
d	body diameter, inches
E	modulus of elasticity
F	thrust, pounds
F_N	normal force, pounds
F_{N_α}	rate of change of normal force with angle of attack, lb/rad
F_X	axial force, pounds
f_m	magnification factor
g	acceleration due to gravity, ft/sec^2
h	altitude, feet
I	mass moment of inertia, slug-ft^2
I_x, I_y	mass moment of inertia about X and Y axes, respectively, slug-ft^2
$(K_b)_f$	interference factor—fin effect on the body
$(K_f)_b$	interference factor—body effect on the fin
M	Mach number
M_X	roll moment, ft-lb
M_{X_p}	roll damping moment, ft-lb
M_{X_δ}	roll driving moment, ft-lb
$(M_X)_{\phi,\eta}$	induced roll moment, ft-lb
M_Y	pitching moment, ft-lb
$M_{Y,A}$	pitching moment due to vehicle asymmetries, ft-lb
M_{Y_α}	rate of change of pitching moment with angle of attack, ft-lb/rad
M_{Y_q}	rate of change of pitching moment with pitching velocity, ft-lb-sec/rad
$(M_{Y_q})_j$	rate of change of pitching moment with pitching velocity due to jet damping, ft-lb-sec/rad

m	vehicle mass, slugs
p	rolling velocity, rad/sec
q	pitching velocity, rad/sec; or dynamic pressure, lb/ft^2
R	range, ft
S	surface area, ft^2
S_R	reference area, ft^2
s_w	wind shear, per second
T	temperature, °F
t	flight time, seconds; or fin thickness, inches
V	total missile velocity relative to wind, ft/sec
W	vehicle weight, pounds
w	wind velocity, ft/sec
X	position of instantaneous flow reaction from nose, inches
X, Y, Z	body axes of launch vehicle
x	station along longitudinal axis, inches from nose
x_{cg}	center-of-gravity distance from nose, inches
x_{cp}	center-of-pressure distance from nose, inches
y	distance along fin span, inches
$\bar{y}$	effective fin moment arm, inches
α	angle of attack, radians
$\Delta\alpha$	induced angle of attack, radians
α_T	total angle of attack, degrees
α_w	wind angle of attack, degrees
β	angle of slideslip, radians
γ	flight path angle, degrees
δ	fin deflection, degrees
$(\delta_a)_f$	fin aerodynamic misalinement, degrees
$(\delta_a)_n$	nose aerodynamic misalinement, degrees

δ_F	thrust misalinement, degrees
η	resultant or total flow incidence angle $(\alpha^2 + \beta^2)^{1/2}$, degrees
Θ_b	boattail angle, degrees
Θ_{te}	total airfoil trailing edge angle, degrees
Λ_{te}	fin leading edge angle, degrees
λ	fin taper ratio, $\frac{c_t}{c_r}$
ξ	damping function
ρ	atmospheric density, slugs/ft^3
σ	standard deviation
ω_n	aerodynamic natural frequency, rad/sec
ω_s	structural frequency, rad/sec

SUBSCRIPTS

bt	boattail
e	exposed
f	fin
max	maximum
n	number of vehicle components
n/b	nose/body
o	initial conditions
r	root
t	tip

References

1. WEBSTER, R.C.; ROBERTS, W.C., JR.; and DONNELL, E.P.: Final Report — Development of the Arcas Rocketsonde System. Contract NOnr-2477(00), Atlantic Res. Corp., 1960.
2. WEAVER, W.L.; SWANSON, A.G.; and SPURLING, J.F.: Statistical Wind Distribution Data for use at NASA Wallops Station. NASA TN D–1249, 1962.
3. HOAK, D.E.; and CARLSON, J.W.: USAF Stability and Control DATCOM. Air Force Flight Dynamics Laboratory, Wright-Patterson Air Force Base, 1963.
4. STONEY, W.E., JR.: Collection of Zero-Lift Drag Data on Bodies of Revolution From Free-Flight Investigations. NASA TR R–100, 1961.
5. MAXWELL, N.E.; and SHUTTS, W.H.: Aerodynamic Effects of Boattailing on a Body of Revolution. Rept. CM–645, Consolidated Vultee Aircraft Corp., 1961.
6. HOERNER, SIGHARD F.: Fluid Dynamic Drag. Publ. by author (Midland Park, N.J.), 1958.
7. ADAMSON, DAVID: Bodies of Revolution. Sect. 8 of Handbook of Supersonic Aerodynamics, U.S. Bur. Ord. (Bur. Naval Weapons).
8. SYVERSON, C.A.; and DENNIS, D.H.: A Second-Order Shock-Expansion Method Applicable to Bodies of Revolution Near Zero Lift. NACA Report 1328, 1957.
9. DEJONGE, C.: The Effect of Low Aspect Ratio Rectangular and Delta Cruciform Fins on the Stability of Bodies of Revolution With Tangent Ogives at Small Angles of Attack Through a Mach Number Range of 0 to 3.5. Rept. No. RF–TR–62–1, 1962.
10. MCNERNEY, J.D.: Aerobee 350 Wind Tunnel Test Analysis. Rept. No. 265FR–8, Space General Corp., 1963.
11. PITTS, W.C.; NIELSEN, J.N.; and KAATTARI, G.E.: Lift and Center of Pressure of Wing-Body-Tail Combinations at Subsonic, Transonic, and Supersonic Speeds. NACA Rept. 1307, 1957.
12. TRILLING, L.; and QUIGLEY, R.E.: Approximate Methods for Estimating Transonic Pressure Distributions and Aerodynamic Coefficients. MIT Aeronautical Engineering Dept.
13. HUTH, J.H.; and DYE, H.M.: Axial and Normal Force Coefficients for Pointed Bodies of Revolution at Supersonic and Hypersonic Speeds, Part II — Boattails. Rept. RM–905, The RAND Corp., 1952.
14. GRIMMINGER, G.; WILLIAMS, E.P.; and YOUNG, G.B.W.: Lift on Inclined Bodies of Revolution in Hypersonic Flow. J. Aeron. Sci. vol. 17, No. 11, Nov. 1950, pp. 675–690.
15. NICOLAIDES, J.D.: Missile Flight and Astrodynamics. Tech. note 100A, Dept. of Navy, Bur. Weapons, 1961.

16. JAMES, R.L., JR. (with appendix B by N.L. CRABILL): A Three-Dimensional Trajectory Simulation Using Six Degrees of Freedom With Arbitrary Wind. NASA TN D–641, 1961.

17. WHITLOCK, C.H.: Comparison of Steady-State and Six-Degree-of-Freedom Analysis of Pitch-Roll Resonance Conditions for a Long-Slender Sounding Rocket. NASA TN D–1816, 1963.

18. NELSON, R.L.: The Motions of Rolling Symmetrical Missiles Referred to a Body-Axis System. NACA TN 3737, 1956.

19. PARSONS, W.D.: Aerobee 350 — Aerodynamic Analysis. Rept. 265FR–3, Space General Corp., 1963.

20. HOOVER, W.L.; and REARDON, P.J.: Approximate Impact Drag Coefficient for the Vertical Water Entry for Families of Cone, Ellipsoidial, and Tangent Ogive Nose Missiles. NOL TR 64–110, Naval Ordnance Laboratory, Nov. 1965.

21. NICOLAIDES, JOHN D.: On Missile Flight Dynamics. Ph.D. Thesis, Catholic Univ. of America, 1963.

☆U. S. GOVERNMENT PRINTING OFFICE: 1966 — O 214-693